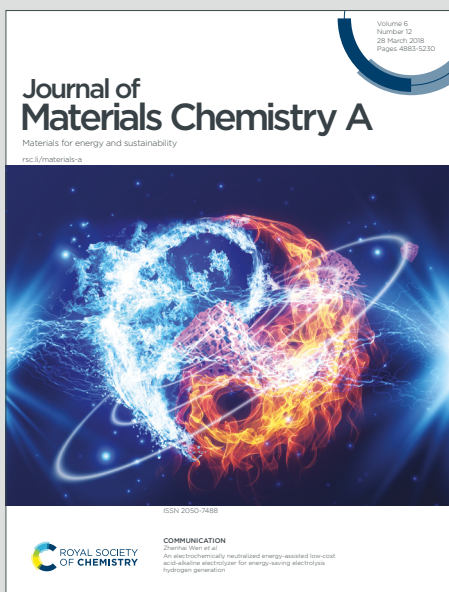


Journal of Materials Chemistry A

Materials for energy and sustainability

Accepted Manuscript

This article can be cited before page numbers have been issued, to do this please use: M. Mazraeh, Z. Hedayati, A. Primo, A. Dhakshinamoorthy, M. Ali and H. Garcia, *J. Mater. Chem. A*, 2026, DOI: 10.1039/D5TA06669G.



This is an Accepted Manuscript, which has been through the Royal Society of Chemistry peer review process and has been accepted for publication.

Accepted Manuscripts are published online shortly after acceptance, before technical editing, formatting and proof reading. Using this free service, authors can make their results available to the community, in citable form, before we publish the edited article. We will replace this Accepted Manuscript with the edited and formatted Advance Article as soon as it is available.

You can find more information about Accepted Manuscripts in the [Information for Authors](#).

Please note that technical editing may introduce minor changes to the text and/or graphics, which may alter content. The journal's standard [Terms & Conditions](#) and the [Ethical guidelines](#) still apply. In no event shall the Royal Society of Chemistry be held responsible for any errors or omissions in this Accepted Manuscript or any consequences arising from the use of any information it contains.

Recent Advances of Multi-Metallic Organic Frameworks and their Derivatives for Catalysis, Electro-/Photocatalysis and Sensing Applications

Mohammad Mazraeh,¹ Zeynab Hedayati,¹ Ana Primo,² Amarajothi Dhakshinamoorthy,^{*3,4} Ali Morsali,^{*1} and Hermenegildo Garcia^{*2}

¹Department of Chemistry, Faculty of Sciences, Tarbiat Modares University, P.O. Box 14115-175, Tehran, Iran.

²Instituto Universitario de Tecnología Química, Consejo Superior de Investigaciones Científicas-Universitat Politecnica de Valencia, Universitat Politecnica de Valencia, Av. De los Naranjos s/n, 46022, Valencia, Spain.

³Departamento de Química, Universitat Politècnica de València, C/Camino de Vera, s/n, 46022, Valencia, Spain.

⁴School of Chemistry, Madurai Kamaraj University, Madurai, Tamil Nadu, 625 021, India.

Abstract

The growing global demand for advanced porous materials for a wide gamut of applications has spurred significant interest in metal-organic frameworks (MOFs). These structures are highly valued for their engineering versatility, combined with multifunctionality, vast chemical space, and structural diversity. Various strategies have been developed to enhance the performance of MOFs in different applications, with one of the most promising approaches being the incorporation of multiple metals into their structure to form multi-metallic organic frameworks (MMOFs). MMOFs exhibit outstanding performance compared to the MOFs due to the tunable synergistic effect among diverse metals, which can be gained by their unique engineering. The simultaneous presence of several metals imparts exceptionally enhanced properties to MMOFs, including active site tunability, which optimizes their catalytic, photocatalytic, and electrocatalytic performance. Additionally, MMOFs exhibit superior sensing capabilities, characterized by higher sensitivity and precision, and demonstrate improved medicinal properties. This review provides a comprehensive, critical view of MMOFs, focusing on their synthesis strategies, challenges, and the specific or preferential role of each metal when



they are present in MMOFs. Further, this review also covers their applications in various fields, such as catalysis, photocatalysis, electrocatalysis, electrical energy storage, gas separation, adsorption, sensing, and medicine. Furthermore, the review offers guidelines in the selection of metals for tailoring MMOFs to specific applications. The numerous existing examples showing the superior performance of MMOFs compared to single-metal MOFs (SMOFs), underscoring the synergistic effects appearing from the combination of multiple metals present in the structure. This favorable synergy makes MMOFs the most efficient material in a wide range of technological and industrial applications.

Table of Contents

1. Introduction

2. Synthetic routes for MMOFs

2.1. Synthesis from Special Precursors

2.1.1. In Situ Synthesis

2.1.2. Cluster Synthesis Route

2.1.3. In Situ Growth on Nickel Foam

2.2. Metallo-Ligand Approach

2.3. MMOF-Derived Materials

2.3.1. 2D Structures in MMOF-Derived Materials

2.4. Post-Synthesis Strategies

2.4.1. Core-Shell Route

2.4.2. Insertion Methods

2.4.3. Exchange Methods

3. Applications

4. Iron-based MMOFs

5. Nickel-based MMOFs

6. Cobalt-based MMOFs

7. Zirconium-based MMOFs

8. Zinc-based MMOFs

9. Lanthanide-based MMOFs



10. Conclusion

11. Outlook and Future Prospects

Acknowledgements

References

1. Introduction

Approximately 25 years ago, porous metal-organic frameworks (MOFs) were reported by Kitagawa¹, Yaghi², and Férey³, and they quickly captured the attention of the scientific community. MOFs are composed of organic linkers and metal nodes, featuring unique characteristics such as high surface area, significant porosity, and tunable design with predictable structures based on the consideration of the linker structure and the directionality of the metal-ligand coordinative bond.^{2,4} These properties can be customized by selecting specific metal ions, organic linkers, and secondary building units (SBUs) with various compositions and directionality of the coordination bonds.⁴ MOFs have found applications across numerous fields, including medicine⁵, sensing⁶, catalysis⁷, renewable energy sector⁸, gas adsorption and separation.⁹

The porous structures of MOFs have attracted considerable attention due to their customizable pore design, adjustable chemical properties, and high surface area^{10, 11}, providing a toolbox to adapt the materials for their practical applications. Despite their widespread use, there is always a continued interest in further improving MOF performance, the discovery of new variants, and advances in their industrial scalability, promising a transformative impact on science and technology.¹²

A subclass of MOFs, known as multi-metallic organic frameworks (MMOFs), incorporates more than one metal ion in their structure.¹³ These metals may be integrated into the MOF structure as metal-organic compounds, metal complexes within cavities, or as part of the MOF nodes. bimetallic or heterometallic MOFs are included in this category.¹⁴ The incorporation of multiple metals can frequently create synergistic cooperation among them, enhancing the performance of MMOFs compared to single-metal MOFs (SMOFs) in applications such as electrocatalysis¹⁵, photocatalysis^{16, 17}, gas separation¹⁸, energy storage^{19, 20}, and sensing.²¹

In 2019, our group published the well-received paper "Mixed-Metal MOFs: Unique Opportunities in Functionalization and Design of Metal-Organic Frameworks"¹³, which highlighted the growing significance of MMOFs and their applications. Since then, the field has



seen rapid development, as evidenced by the exponential number of publications on MMOFs, particularly notable since 2016 (Figure 1a). This growing interest underscores the need for an updated review of recent advances in MMOFs to show the current state of the art, the present bottlenecks, and the challenges ahead.

Numerous reviews and perspectives have emphasized the critical role of the preparation of MMOFs and their derivatives, focusing on their use in specific applications. For example, some perspectives have focused on the challenges and opportunities associated with the metal node engineering in electrical energy storage systems.²² Others have provided the detailed description of the topological properties of MMOFs with the presence in a single material of different metallic nodes, synthetic methodologies, metal distributions within MMOFs, and their characterization.²³ Reviews covering synthesis routes, characterization techniques, and computational studies of MMOFs and their derivatives provide a conceptual framework to understand the reasons for the improved performance of MMOFs in applications such as catalysis, photocatalysis, and electrocatalysis.^{13, 24-26} Additionally, some reviews compare the development and performance of bimetallic MOFs and trimetallic MOFs and their derivatives with SMOFs counterparts.^{27, 28} Some reviews have focused on the specific applications of MMOFs and their derivatives, such as energy storage (e.g., supercapacitors and batteries),²⁹⁻³¹ water splitting (including oxygen evolution reaction (OER) and hydrogen evolution reaction (HER)),³²⁻³⁷ and photocatalysis.^{38, 39} Compared to other multi-metal compounds, MMOFs offer advantages particularly the possibility to design the structure and versatile synthetic methods, thus justifying their vast usage for diverse applications. Other important features of MMOFs are porosity and vast chemical space in ligands and metals, while metal oxides or alloys can lack this intrinsic chemical diversity. Also, the stability of MMOFs can differ on various applications compared to other multi-metal compounds. Furthermore, MMOFs can be the precursors of a wide range of multi-metal oxides/alloys/carbides and other variants.⁴⁰⁻⁴² By pyrolysis MMOFs can be converted into MMOF-derived materials preserving some advantages of the pristine MMOFs, such as hierarchical porosity, uniform distribution of metals, and tunable electronic structures, rendering highly active electrocatalysts and single-atom sites, which cannot be easily obtained from direct oxide synthesis.⁴³⁻⁴⁵ These accounts comprehensively address synthesis strategies, characterization methods, and applications, underscoring the potential offered by MMOFs in fundamental and technological advancements that focus on the role of metals and their synergistic effect in diverse applications,



which is not comprehensively stated in any other reviews. Besides, our review also compares the activity of MMOFs with that of SMOFs in different catalytic applications to precisely illustrate the importance of MMOFs. Eventually, some advantages can be achieved by MMOFs, which are different compared to other multi-metal compounds and justify their vast usage for diverse applications. One of these features can be attributed to the porosity and vast engineering of ligands and metals, while other metal oxides or alloys can lack this intrinsic molecular engineering. Also, the stability terms on MMOFs can vary on various engineering assignments compared to other multi-metal compounds. Furthermore, achieving multi-metal oxides/alloys/carbides and other variants by pyrolyzing MMOF to obtain MMOF-derived materials not only can preserve some advantages of the MMOFs, such as hierarchical porosity, dispersing metals, stability, and tunable electronic structures, but also can yield highly active electrocatalysts and single-atom sites, which cannot easily be obtained from direct oxide synthesis.

In this review, we focus on recent progress in MMOFs and their derivatives, which have garnered significant interest in recent years. The review is divided into two sections, the first part dealing with the synthesis of MMOFs and the second part summarizing their applications. The synthesis methods discussed here include diverse approaches to MMOF formation, either *de novo* or post-synthetic modification, analyzing their specific advantages and disadvantages, and how they impact the structural and functional performance of MMOFs. In the applications section, we emphasize the critical role of incorporating multiple metals, as the combination in the material of a second, third, or additional metals can significantly enhance some properties of the resulting MMOF with an impact on its performance. This review covers applications in adsorption, catalysis, electrocatalysis, energy storage, photocatalysis, sensing by electrochemical or fluorescence techniques, and related areas reported from 2019 to 2024, providing insights into the influence of multi-metal incorporation on MMOFs in these fields. It also analyzes the interactions among metals, the unique properties present in MMOFs, the structural modifications induced by the incorporation of additional metals in the composition, and the formation of MMOFs.

Figure 1b illustrates the proportion of the various metallic elements that have been reported in the composition of MMOFs and their derivatives. The applications are categorized into seven primary sections, highlighting each metal role and its interaction with neighboring metals. The intrinsic electroactive properties of Ni make it highly active in electrical energy applications, particularly in electrocatalysis and energy storage, where it significantly enhances specific



capacity. Further, Ni-MMOFs are also the most widely used materials in photocatalysis due to their ability to regulate band gaps, thereby improving the photocatalytic activity.⁴⁶

After Ni, Co, and Fe are the following most frequently reported metals in MMOFs. Their electroactive properties make them highly effective in energy-related applications. Fe-MMOFs, in addition to energy applications, are employed in the adsorption and removal of pollutants since the corresponding Fe-MMOFs have abundant active sites. Co-MMOFs, besides their role in energy applications, excel in catalysis, where these MMOFs exhibit high porosity, and their crystalline structure enhances catalytic efficiency. Lanthanide-based MMOFs demonstrate great potential, particularly in sensing applications, due to the sensitivity of atomic emissions in rare earth ions. The incorporation of additional lanthanide metals further enhances their efficiency through the appearance of synergistic effects. Zn-based MMOFs are also promising for diverse applications. In this case, Zn combined with Co is the most common pairing, as Co enhances crystallinity, while Fe, when paired with Zn, may reduce structural stability. Cu is another widely used metal in MMOFs, contributing to various applications. For the sake of organization, this review, MMOFs based on the metal present in the highest proportion in the material. For some metals, like Cu, that have not yet been reported to be in the highest proportion, their examples of MMOFs are scattered in sections corresponding to the most abundant metal.

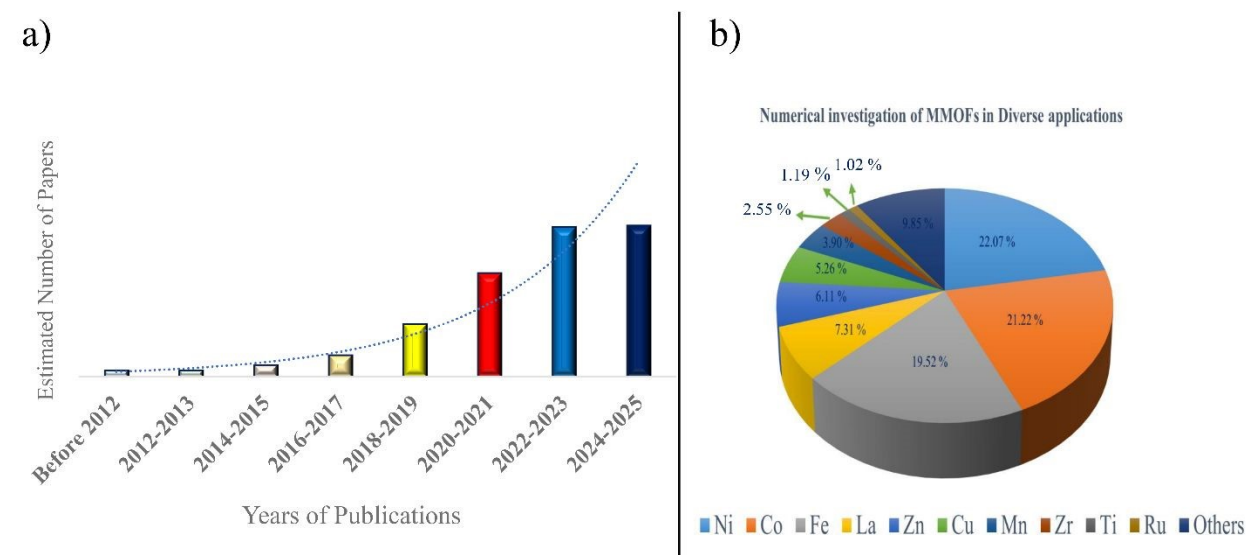


Figure 1. a) Plot showing the gradual increase of reports on MMOFs since 2004 based on Web of Science Database (accessed in Nov. 2025); b) Percentage contribution of each metal in the composition of MMOFs during the period 2019-2025.

This review focuses exclusively on MMOFs reported in recent years, offering a comprehensive analysis of the challenges in their synthesis, the impact of various metals on MMOF structures, their unique properties, and the metal-metal interactions. Besides their synthesis, the present review provides a detailed exploration of the diverse applications of MMOFs, categorized by metal composition, and examines the contribution of each of these metals to the structure and functionality of the resulting MMOFs. Considering the vast chemical space, this area of MMOFs remains relatively underexplored, making this review valuable for understanding the remarkable MMOF properties and how metal characteristics determine their applications. Moreover, it presents a fresh perspective on MOF engineering for targeted applications, indicating the rules for the selection and integration of specific metals in MMOF. Finally, this work highlights the huge potential of MMOFs and opens new avenues for research, offering significant opportunities for future growth and innovation in this rapidly evolving field. Also, application sections with M-based MOFs (M: Fe, Ni, Co, Zn, La, Zr) can give us clear insights into the role of each metal ion in diverse MMOFs applications along with their efficiency.

2. Synthetic Routes for MMOFs

The synthetic route of a given MMOF is a critical factor influencing their performance in diverse applications, since, depending on the preparation procedure, MMOFs with even the same chemical composition can exhibit contrasting efficiency. Recent research has employed various methods to enhance durability, stability, and activity by forming robust structures. Several reviews have specifically addressed these synthetic procedures, highlighting the importance of the synthesis on the properties.^{24, 25} In this review, we will discuss some of the most widely used, reliable synthetic routes to provide a clearer understanding of MMOF structures.

Before exploring the applications of MMOFs, it will be commented how the synthesis method can influence the properties of these materials, affecting later to their performance. Direct synthesis methods, such as *in situ*, cluster, and nickel foam strategies, are among the most widely used synthetic procedures, and they will be described earlier in this review. Post-modification routes, including core-shell, insertion, and exchange strategies, are less general synthetic approaches, more specifically tailored towards a particular application, providing further versatility in MMOFs research.



Besides being at the metal nodes, the metallo-ligand approach, where metals are integrated into the linker, also provides an effective strategy for synthesizing MMOFs. This method is particularly advantageous for energy conversion systems, where enhanced porosity, robustness, and functional properties are required. Additionally, the review also covers procedures to obtain MMOF derivatives, particularly employed for energy applications. Transformation of MMOFs into derivatives will also be succinctly covered, as they offer materials with larger surface areas and increased active site accessibility compared to alternative synthetic routes of these derived materials. Figure 2 illustrates the synthesis routes covered in the present review, emphasizing their impact on MMOF performance and expanding their applicability across various fields. Structural changes in MMOFs occur before synthesis (pre-modification) or after (post-modification). Derived routes can also relate to various modifications that take place in high temperatures to form MMOF derivatives. Metallo-ligand approaches form part of a unique MMOF synthesis pathway; the section explains how linkers containing metals within their structure can be used in the synthesis of MMOFs.

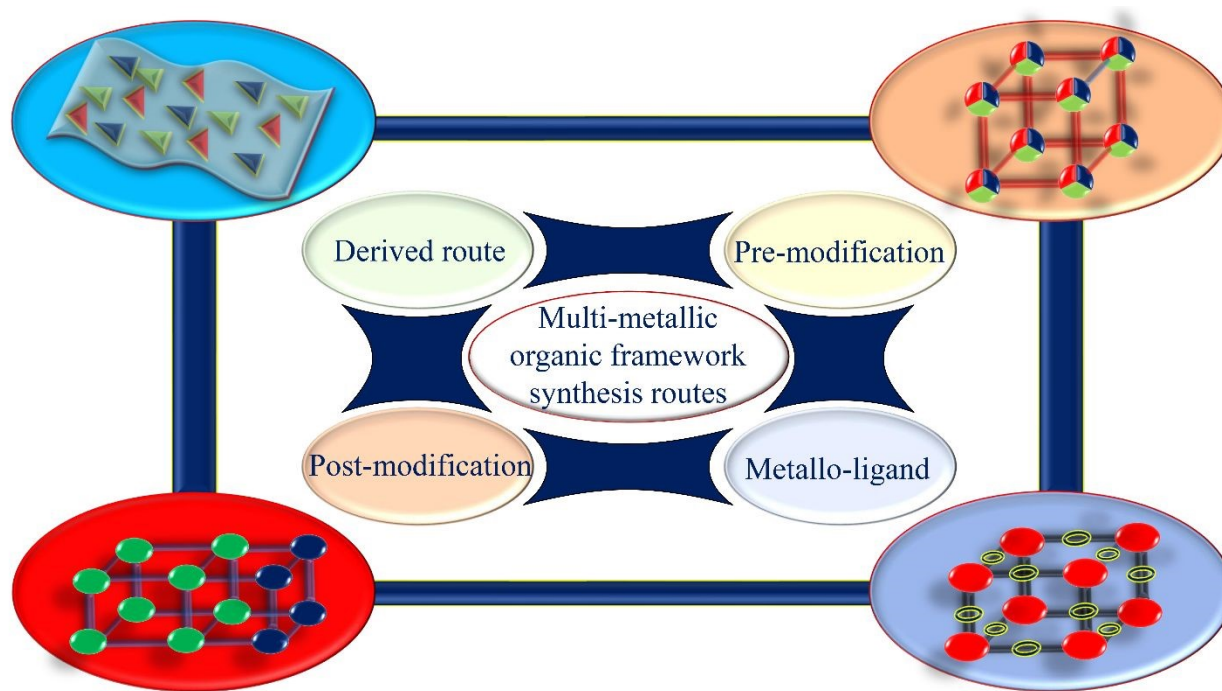


Figure 2. Most employed synthesis methods for the preparation of MMOFs.

2.1. Synthesis from Special Precursors



The synthesis of MMOFs, adapting the general procedure of the SMOF relatives, starting from precursors of the wanted metal elements in specific ratios required in the metal nodes and the corresponding organic linkers using reflux, hydrothermal, or solvothermal techniques, has been extensively employed. Although this approach has limitations, such as uneven metal distribution in nodes, it is straightforward and remains the most frequent procedure. This route allows for the synthesis of MMOFs with various structures and morphologies, including foam-like nano-octahedra, hierarchical 3D frameworks, multi-shelled hollow structures, and 2D morphologies. Derived MMOF structures generated through pyrolysis of the direct synthesis are also discussed in the last sections. As illustrated in Figure 3, the reports on the direct synthesis of MMOFs can be classified into three methods of MMOF synthesis using special precursors. They are discussed in the sequel.

2.1.1. In Situ Synthesis

In situ synthesis is one of the most widely employed methods for MMOFs. It consists in using, in a conventional synthesis initially reported for an SMOF, a mixture of metal salts in specific molar ratios together with the corresponding organic linker to form MMOFs. Despite its simplicity, this method is influenced by factors such as the different reactivity of the metal ions, coordination environment, and pH. This often results in variability in the incorporation of metal ions in the lattice, with some metals failing to enter the MOF structure. Additionally, this method often requires high energy and is irreversible, meaning that incorporation of one metal ion cannot be reversed by the second metal due to its lower affinity. These negative factors can limit the applicability of the in-situ incorporation of two or more metal ions in the structure. An example of in situ synthesis is the preparation of UiO-66(Zr/Ti) using specific molar ratios of titanium and zirconium salts combined with 1,4-terephthalic acid (H_2BDC) in a one-pot synthesis process.⁴⁷

2.1.2. Cluster Synthesis Route

The cluster synthesis route is another straightforward synthesis method of MMOFs, that is based on the controlled formation of multi-metallic metal clusters in a pre-synthesis phase. In this method, metal salts are first combined following specific protocols to form clusters of various metals. Organic linkers then reacted to precise ratios with these preformed clusters to form MMOFs. As an example, the PCN-250-Fe₂M MMOF is synthesized in two steps. First, Fe₂M(μ_3 -



$\text{O})(\text{CH}_3\text{COO})_6(\text{H}_2\text{O})_3$ clusters are prepared, and then these clusters are reacted with azobenzene tetracarboxylate (H_4ABTC) to produce the PCN-250 structure.⁴⁸

2.1.3. In Situ Growth on Nickel Foam

The in-situ growth method on nickel foam (NF) has recently gained considerable popularity, especially in energy-related applications, such as electrocatalysis.⁴⁹ This procedure enhances electrical conductivity and performance by achieving a good integration of the MMOF and the conductive NF electrode. This integration is much superior to deposit the preformed MMOF on NF that does never reach similar conductivity.

The process begins by cleaning NF with acid or other treatments to remove surface oxides. Clean NF serves as a Ni source, and it is combined in an autoclave with additional metal salts and linkers to form MMOFs. For example, the FeCoNiMn-MOF/NF was synthesized by washing NF with a mixture of HCl, water, and ethanol under sonication. Subsequently, metal salts (Fe, Co, Mn) and 2,3-dihydroxyterephthalic acid as a linker were added to the autoclave to form the MMOF structure.⁵⁰ These synthesis methods employing preformed metal clusters analogous to the metal nodes of the MMOF highlight the versatility and adaptability of MMOF fabrication, enabling the design of materials tailored for specific applications.

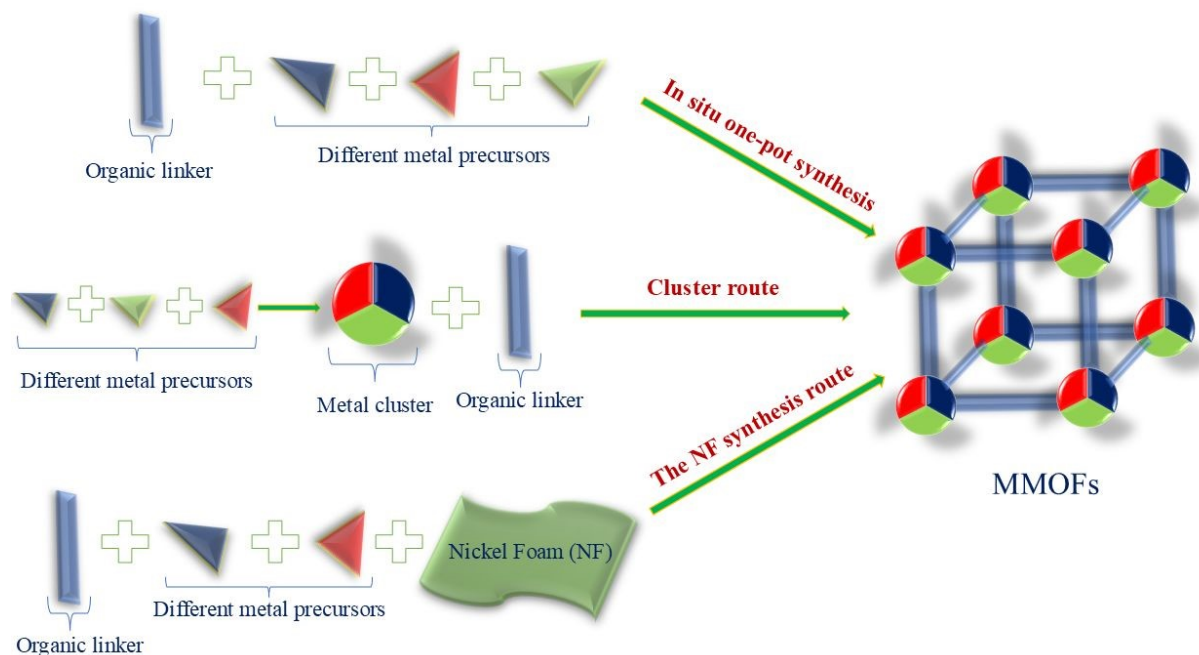


Figure 3. Procedures for the direct synthesis of MMOFs in which several metals are incorporated simultaneously, two of them employing special precursors.

2.2. Metallo-Ligand Approach

The metallo-ligand approach represents a recent and innovative method for synthesizing a new MMOF synthesis route tailored for diverse applications. This technique involves using materials such as ferrocene or metalloporphyrins as organic linkers, allowing for the incorporation of mixed-metal ions into the MOF structure at various defined lattice positions.

In this approach, metal salts in specific ratios are combined with metallo-ligands to form MMOFs in which at least one metal is not in nodal positions (Figure 4). The material can then be utilized for various applications, particularly related to catalysis and sensing. Additionally, this method can be integrated with other previous synthesis techniques. For example, metal clusters can be combined with metallo-ligands to fabricate MMOFs, or NF can serve as a precursor and Ni source alongside the metallo-ligand. Although this synthesis route remains relatively underexplored, initial studies have demonstrated its potential for specific applications. For instance, defective $\text{NiFc}'_x\text{Fc}_{1-x}$ MOFs (Fc and Fc': substituted ferrocenes as metallo-ligands) were synthesized by varying the ratios of Fc or Fc' and Ni. The metal sources in these syntheses can include salts or meshes, as illustrated in Figure 5.⁵¹

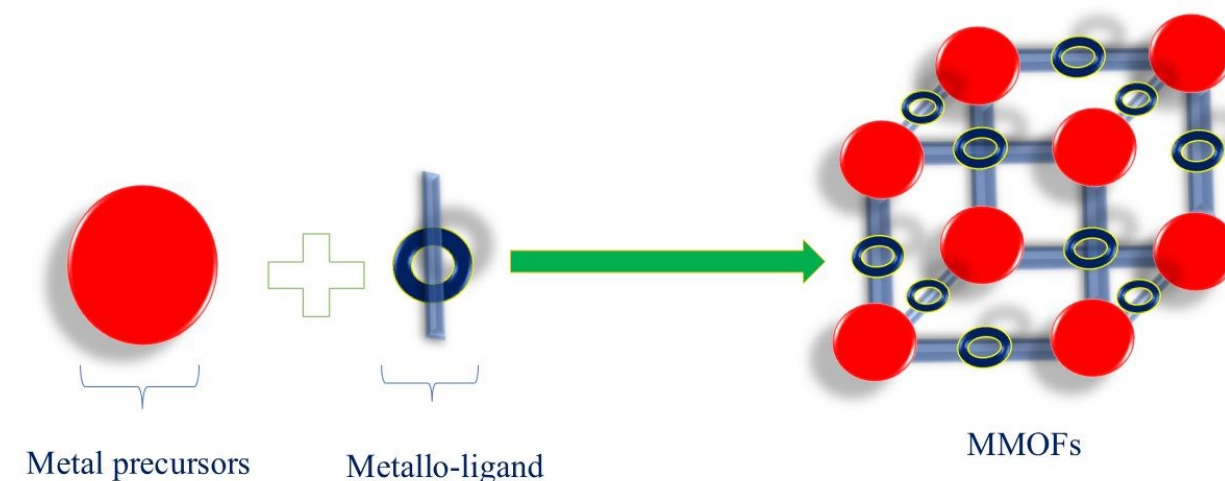


Figure 4. Preparation of MMOFs using the metallo-ligand approach. It should be noted that metals are present at the nodes as well as at the ligands.

The metallo-ligand approach offers promising opportunities to expand the diversity and functionality of MMOFs, particularly when combined with other advanced synthesis techniques.

Further investigation into this method could unlock new possibilities for designing MMOFs with tailored properties for specific applications.

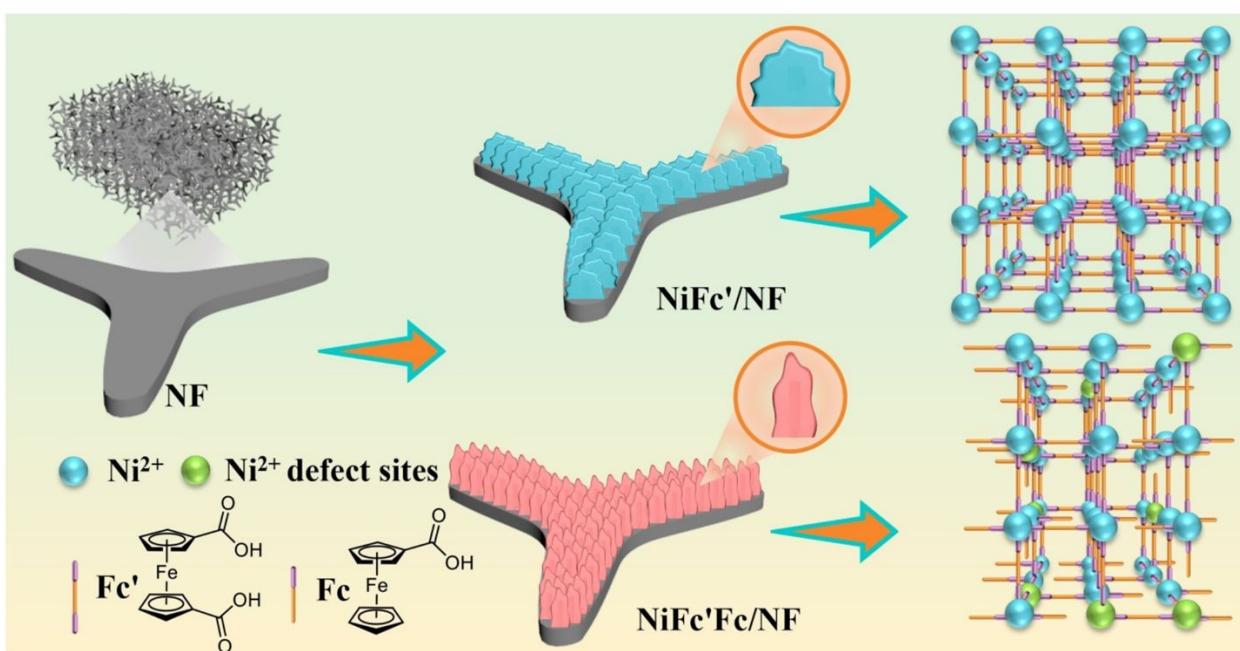


Figure 5. Synthesis route of $\text{NiFc}'_x\text{Fc}_{1-x}$ MMOF series grown on NF for OER electrocatalysis. Reproduced with permission from ref.⁵¹ Copyright 2023 Wiley.

2.3. MMOF-Derived Materials

MMOF-derived materials have garnered significant attention for their versatility in applications, particularly in electrocatalysis and electrical energy storage systems²⁸. These materials are formed when synthesized MMOF precursors are exposed to controlled transformation, resulting in changes in composition and structure, leading to unique MMOF-derived materials. The most common procedure to obtain MMOF derivatives is high-temperature treatment under an inert atmosphere, which results in the graphitization of the MMOF organic linker. This process can generally result in a carbon matrix acting as support for fine metal alloy nanoparticles.

The morphology of derived MMOFs can vary widely, encompassing carbon nanoflowers, nanoflakes, porous frameworks, and hollow structures. These morphologies are influenced by factors such as the initial morphology of the MOFs, pyrolysis temperature, and other external and internal conditions. A growing area of interest is the synthesis of 2D-derived MMOFs, which again offer unique advantages in energy applications due to their notable electrical conductivity.

2.3.1. 2D Structures in MMOF Derived Materials

Two primary methods are used to synthesize 2D MOF structures (nanosheets), either the top-down or the bottom-up routes. The top-down approach involves the exfoliation of 3D MOFs into 2D nanosheets by breaking weak interactions, such as hydrogen bonds, π - π stacking, and van der Waals forces. These weak bonds are disrupted through chemical or physical treatments. In contrast, the bottom-up route generally uses surfactants and modulators to control the thickness of the nascent particles during the crystallization of the MMOF, resulting in 2D structures by arresting the growth in the z-direction.

Subsequently, when the 2D MOFs are subjected to pyrolysis, they can form, among other possibilities, layered double hydroxides (LDHs), which are particularly valuable for energy applications due to their enhanced conductivity, cost-effectiveness, and ease of synthesis. LDHs derived from 2D MMOFs have been widely studied for their performance in energy-related technologies. 2D MMOF-derived materials are particularly attractive due to their larger specific surface area and easy site accessibility, which enhances their functionality across a range of applications. In electrochemical systems, they are especially promising because their enlarged surface area improves electrolyte-material interactions, thereby enhancing their performance.

One notable example of MMOF-derived material for energy application is the trimetallic $\text{Co}_{0.2}\text{Fe}_{0.8}\text{Ni}$ -OCNF (OCNF: oxide carbon nanoflower), which can be synthesized from trimetallic Hofmann nanoflower MOFs. After the spontaneous self-assembly of the 2D MOF sheets as nanoflowers, this morphology remains upon pyrolysis. This specific structure creates a large population of accessible active sites, making these materials highly effective for electrocatalysis.⁵² In another example, bimetallic Fe_2Co -MOF was employed as a precursor to obtain CoFe_2O_4 oxides at 500 °C, and nanoporous carbon (NPC) at 800 °C (Figure 6). This derivative showed the enhanced specific capacitance, thus beneficial for supercapacitor applications.⁵³ Furthermore, Figure 7 illustrates conventional synthesis routes for MMOF-derived materials, showcasing their utility in energy applications. By engineering the structure of MMOFs and transforming them into derivatives, it has been possible to obtain materials with enhanced performance and site accessibility, making them among the best candidates for advanced energy technologies.



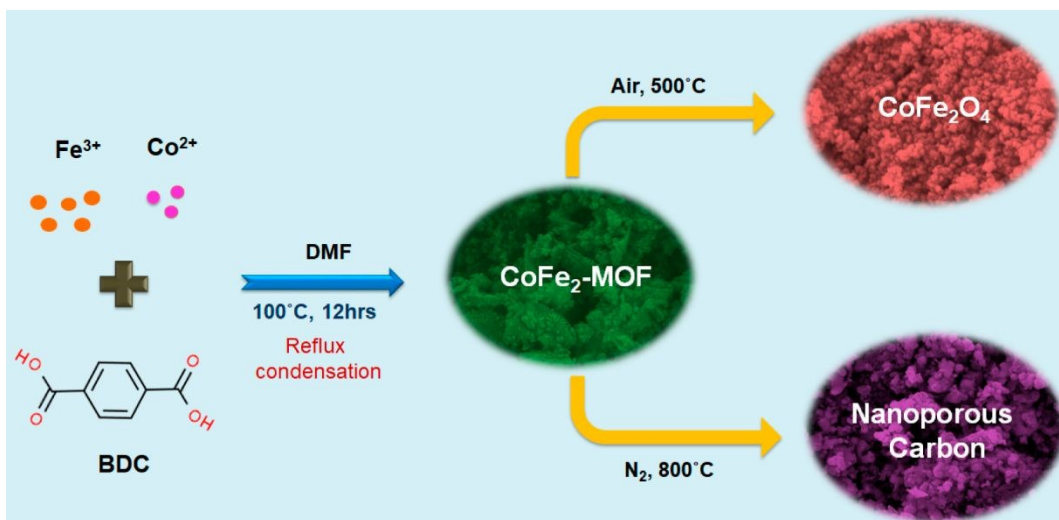


Figure 6. Synthesis of CoFe_2O_4 and NPC solids by pyrolysis of bimetallic MOF for supercapacitor applications. Reproduced with permission from ref.⁵³ Copyright 2024 American Chemical Society.

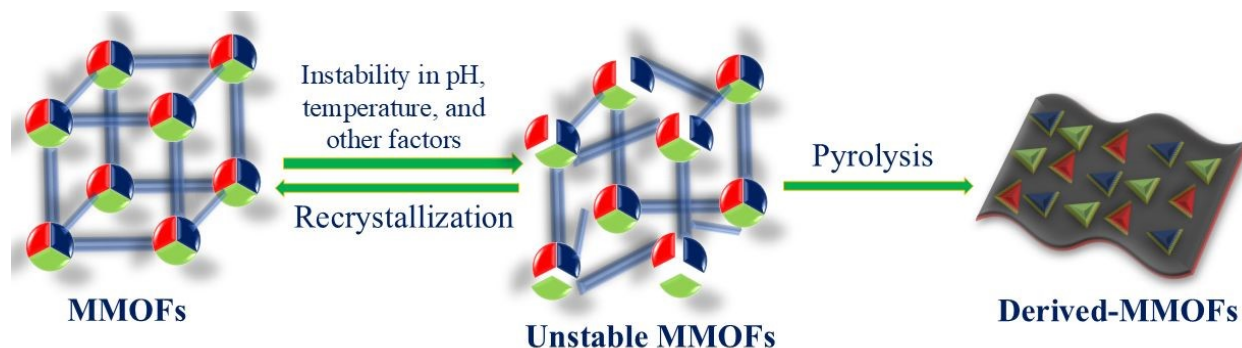


Figure 7. Preparation of MMOF-derived materials from MMOFs as the precursors.

2.4. Post-Synthesis Strategies

Post-synthetic modifications start from SMOF that are subsequently treated to introduce additional metals. This approach encompasses various modification methods tailored for specific applications. The post-synthesis MMOF preparation generally can take place through one of the following three main approaches, i.e., either core-shell, or insertion, or exchange methods. Figure 8 summarizes the post-synthetic modification methods.

2.4.1. Core-Shell Route

Although still poorly explored for MMOF synthesis, the core-shell route involves combining a MOF core with a MOF shell to form MMOFs in which two or more metals are in the

material, but at different positions. This method is advantageous for regulating the spatial distribution of the metals in the MMOF, as it is possible to adjust the sizes of the shell and core, resulting in highly porous materials. However, it is challenging to obtain single crystals from the MOF shell, which limits its use in certain applications.²⁵ Also, core-shell can ensure uniform nucleation and strong adherence between the MOF and substrate, which can be expected that it will be further applied for the synthesis of MMOF in the future.⁵⁴

2.4.2. Insertion Methods

The insertion of metals into pre-formed MOF structures can occur through three primary strategies, namely:

- Functionalized Group Incorporation. Functional groups can be introduced either within the MOF cavity or on its surface. These groups coordinate with a metal diffusing to the interior of the crystal to form MMOFs.
- Open Metal Site Provision. Unsaturated coordination sites in the MOF structure enable the incorporation of secondary metals, resulting in MMOF formation.
- Metal Penetration. By controlling the molar ratio of metal salts, secondary metals can be introduced into the structure, creating MMOFs.

2.4.3. Exchange Methods

The exchange methods involve replacing existing metals or ions within the MOF structure by ions of other elements. Since the metal-linker coordination bond is reversible, additional metals can be, in principle, introduced into the structure by metal ion exchange, exposing performed MOF to a high concentration of other metal salts, creating in this way MMOFs. There are three primary ways to achieve this exchange:

- Demetallation-Addition Route. Initially, SMOF is synthesized. Then, a certain proportion of the metal atoms is removed (demetallation) to create structural vacancies, allowing additional metals to penetrate the structure and form MMOFs.
- Ion Exchange. Metal ions within the SMOF structure are directly exchanged with other ions, creating MMOFs.



- Etching Procedure. If ion exchange occurs only on the MOF surface rather than throughout the structure, etching can be applied. This approach makes possible a certain control on the morphology and crystallinity of MMOFs.

While these post-modification methods are versatile and suitable for fine-tuning the morphology and crystalline properties of MMOFs, they present several challenges. For instance, doping, inserting, or exchanging metals may damage MOF crystallinity, which can be detrimental or beneficial depending on the specific application. These merits and limitations are further discussed in the applications section (Figure 8).^{13, 27, 29}

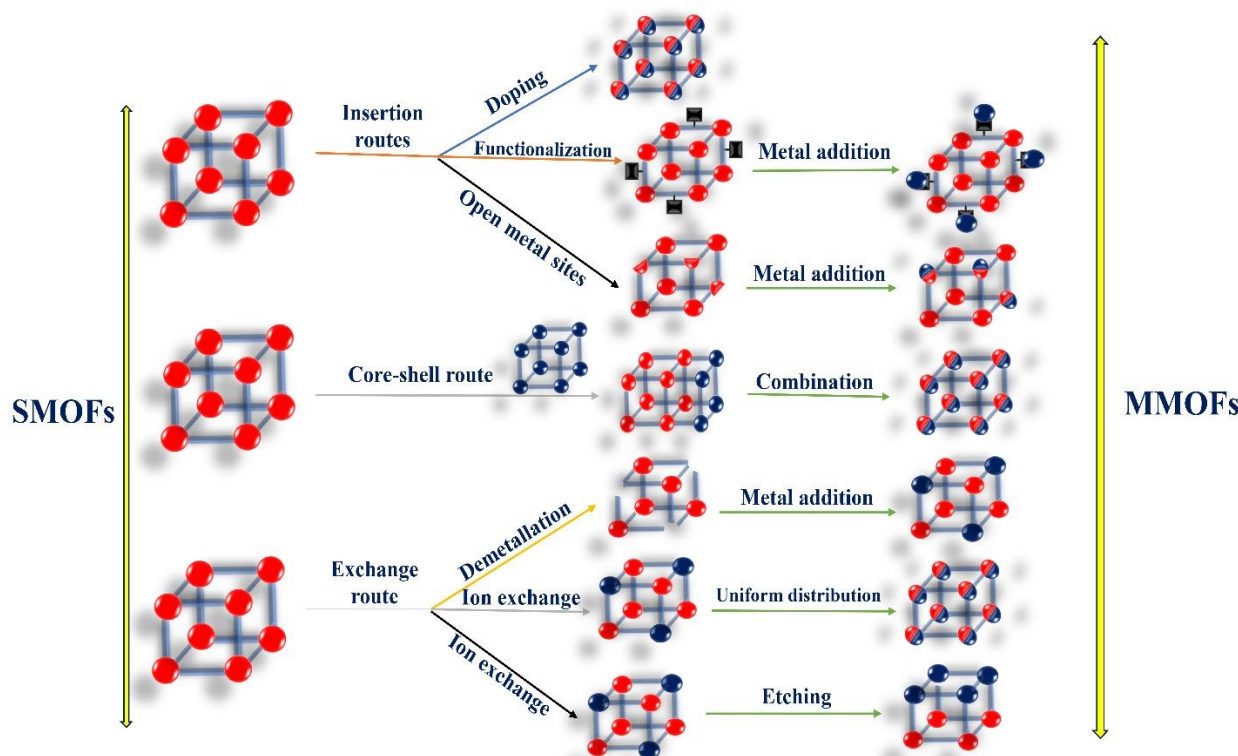


Figure 8. Different post-synthesis strategies for the preparation of MMOFs.

3. Applications

This section explores the applications of bimetallic MOFs and MMOFs as well as MMOF-derived materials across various domains, including electrocatalysis, electrical energy storage, catalysis, and photocatalysis, as well as sensing, medicine, removal of pollutants and adsorption. Each application is critically reviewed, focusing on the role played by the presence of various metals and their quantitative impact. Emphasis will be placed on the efforts to rationalize the



results by advanced characterization, such as X-ray photoelectron spectroscopy (XPS), microscopy, electrochemical measurements, density functional theory (DFT) calculations, and other methods to understand the reasons for the synergy and modification of the electronic structures. While other reviews have covered MMOFs in general applications, this work emphasizes the specific contribution and synergy of mixed metals, resulting in improved MMOF performance.²⁹⁻³¹

The most extensively studied applications of MMOFs are in energy-related fields, particularly electrocatalysis and electrical energy storage. These areas dominate due to the general observation of synergistic effects between metal ions, the development of cost-effective alternatives to precious metals by combining abundant metals, and the high electroactive potential of materials based on Ni, Fe, and Co. Despite significant progress, challenges, such as synthesis complexity, scalability, and stability, continue to pose limitations for broader adoption in other fields.

Electrocatalysis in MMOFs spans diverse reactions, including water splitting, OER, HER, oxygen reduction reaction (ORR), nitrogen reduction reaction (NRR), urea oxidation reaction (UOR), and CO₂ reduction (CO₂R), among the best studied. Water splitting involves two redox processes: OER occurs at the anode and HER at the cathode. While HER is relatively efficient, OER is hindered by thermodynamics and high kinetic barriers due to the sluggish four-electron transfer processes, resulting in increased overpotential. MMOFs with non-precious metals, offer an alternative to electrodes based on expensive Ru and Ir catalysts for OER by diminishing overpotentials and Tafel slopes, increasing stability, and Faradaic efficiency.⁵⁵⁻⁶² In one example of MMOFs circumventing OER to reach enhanced H₂ production, HER was coupled with glycerol oxidation reaction (GOR), which results in an enhanced HER efficiency, while yielding valuable by-products, like formic acid. ORR is pivotal for zinc-air batteries; the process requires four-electron reduction. More recent interest is focused on selective two-electron reduction, since it could enable an eco-friendly, electrochemical route for H₂O₂ production from air without the need for H₂. It appears that MMOFs and derived materials are among the best 2-electron ORR electrocatalysts.^{63,64} Electrochemical CO₂R with MMOFs provides a sustainable pathway for CO₂ conversion using green electricity under mild conditions, reducing the need for high temperatures or pressures typically required in thermal catalysis. Although still underexplored, MMOFs have



shown considerable potential for driving product selectivity in CO₂R to valuable products.⁶⁵ UOR is an anodic reaction requiring a lower potential (0.37 V) than OER, making it energetically favorable to be coupled with HER with lesser electrical energy consumption. MMOFs enhance the sluggish six-electron kinetics of UOR, improving efficiency.^{66, 67} Breaking the N≡N bond to convert N₂ into NH₃ demands significant energy due to the bond stability. MMOFs, acting as Lewis acids provide active sites for NRR, facilitating this transformation.^{68, 69}

MMOFs are effective in supercapacitors and batteries, addressing key challenges related to high specific energy storage and high-power density. Known for their fast charge-discharge rates and high-power density, supercapacitors must overcome their low energy density limitation. MMOFs help expand the potential window and specific capacitance, boosting energy density.⁷⁰⁻⁷⁶ Lithium-ion batteries (LIBs) have high energy density but require optimization for power density. MMOFs enhance LIB performance by balancing these two factors and improving specific capacity.

MMOFs are effective heterogeneous catalysts, with better performance than the corresponding SMOFs. MMOFs have shown promise in oxidation reactions, CO₂ transformations, and other catalytic processes factors such as turnover number (TON), turnover frequency (TOF), stability and yield determine their catalytic efficiency.⁷⁷⁻⁷⁹ Photocatalytic applications of MMOFs include water splitting, CO₂ reduction, and dye degradation. Their effectiveness is influenced by factors such as light absorption, band energy, and reaction yield.^{16, 80-83}

The performance of MMOFs in sensing applications, particularly using electrochemical or fluorometric response, is evaluated based on the limit of detection (LOD), which reflects the lowest concentration at which a substance can be detected. Challenges include the uniform distribution of metals and the development of suitable synthesis procedures.⁸⁴ Key challenges in pharmaceutical applications include biocompatibility, toxicity, and synthesis complexity. The cytotoxicity of different metal elements poses safety concerns, while large-scale production requires maintaining uniformity and structural integrity.^{85, 86} MMOFs are also employed in removal, separation, and adsorption applications. Challenges in these areas include stability, uniform metal distribution, and minimization of environmental impacts.⁸⁷



Energy-related applications, particularly electrocatalysis, dominate the field of MMOFs due to the general observation of synergistic effects between metals and the higher electrical conductivity of pyrolysis-derived MMOFs. Non-precious metals like Ni, Fe, and Co are preferred candidates due to their cost-effectiveness and electrocatalytic activity. Less-studied applications, such as medicinal, sensing, and pollutant removal, are emerging areas with growth potential, requiring further research and development. This review underscores the versatility of MMOFs and highlights areas for future investigation to take advantage of MMOF properties in various fields. The following sections will describe MMOFs and their derivations, classified based on the metal element presented in the highest proportion in the composition of the material.

4. Iron-based MMOFs

Among the various types of MMOFs, Fe-based frameworks have seen rapid development and have attracted considerable interest from the scientific community. As the fourth most abundant element in the Earth's crust, Fe is widely available and cost-effective, making Fe-based MOFs an attractive option for various applications. Furthermore, low toxicity of Fe enhances its suitability for pharmaceutical uses, while its paramagnetic properties make Fe(III)-based MOFs highly effective in magnetic resonance imaging. Beyond pharmaceuticals, Fe-MMOFs find applications in sensing, catalysis, and other areas. In MOFs, Fe^{3+} ions act as Lewis acids, coordinating with oxygen-containing ligands that serve as Lewis bases. This robust coordination bond between Fe^{3+} and oxo ligands provides Fe-MMOFs with excellent stability in both aqueous and organic solvents, as well as high thermal and chemical resilience. When combined with other metals, Fe-based MMOFs benefit from the unique properties of each metal, expanding their potential applications, as will be discussed below.⁸⁸⁻⁹⁰

The incorporation of additional metals into Fe-MMOFs can eventually result in an enhancement of their surface area, pore size, and density of open metal or catalytically active sites, improving in this way their drug delivery capabilities. Enlarged pores in these frameworks facilitate larger drug adsorption capacity and release efficiency. As an example, M-MIL-100(Fe), a bimetallic MOF, was employed by Muder Al Haydar et al. as a carrier of the drug aceclofenac, which has low solubility in aqueous media. Compared to monometallic MIL-100(Fe), the incorporation of a second metal expanded the MOF pore size, enabling enhanced drug adsorption,



and was beneficial for providing an adequate dose within the body. The aceclofenac loading capacity of MIL-100(Fe) was 27%, whereas the loading capacity was 37% in Ca(I)-MIL-100(Fe), 57% in Mn(II)-MIL-100(Fe), and 59% in Zn(II)-MIL-100(Fe), which exhibits the superior activity of bimetallic MOF compared to monometallic MOF. This highlights the superior performance of Fe-based MMOFs in drug delivery compared to their monometallic counterparts due to the higher loading of Fe-MMOFs.⁹¹

Fe-MMOFs demonstrate excellent electrochemical sensing properties due to their two available oxidation states, Fe^{2+} and Fe^{3+} , and their synergistic effect with other metals can better induce selectivity toward detection.^{92, 93} The swing between these two states enables enzyme-like catalytic activity, making Fe-MMOFs valuable components in biosensing platforms. In this context, a Fe_3Ni -MOF (BDC as linker) synthesized by Wang and coworkers demonstrated peroxidase-like activity. Also, Ni can buttress peroxidase-like activity and improves electron transport between H_2O_2 and 3,3',5,5'-tetramethylbenzidine (TMB), facilitating oxidation of Fe^{2+} to Fe^{3+} and generating more $\cdot\text{OH}$ radicals. This improvement enabled ultra-sensitive detection of H_2O_2 , which was further used to develop a glucose detection system.⁹² In another case, Yuan et al. developed a trimetallic MOF, FeCoNi -MOF (BDC as linker), for detecting thiophenol. XRD pattern of FeCoNi -MOF after immersing in aqueous solution at pH 2, 7, and 12 for 24 h showed no characteristic changes in its pattern, thus showing its stability for sensor application. This MOF exhibited both peroxidase- and oxidase-like activity, catalyzing the oxidation of TMB and directly oxidizing chromogenic substrates into oxTMB, resulting in a blue product. The synergistic effect and efficient electron transfer among Fe, Co, and Ni make FeCoNi -MOF a highly sensitive and stable sensor for detecting biomarkers in water samples. The intensity of the EPR signal for trimetallic MOF is stronger than for bimetallic FeCo , FeNi , and CoNi -MOFs and the bimetallic counterparts have a stronger EPR signal than the monometallic Fe, Co and Ni-MOFs, indicating the synergistic effects among Fe, Ni, and Co in FeCoNi -MOF for activation of H_2O_2 . Its rapid reaction speed demonstrated the potential of Fe-MMOFs for colorimetric sensing applications.⁹⁴ In another instance, $\text{NH}_2\text{MIL-101(Fe)}$ @Ag exhibit a nearly 100% bactericidal activity against high concentrations of *Staphylococcus aureus* and *Escherichia coli*. DFT simulations have indicated that electrons are transferred from Ag to Fe-MOF due to lower Ag work functions and higher Fermi energy compared to Fe-MOF. Also, incorporation of Ag has a little impact on the adsorption



energy of Fe-MOF, which indicates that O_2 can be adsorbed on the $NH_2MIL-101(Fe)@Ag$ surface and produce more reactive oxygen species (ROS) upon irradiation at 880 nm.⁹⁵

Fe-MMOFs are among the most extensively studied materials for electrocatalytic OER due to their synergistic effects with other metals, that can result in highly efficient active sites.⁹⁶⁻⁹⁹ The ability to release protons and alter the MOF structure significantly impacts the active site density and overall catalytic performance. The mixed valence states of Fe, such as Fe^{2+} and Fe^{3+} , contribute to improved electronic interactions with other metal ions, enabling enhanced intermediate production (e.g., *OOH in OER) with lower energy barriers. In one example, Co_4Fe_6 -MOF (BDC as linker) demonstrates low overpotential (241 mV at 10 mA cm⁻²) and a Tafel slope of 30.1 mV dec⁻¹ for OER.¹⁰⁰ The enhanced OER activity is attributed to the optimal Fe/Co ratio that increases adsorption/desorption processes and decreases crystallinity, yielding abundant active sites.¹⁰⁰ DFT calculation indicates that defect formation energies decrease as the Co/Fe ratio diminishes, corresponding to the introduction of defects and disordered atom architectures in the MOF framework. Defect structure can augment the number of active sites and high charge transport, and the incorporation of Fe ions can effectively optimize the electronic structure of metal Co nodes, thereby facilitating adsorption/desorption of OER intermediates. Also, the Co_4Fe_6 -MOF shows a higher TOF value (1.04 s⁻¹) than the others, indicating its reinforced intrinsic activity in the OER process. In another example, PCN-Fe₂Co-Fe₂Ni, MMOF of 3,3',5,5'-azobenzene tetracarboxylic acid (H₄abtc) as linker having simultaneously two different mixed metal clusters in the structure, either $Fe_2Co-m_3O^{6+}$ or $Fe_2Ni-m_3O^{6+}$, shows an overpotential of 271 mV and a Tafel slope of 67.7 mV dec⁻¹.⁴⁸ Also, no changes in the PXRD patterns of PCN-Fe₂Co-Fe₂Ni in a broad range of pH values from 1 to 14 demonstrate its stability. The higher OER activity was related to the lower ionization potential of the mixed metal cluster, increased electron density, and synergistic effects between Co, Ni, and Fe.⁴⁸ The density of states (DOS) of Co and Ni 3d orbitals for mixed-metal mixed-cluster MOFs exhibits a weaker negative shift compared to the PCN-250-Fe₂Co and PCN-250-Fe₂Ni counterparts, which indicates that incorporation of another Fe₂M cluster decreases the energy of Co and Ni atoms and leads Co and Ni atoms receiving higher electron density in PCN-Fe₂Co-Fe₂Ni. Also, a high TOF value of 0.068 s⁻¹ at 350 mV reflects their excellent intrinsic activity of mixed-cluster MOF compared to the PCN-250-Fe₂Co (0.024 s⁻¹) and PCN-250-Fe₂Ni (0.038 s⁻¹). In another illustrative example, the Fe-MMOF derivative of MIL-88A(Fe) (fumaric



acid as linker) was prepared under hydrothermal conditions in the presence of $\text{Ni}(\text{NO}_3)_2$ and $\text{Ce}(\text{NO}_3)_3$ and urea. The resulting 30%CeNiFe-LDH obtained by etching of a CeNiFe MMOF exhibits superior OER activity due to Ce strong affinity for oxygen donors and its synergistic interaction with Fe and Ni, facilitating electron transfer.¹⁰¹ Although 3d orbitals of Ni and Fe have a critical role to play for OER activity, Fe 3d orbitals cross the EF, supporting the stabilization of O-related species while the Ni 3d band synergy with Fe and Ce at the commensurate positions can induce high electroactivity during OER. Meanwhile, the Ce 4f orbitals overlap with Ni and Fe 3d orbitals, which can modulate the electronic structure and buttress electron transfer throughout the catalyst surface. In one of the examples, MIL-53(Fe) (BDC as linker) was modified mechanochemically by adding $\text{Ni}(\text{OAc})_2$ and $\text{Co}(\text{NO}_3)_2$. The ball milling decreases the particle size of MIL-53(Fe), while the Ni and Co metal salts are deposited on the external surface of the MOF crystallites. The resulting trimetallic Fe/Ni/Co MOF achieves a low overpotential of 180 mV (10 mA cm⁻²) due to Fe-O-Ni/Co bonding, as supported through XANES and EXAFS analyses.¹⁰² Regarding reported examples of V-MMOFs in electrocatalytic water splitting, it was found that the presence of V was favorable due to the multiple valences states that it can present, optimizing the binding energy of redox reaction intermediates, lowering overpotential and enhancing the electrocatalytic activity. For instance, various M_2V -MOFs ($\text{M}=\text{Zn}$, Co, Fe, Mg, and Ni, BDC as linker) having trimetallic clusters were explored for electrolytic water splitting in 1 M KOH.¹⁰³ Interestingly, these M_2V -MMOFs were prepared by the so-called pore-space-partition (PSP) strategy that consists of performing the solvothermal synthesis of the mixed metal MOF adding, besides the BDC linker, 2,4,6-tris(4-pyridyl)-1,3,5-triazine.¹⁰³ The bulky triazine linker occupies the pores generated in the framework by the coordination of the M_2V metal node and BDC dividing the internal space into three compartments while adding further structural robustness due to the additional coordination with the rigid triazine molecules. The electrochemical data show that the OER activity of Fe_2V -MOF has a calculated TOF of 0.0243 s⁻¹ and R_{ct} of 0.67 Ω measured by EIS characterization, resulting in a better electrochemical activity than the other M_2V -MOFs having other metals accompanying to V and even than the commercial IrO_2 catalyst which has overpotential of 330 mV.¹⁰³ Furthermore, at the scan rate of 5 mV/s, both Fe_2V -MOF (overpotential=198 mV at current density 10 mA cm⁻²) and Mg_2V -MOF (overpotential=195 mV at current density 10 mA cm⁻²) have great performance for HER in alkaline media. Notably, Mg_2V -MOF also exhibits HER activity in acidic media having an overpotential of 215 mV at a



current density of 10 mA cm^{-2} . Also, Mg_2V -MOF has the highest performance of C_{dl} (2.38 mF cm^{-2}) among M_2V -MOFs. Besides a remarkable activity, both Fe_2V -MOF and Mg_2V -MOF exhibit long-term stability in a current density of 10 mA cm^{-2} for 12 h after 5000 cycles. The superior activity and stability of Fe_2V -MOF and Mg_2V -MOF were rationalized as derived from a combination of positive effects, including: **i**) higher valence states introduced by the presence of V should improve the electrostatic interactions with the linkers and establish a synergistic effect with the other metal ions at the node, as can be experimentally assessed by XPS analysis, **ii**) higher hydrophobicity that should favor bubble evolution during water electrolysis by decreasing the surface tension, **iii**) the additional triazine linker at the pore space should stabilize further the structure, particularly at the pH operation conditions under electrochemical stress, and **iv**) decrease in Gibbs free energy of the rate-determining transition state due to effect of vanadium stabilizing the reaction intermediates that result in a better electrocatalytic activity.¹⁰³ In another instance, tetrametallic NiFeCoV -MOF-74 demonstrates overpotential of 266 mV at a current density of 10 mA cm^{-2} which is superior to the bimetallic and trimetallic counterparts. Due to the effective synergy among tetra-metals, electron transport from V^{4+} to Ni^{2+} and Co^{2+} is facilitated, and NiOOH and CoOOH on the surface act as the active sites.¹⁰⁴

Furthermore, Fe-MMOFs have significant potential in supercapacitors and batteries. The synergistic effects of Fe with other metals enhance OH^- adsorption, charge transfer, and conductivity.¹⁰⁵ In one example, the solid derived from CoFe_2 -MOF (BDC as linker) demonstrates improved storage capacity due to synergistic interactions, increased active sites, and higher conductivity.⁵³ The electronegativity facilitates the charge transfer with the electrolyte, which is a crucial process for Li^+ ion batteries.

Fe-MMOFs serve as efficient catalysts due to their Lewis acidity, which enhances the activity and selectivity of catalytic processes. The presence of Fe in MOF structures results in high TOF values and reaction rates by decreasing electron density around neighboring metal ions, and oligomerization of Fe-oxo clusters is disfavored by the interaction with other metal ions. In one report, FCN-K MMOF derivative obtained by N_2 calcination at $550 \text{ }^\circ\text{C}$ of Fe-Co-Ni-MMOF with BDC linker promoted by K due to the augmenting surface basicity which leads to the increasing alkali-metal content, and shows exceptional performance in CO_2 hydrogenation via efficiency of CO_2 conversion of 47.5 % and selectivity of light olefins 46.8 % which is attributed to the



synergistic effect between Fe and other metal ions within the MOF-derived solid, boosting catalytic activity. Fe species can boost the binding force of Fe-O and Fe-C, enhancing the stability of reactive phases, and supporting the construction of Fe_5C_2 .¹⁰⁶ In another instance, bimetallic-derived FeMn-MOF was applied for non-radical oxidation of peroxydisulfate (PDS) and illustrated the performance of 96.5 % within 10 min for the degradation of sulfamethoxazole (SMX). $\text{Fe}_3\text{O}_4/\text{Mn}_3\text{O}_4$ interface, which can contain Fe-Mn bonds, could effectively boost PDS adsorption and electron-transport capacity.¹⁰⁷ Their high stability at pH = 2 is also due to the strong structural integrity and consistent redox cycling of Fe and Mn active sites anchored on biochar. This prevents metal leaching and maintains effective PDS activation. Furthermore, from DFT simulations, the adsorption energy of PDS on the $\text{Fe}_3\text{O}_4/\text{Mn}_3\text{O}_4$ with Fe–Mn connections is 2.0 eV, which is higher than the Fe/Mn–O bonding model (1.7 eV), indicating their better PDS activation.¹⁰⁷ In addition, the high valence (III) can also provide adequate stability to the framework structure for any application if there is an adequate Cr molar ratio, besides the expected synergistic effect derived from the combination with other metal ions such as Fe.⁷⁷ As one example, the catalytic activity of bimetallic MIL-101(Cr/Fe) (BTC as linker) for the Prins reaction between formaldehyde and β -pinene was studied and found to be higher than that of monometallic MIL-101(Cr). The enhanced catalytic activity is due to the complementary role of Cr^{3+} and Fe^{3+} ions, in a way that Cr^{3+} provides thermal and structural stability that is lacking for MIL-101(Fe), while the presence of Fe^{3+} ions into the MMOF results in an increase of the activity of the Lewis acid sites, therefore enhancing catalytic activity and stability.⁷⁷

Fe-MMOFs are widely used in photocatalysis, where charge transfer from Fe to other metals enhances the active site availability and improves photocatalytic charge separation efficiency.¹⁰⁸⁻¹¹¹ The multiple valence states of Fe facilitate strong interactions with donors like H_2O , optimizing photocatalytic reactions. This is the case of $\text{NH}_2\text{-MIL101(Fe, Co)}$, with an optimal Co/Fe ratio of 0.15, that can achieve a nitrogen photo-fixation efficiency of $335.7 \mu\text{mol g}^{-1} \text{ h}^{-1}$. The synergistic interaction between Co and Fe strengthens light harvesting, lowers the conduction band (CB) potential, and activates N_2 more effectively. Monometallic Fe-MOF has a strong PL peak at 460 nm, which can be related to the high electron-hole recombination rate. However, the PL intensities in bimetallic MOF samples are weaker than those of monometallic MOF, that related to the doping of Co, can suppress the recombination. Moreover, bimetallic MOF contains more oxygen vacancies that can be useful in the adsorption and activation of N_2 .¹⁰⁹ In



another instance, doping of Mn into MIL- 53(Fe) illustrates that the incorporation of Mn into the MOF can reduce the band gap and resulted in better removal of crystal violet (CV) with performance of 99.01% under a 100-W xenon lamp. In conclusion, for these materials in the photo-Fenton reaction, the Mn^{2+} can promote the generation of $\cdot OH$ radicals and Fe^{2+} . Furthermore, Fe^{2+} swiftly activates H_2O_2 and generates radicals in the case of CV degradation.¹¹²

From the above precedents, it can be concluded that Fe-MMOFs continue to be among the most researched MMOFs for a wide range of applications. In the case of biomedicine, Fe-MMOFs enhance drug delivery through increased pore size, higher cargo loading, and the immobilization of active sites. Fe-MMOFs have been widely used in electrochemical sensing, taking advantage of the various Fe oxidation states and the enzyme-like peroxidase/oxidase activity of these materials, combined with synergistic interactions with secondary metals. Regarding the pollutant removal and adsorption, the Lewis acidity and structural robustness make Fe-MMOF among the most suitable materials. However, among all the applications, Fe-MMOFs are mostly researched for their electrocatalytic activity with a focus on OER and novel, promising developments in UOR, HER, and other reactions. Also, the swing among Fe oxidation states and synergistic effects with other metals are very suited for this use, the enhanced activity deriving from high active site density and facile charge transfer, which results in low reducing overpotentials. Emerging applications of Fe-MMOFs in supercapacitors and batteries leverage Fe ability to undergo charge transfer processes and active site optimization. Regarding catalysis, Fe-MMOFs exhibit high TOF values and selectivity due to the Lewis acid behavior of Fe ions and electron density modulation through interaction with other transition metal ions. In photocatalysis, Fe-MMOFs often exhibit enhanced activity through more efficient light harvesting, efficient charge separation, availability of multiple oxidation states, and d-orbital electron dynamics by interaction with the other metals present in the MMOF material. Fe incorporation into MMOFs enhances their stability and functionality, enabling efficient removal of pollutants from aqueous and gaseous environments. In all these applications, the use of Fe-MMOF with Fe as the main metal has the advantage of cost-effectiveness due to its abundance and affordability, making Fe-MMOFs economically attractive for large-scale applications. In addition, the low toxicity allows their use in biomedical applications for drug delivery. Another general effect of the presence of Fe on the MMOF is the robustness of most of the materials due to the strong coordination bonds and the high Coulombic charge of Fe^{3+} , both factors contributing to the structural stability in various solvents and under thermal treatment.



Overall, Fe-MMOFs ability to combine with other metals opens avenues for a multitude of diverse applications. This review underscores the importance of Fe-MMOFs, particularly in sensing, medicinal, pollutant removal, and electrocatalysis applications, in which the intrinsic properties of Fe and synergy with other metals contribute to a superior performance of the resulting Fe-MMOF. The applications of Fe-MMOFs are summarized in **Table 1**, illustrating the intense research in this type of material. This positions Fe-MMOFs as crucial materials for advancing sustainable and high-performance technologies. Further, Table 1 provides an extensive comparison of Fe-MMOFs amid diverse applications for their performance. Although numerous Fe-MMOFs demonstrate their efficiency for energy applications due to their electro-active intrinsic nature, their performance toward removal applications can also be promising compared to other MMOFs. Table 1 presents various types of Fe-MMOFs and their corresponding metal contributions, as well as their applications and efficiencies, to inform future research. Their synergistic effect with Ni and Co is one of the most favorable engineering approaches for constructing electrocatalysts and photocatalysts. Also, their synergistic impact with Mn can be further developed, especially in energy storage and conversion systems. In the future, the Fe-MMOF cannot only be explored for less investigated applications, but also can be studied for optimizing the Fe content. Finding appropriate Fe content compared to other metals can especially affect their performance, notably in catalysis.

Table 1. Summary of the application of Fe-MMOFs or their derived composites or materials, indicating their efficiency.

Fe-MMOF	Other Metals	Application	Efficiency	Ref.
NiFeMo-MOF	Ni/Mo	Electrocatalyst/Water splitting	C.d: OER and HER: 50 Cell voltage: 10/ O.v: OER: 239 and HER:119/ T.f: OER: 87.0 and HER: 58.3/ C.v: 1.50	113
Fe ₂ O ₃ /ZnCo ₂ O ₄	Zn/Co	Electrocatalyst/Water splitting	C.d: OER and HER: 10 Cell voltage: 10/ O.v: OER: 212 and HER: 44.8/ T.f: OER: 41.2 and HER: 35.8/ C.v: 1.44	114
0.04Ru/FeCo-MOF	Ru/Co	Electrocatalyst/Water splitting	C.d: OER: 50 and HER: 10 Cell voltage: 10/ O.v: OER: 309 and HER: 180/ T.f: OER: 84.0 and HER: 146/ C.v: 1.498	115
Co ₄ Fe ₆ -MOF	Co	Electrocatalyst/OER	C.d: 10/ O.v: 241/ T.f: 30.1	100
NiFe-MOF	Ni	Electrocatalyst/OER	C.d: 100/ O.v: 277/ T.f: 73	116
Fe ₂ Ni ₁ - MOF-TDC	Ni	Electrocatalyst/OER	C.d: 10/ O.v: 211/ T.f: 40.3	117



Fe _{0.75} Ni _{0.25} S ₂	Ni	Electrocatalyst/OER	C.d: 10/ O.v: 247/ T.f: 47.6	118
FeCo _{0.5} Ni _{0.5} -LDH	Ni/Co	Electrocatalyst/OER	C.d: 10/ O.v: 258/ T.f: 38	119
CoNiFeO _x -NC	Ni/Co	Electrocatalyst/OER	C.d: 50/ O.v: 265/ T.f: 64.1	120
CoNiFeP-YSNSs	Ni/Co	Electrocatalyst/OER	C.d: 10/ O.v: 261/ T.f: 49.5	121
<u>FeCoNi@NC</u>	Ni/Co	Electrocatalyst/OER	C.d: 10/ O.v: 285/ T.f: 69.6	122
FeCoNi(OH) ₃ (BDC) _{1.5}	Ni/Co	Electrocatalyst/OER	C.d: 1000/ O.v: 284/ T.f: 29.5	123
MIL-59(FeNi)/Co NSs	Ni/Co	Electrocatalyst/OER	C.d: 20/ O.v: 216/ T.f: 38.46	59
M-NiA-CoN	Ni/Co	Electrocatalyst/OER	C.d: 10/ O.v: 180/ T.f: 41	102
FeCoNi-BHT	Ni/Co	Electrocatalyst/OER	C.d: 10/ O.v: 266/ T.f: 88	124
FeNi ₂ Co ₁ -MOF	Ni/Co	Electrocatalyst/OER	C.d: 10/ O.v: 143/ T.f: 68	125
30%CeNiFe-LDH	Ni/Ce	Electrocatalyst/OER	C.d: 10/ O.v: 242/ T.f: 34	101
PCN-Fe ₂ Co-Fe ₂ Ni	Ni/Co	Electrocatalyst/OER	C.d: 10/ O.v: 271/ T.f: 67.7	48
(FeNiCoCrCu) ₃ O ₄	Ni/Co/Cr/Cu	Electrocatalyst/OER	C.d: 10/ O.v: 270/ T.f: 49	66
(FeNiCoCrCu) ₃ O ₄	Ni/Co/Cr/Cu	Electrocatalyst/UOR	C.d: 10/ O.p: 1.35/ T.f: 33	66
FLaN-MOF	La	Battery/LIBs	C.d: 100/ capacity: 337/ cycle: 100	126
Fe-Mn-O/C	Mn	Battery/LIBs	C.d: 100/ capacity: 1294/ cycle: 200	127
Fe-Fe_{0.33}Mn_{0.67}O/C	Mn	Battery/ LIBs	C.d: 1000/ capacity: 626.8/ cycle: 1000	128
NiFe/Mn-MOF	Ni/Mn	Supercapacitor	S.p: 1640/ C.d: 1.0 (5000 cycle)/ E.d: 75/ P.d: 1166/ retention: 94%	129
CoFe ₂ -MOF	Co	Supercapacitor	S.p: 112.1/ C.d: 1.0 (12000 cycle)/ E.d: 56.2/ P.d: 1091.5/ retention: 97.91%	53
NH ₂ -MIL-88B (Fe _{0.6} In _{0.4})	In	Photocatalyst/Cr(VI) reduction	86.83%/ Bandgap: 2.58	130
NM-Fe-0.15Co	Co	Photocatalyst/N ₂ reduction	NH ₃ evolution rate: 335.7 $\mu\text{mol g}^{-1} \text{h}^{-1}$	109
10%Ni/Fe-MOF	Ni	Photocatalyst/Dye degradation	96%/ Bandgap: 2.55/ R ² : 0.98683/ reuse: 5 cycles	131
Fe/Ni-T120	Ni	Photocatalyst/CO ₂ reduction	CO evolution rate: 9.74/ CO selectivity: 92.1%/ Bandgap: 1.69/ AQE: 0.057%	132
Fe-Cu-T130	Cu	Photocatalyst/CO ₂ reduction	CH ₄ generation rate: 499.2/ Bandgap: 1.51/ AQE: 0.0011%/ reuse: 5 cycles	133
Fe _{0.02} Ni _{0.10} -Co _{0.15} -PCN-250	Ni/Co	Photocatalyst/ CO ₂ reduction	CO yield: 299/ Bandgap: 1.92	134
Fe ₂ Zn-MOF	Zn	Catalyst/ imine synthesis	97%/ 80 °C/ air/ 12 h/ reuse: 5 cycles	135
MIL-101(Al/Fe)-NH₂(15:1)	Al	Catalyst/ Knoevenagel condensation reaction	100%/ 90°C/ BDA/ 90min/ reuse: 5 cycles	136
Co/Fe-MOF	Co	Catalyst/ Synthesis of N-Pyridinylamides	94%/ DTBP/ 120 °C/24 h/ reuse: 5 cycles	137
MIL-101(Cr/Fe)	Cr	Catalyst/ Prins reaction	63.75% (for Nopol)/ selectivity: 80%/ reuse: 4 cycles	77
FCN-K(a)	Ni/Co	Catalyst/ CO ₂ hydrogenation	47.5%/ 320 °C/ selectivity: 46.8%	106
MOF-(Al, 5Cr, 3Fe)	Al/Cr	Catalyst/ Aromatization of p-xylene	21%/ 450°C/ selectivity: 91%/ reuse: 3 cycles	138



Fe Pt Rh MOF	Pt/Rh	Sensing/ Detection of heart-type fatty acid binding protein	LOD of 0.01–100 ng mL ⁻¹	139
S-FCM-MOF@PCL	Co/Mn	Sensing/ Detection of bisphenol A and S	LODs (2.57, 2.91 μM)	140
Fe/4Cu-MOF	Cu	Sensing/ Selective colorimetric detection of <i>Salmonella typhimurium</i> in food	LOD of 1.0×10^2 CFU/mL	141
Fe/Ni-MOFs	Ni	Sensing/ Detection of thiamphenicol	LOD: 0.030 and 0.031 nM	142
Fe ₂ Ni MIL-88B	Ni	Sensing/ Selective detection of dopamine	LOD of 0.40 μM (S/N = 3) and higher sensitivity of 124.7 μA mM ⁻¹ cm ⁻²	143
Fe/Co-MOF	Co	Removal/ Toxic metals	-	144
Fe–Mg MOF	Mg	Removal/ Heavy metal	-	145
FeCu-MOFs	Cu	Removal/ Adsorbents for gaseous elemental Hg removal	equilibrium adsorption: 12.27 mg/g	146
UiO-66(Fe/Zr)	Zr	Removal/ Removal and immobilization of Se	adsorption capacity for Se(IV) and Se(VI): 196 mg/g at pH =3 and 258 mg/g at pH =5	147
Ag-Fe MOF	Ag	Removal/Cd and Cu removal	Cd(II) and Cu(II) adsorption: 265 and 213 mg/g	148
Mn–Fe MOFs	Mn	Removal/ Reductive removal of Cr(VI)	initial Cr(VI) concentration: 20 mg L ⁻¹ , and 10 mg of photocatalyst within 30 min.	149
PCN-250(Fe ₂ Ni)	Ni	Adsorption and Separation/ SO ₂	SO ₂ uptake: 8.64 mmol g ⁻¹ at 0.1 bar and 298 K	150
FeNi _x -BDC	Ni	Adsorption and Separation/ organic dyes	-	151
Cu/Fe-BTC	Cu	Adsorption and Separation/ U (VI)	optimum pH: 7.0 adsorption capacity: 354 mg·g ⁻¹	152

C.d: current density given in A g⁻¹ or mA cm⁻² for energy applications; O.v: overpotential given in mV; T.f: Tafel slope given in mV dec⁻¹; C.v: cell voltage given in V; O.p: onset potential given in V in the most research capacity and S.p (specific capacitance) is given in F/g, C/g, and mAh g⁻¹; E.d: energy density given in Wh kg⁻¹; P.d: power density given in W kg⁻¹; all percentage in photocatalyst or catalyst represent yield, conversion or any efficiency of MMOFs which for further details can see the references; bandgap given in eV; AQE: apparent quantum efficiency; p.d: photocurrent density given in μA cm⁻²; RT: room temperature; E_a: Energy activation given in kJ mol⁻¹; for further details can see the references. YNSNs: yolk-shell nanospindle; NC: N-doped carbon; NS: nanoasheets; BHT: benzenehexathiol; PCN: porous coordination network; FLaN : FeLaNa; NM: NH₂-MIL-101; Fe/Ni-T120 and Fe–Cu-T130: mixed metal MOFs prepared using dihydroxyterephthalic acid by solvothermal synthesis at the indicated temperature; FCN-K(a): FeCoNi MOF-derived carbon material incorporating K after calcination; PCL: polycaprolactone coated.

5. Nickel-based MMOFs



Nickel-based MOFs (Ni-MMOFs) have gained significant attention due to their remarkable properties, low cost, environmental compatibility, and corrosion resistance in alkaline environments. Very frequently, Ni-MMOFs also enjoy sufficient thermal and chemical stability. These characteristics, combined with a high specific charge capacity, make Ni-MMOFs as versatile materials for applications in energy storage, catalysis, medicine, and sensing. Ni-MMOFs enhance their performance in these applications by incorporating additional metals, resulting in a general effect in improved electrical conductivity, stability, and catalytic performance.^{153, 154}

Ni-MMOFs exhibit excellent stability and electrocatalytic performance in alkaline electrolytes, making them suitable for electrochemical sensors under certain conditions. Incorporating additional metals into Ni-MOFs enhances conductivity, active site density, and overall catalytic efficiency. In one example, NiCo-BTC/CC, a bimetallic MOF (BTC: 1,3,5-benzenetricarboxylate, as linker) on carbon cloth (CC), significantly improves glucose sensing due to the presence of cobalt with the enhanced oxygen adsorption and charge redistribution between Ni and Co ions. Synergistic impact amid Ni and Co augments the activity and stabilizes the MOF architecture, which leads to premier sensitivity and stability compared to monometallic MOF counterparts. The bimetallic MOF exhibits the sensitivity of $2701.29 \mu\text{A mM}^{-1} \text{cm}^{-2}$ with low detection limit of $0.09 \mu\text{M}$.¹⁵⁵

Ni-MMOFs are highly effective for removing heavy metals in aqueous media due to their large surface areas, enhanced pore sizes, and augmented negative charge layers. This is the case of the 2D Ni/Cd-MOF sheets (BDC as linker) that outperform monometallic Ni-MOF in Pb^{2+} removal due to increased electrostatic repulsion between the 2D MOF sheets, minimizing their stacking and improving the adsorption capacity. The bimetallic MOF exhibits a larger surface area and pore size, facilitating efficient contaminant removal. Stability at various pH illustrated that the bimetallic MOF is well maintained as evidenced from XRD results, but slightly collapses at pH 2. However, Ni-MOF and Ni/Cd-MOF in strong alkaline solutions led to the dissolution of 2D MOFs. Furthermore, bimetallic MOFs contain more crystal defects and vacancies. Thus, compared to monometallic Ni-MOF, bimetallic Ni/Cd-MOF shows a higher specific surface area and higher surface electronegativity, which leads to effective, rapid diffusion of Pb^{2+} to its active sites.¹⁵⁶

In the pharmaceutical field and health monitoring, Ni-MMOFs demonstrate potential usage for antibacterial and wound-healing, and piezoresistive sensor applications.^{157, 158} As an example,



NiCoCu-based MOF nanosheets (BDC as linker) exhibit peroxide-like activity, catalyzing H_2O_2 to $\cdot\text{OH}$ radicals. This enhances antibacterial performance against methicillin-resistant *Staphylococcus aureus* and gram-positive *Escherichia coli*. Copper incorporation accelerates wound healing due to the combination of 2D NiCoCu-MMOF, which have good stability in DMF solution and absolute ethanol, and H_2O_2 by facilitating electron transfer and stabilizing nanoenzymes, which results in preventing inflammation and accelerating skin growth. These results make NiCoCu-MMOF a promising candidate for therapeutic applications. The addition of Cu^{2+} as cofactors enhances the high POD-like activity, and Ni, Co can decrease the path of electron transport and ion diffusion.¹⁵⁷

Ni-MMOFs and their derived forms have been extensively studied as electrocatalysts in OER, HER, and UOR applications.¹⁵⁹⁻¹⁶⁴ Incorporating metals such as Fe, Co, and Cu further enhances electron transfer, reduces overpotential, and increases active sites. In OER, Ni-MMOFs benefit from the synergistic effects of multiple metals, which enhance electrical conductivity and optimize intermediate adsorption. In one example, Ni–BDC MOFs incorporating Er showed improved OER and HER activity. $\text{Er}_{0.5}\text{Ni–BDC}$ MOF exhibits an overpotential of 420 mV for OER, while ErNi–BDC MOF achieves an overpotential of 270 mV for HER, demonstrating the impact of Er in enhancing active sites and improving electrocatalytic efficiency.¹⁶⁵ In another example, $\text{NiFe}_{0.2}\text{Co}_{0.3}\text{-ZIF}$ trimetallic MOF (2-methylimidazole as linker) exhibits even a lower overpotential of 216 mV and a Tafel slope of 23.25 mV dec^{-1} at 100 mA cm^{-2} . The synergistic interaction among Fe, Co, and Ni reduces the energy barrier and increases active sites, boosting OER performance. Also, the higher intrinsic activity in OER for $\text{NiFe}_{0.2}\text{Co}_{0.3}\text{-ZIF}$ was evidenced by achieving a TOF of 0.0259 s^{-1} compared to Ni-ZIF and $\text{NiFe}_{0.2}\text{-ZIF}$ solids, which both of them are below than 0.01 s^{-1} .¹⁶⁶ In another instance, bimetallic $\text{NiFe}\text{-MOF-}\text{BF}_4^-$ -0.3 NSs exhibit a low overpotential of 237 mV at a current density of 10 mA cm^{-2} with a Tafel slope of 41 mV dec^{-1} in alkaline media. Based on XPS analysis, electron transport from Ni or Fe to F in the counterion leads to better charge transfer and alters the coordination environment of metals, therefore accelerating OER kinetics in the electrochemical procedure and enhancing OER activity. Figure 9 illustrates the theoretical calculations where the introduction of Fe to the monometallic Ni-based MOF leads to a conduction band closer to the Fermi level. During synthesis, Fe^{2+} ions are converted to Fe^{3+} ions and exchange with some of the Ni^{2+} ions. Furthermore, the introduction of counterion also augments electron number close to the Fermi level which both Fe and counterions



favor to a new electronic state which is evidenced by better conductivity and activity of the synthesized MOF. Also, achieving lower energy shifts for bimetallic counterion MOF in comparison to monometallic and bimetallic MOF can buttress OER activity by regulating OH^* , O^* , and OOH^* adsorption in an electrochemical procedure. Higher charge density and lower energy barrier are also important factors for better OER activity of NiFe-MOF- BF_4^- -0.3 NSs.¹⁶⁷

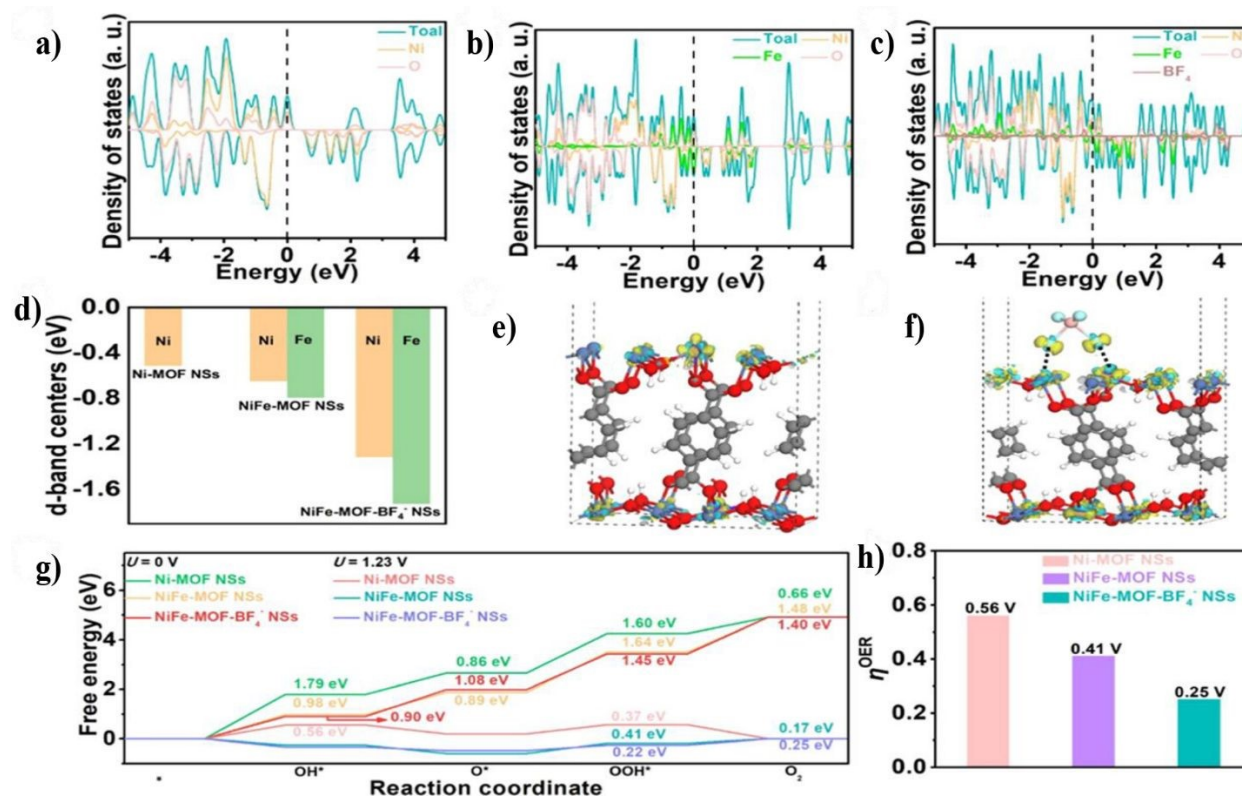


Figure 9. DOS of a) Ni-MOF NSs; b) NiFe-MOF NSs; c) NiFe-MOF- BF_4^- NSs; d) d-band center of Ni in Ni-MOF NSs, Ni and Fe in NiFe-MOF NSs, and NiFe-MOF- BF_4^- NSs; and the density difference of e) NiFe-MOF NSs and f) NiFe-MOF- BF_4^- NSs with an isosurface value of 0.003 eV/Å³. Yellow and cyan regions represent charge depletion and accumulation, respectively; g) calculated free energy for OER with Ni-MOF NS, NiFe-MOF NS, and NiFe-MOF- BF_4^- NS surface at 0 and 1.23 V; and h) η_{OER} comparison of Ni-MOF NSs, NiFeMOF NSs, NiFe-MOF- BF_4^- NSs. Reproduced with permission from ref.¹⁶⁷ Copyright 2022 American Chemical Society.

In another example, $\text{Ni}_{0.5}\text{Fe}_{0.5}\text{-THQ}$ exhibits better OER activity in comparison with Ni-THQ, $\text{Ni}_{0.8}\text{Fe}_{0.2}\text{-THQ}$, $\text{Ni}_{0.5}\text{Fe}_{0.5}\text{-THQ}$, $\text{Ni}_{0.2}\text{Fe}_{0.8}\text{-THQ}$, and Fe-THQ via higher C_{dl} efficiency of 0.852 mF cm⁻², larger ECSA of 21.25 cm², higher mass activity of 175 mA mg⁻¹ which is pertinent to the intrinsic activity of MOF, and higher TOF of 0.026 s⁻¹, as well as other counterparts

performance exhibited in Figure 10. The adsorption energies of OH^- species on iron sites is -0.54 eV in $\text{Ni}_{0.5}\text{Fe}_{0.5}\text{-THQ}$, which is lower than adjacent nickel sites that are -0.05 eV, resulting in the Fe sites acting as active metal centers for the OER. Also, the synergistic impact between Fe and Ni in bimetallic MOF can reinforce the OER activity by decreasing the energy barrier of the intermediate product. In addition, the highest d-band center of Fe sites in bimetallic MOF illustrates strong adsorption capacity for species, which leads us to higher OER activity due to the transporting d-electron of the Ni site to the Fe site via d- π conjugation on the surface of the bimetallic MOF.¹⁶⁸

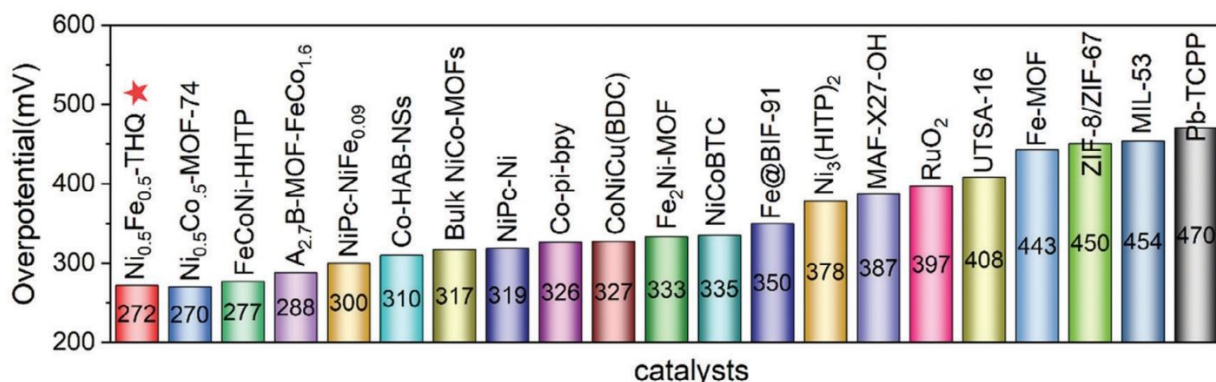


Figure 10. Comparison of the performance of $\text{Ni}_{0.5}\text{Fe}_{0.5}\text{-THQ}$ with other MOFs and commercial RuO_2 for OER applications. Reproduced with permission from ref.¹⁶⁸ Copyright 2024 Wiley.

In another pertinent example, NiCoFe-NDA (NDA: 1,6-naphthalenedicarboxylic acid) grown on NF showed a lower overpotential of 215 mV and a lower Tafel slope of 64 mV dec^{-1} at a current density of 10 mA cm^{-2} and higher C_{dl} compared to the monometallic Ni-NDA/NF, Co-NDA/NF, and Fe-NDA/NF and commercial IrO_2 . In addition, NiCoFe-NDA exhibited an enhanced stability (current density of 100 mA cm^{-2} via 6% decay after 50 h) as shown in Figure 11. Better function in the OER application is related to the i) lower coordination environment for NiCoFe-NDA (4-coordinated) via applying Fe. also, $\text{Fe}^{2+/\text{3}+}$ can decrease overpotential by optimizing rate-determining steps, leading to better OER activity, which is provided by theoretical methods. ii) synergistic effect between metal ions and the formation of metal oxyhydroxides, which is beneficial for OER application.¹⁶⁹

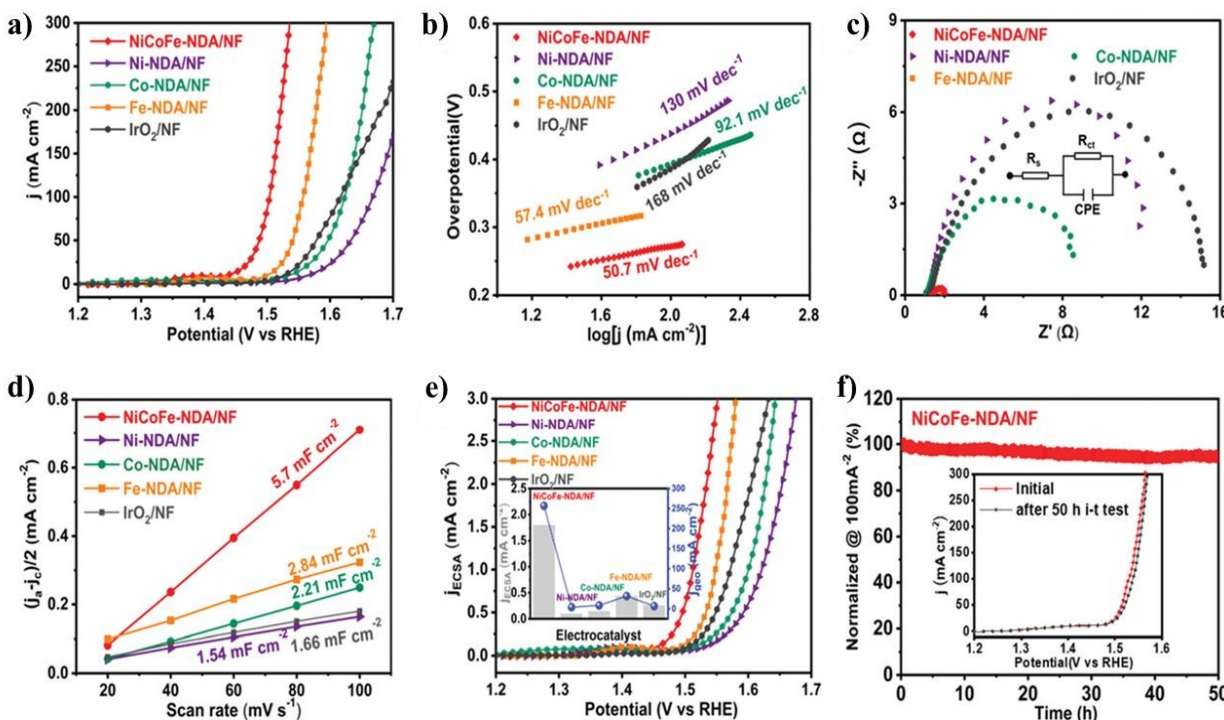


Figure 11. Evaluating OER activity of NiCoFe-NDA/NF in terms of a) LSV curves, b) Tafel slope, c) Nyquist plots, d) C_{dl} , e) ECSA-normalized LSV curve, and f) chronoamperometric curves. Reproduced with permission from ref.¹⁶⁹ Copyright 2021 Royal Society of Chemistry.

High entropy MOFs have recently been explored due to their diverse synergistic effect between metals for electrocatalysis.¹⁷⁰ For instance, penta-metallic high entropy MOF composed of Ni, Co, Zn, Fe, and Mo, metals (HE-MOF) exhibits an overpotential of 254 mV at a current density of 50 mA cm⁻². High-entropy materials can minimize Gibbs-free energy but have flaws in the OER process due to the harsh conditions of synthesis. They produce bulk forms in which adjacent nanoparticles of bulk high-entropy materials can overcome this demerit. Furthermore, the synthesis of ultrathin HE-MOF due to the rich active sites, synergic between metal ions, and high entropy can lead us to better OER activity compared to other counterparts have shown in Figure 12.¹⁷¹ Compared to other multi-metallic MOFs, Ni-MMOFs have been less explored as heterogeneous catalysts, primarily because other metal ions often exhibit superior catalytic activity. Nevertheless, the incorporation of Ni alongside other metals can enhance catalytic performance by creating open metal sites, and oxygen vacancies, and by reaction intermediate stabilization. These features make Ni-MMOFs valuable for applications such as dehydrogenation and hydrodeoxygenation. One of the recent examples of Ni-MMOFs as an electrocatalyst is the



use of NiFe-GA (GA: gallate) bimetallic MOF for OER, showing a superior activity with overpotentials of 185 mV and 236 mV for 10 mA cm⁻² and 100 mA cm⁻² in 1.0 M KOH, respectively. This performance was attributed to the hexagonal structure of NiFe-GA, ample active sites, and strong d-p orbital overlaps between Ni, Fe, and oxygen, reducing activation barriers and enhancing catalytic efficiency.¹⁷²

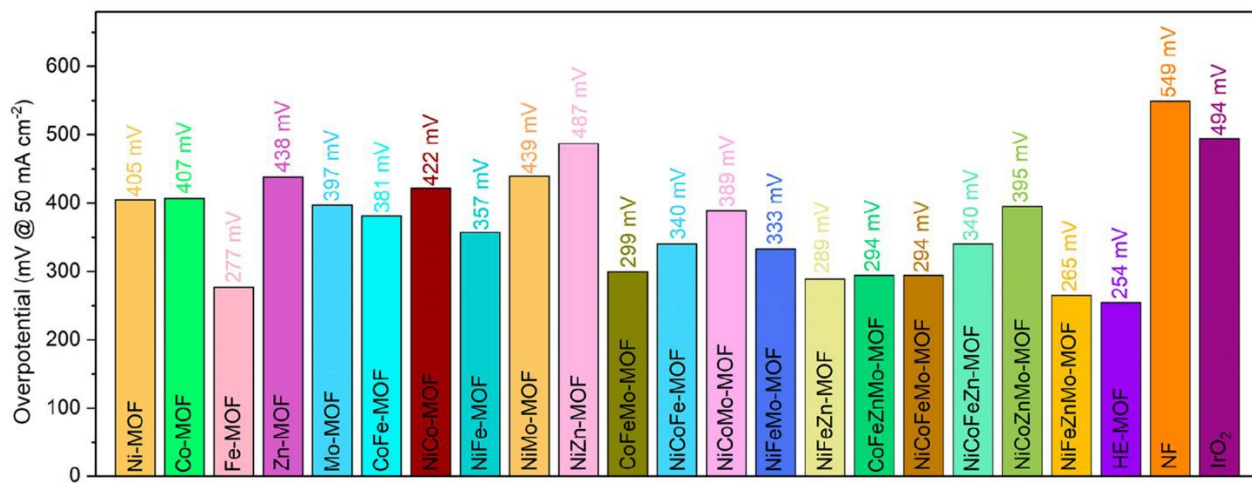


Figure 12. Comparison of the overpotential of HE-MOF with other mono-, bi-, tri-, tetra-metallic MOFs, bare NF, and commercial IrO₂ solids. Reproduced with permission from ref.¹⁷¹ Copyright 2022 American Chemical Society.

Similarly to OER, the HER activity in Ni-MMOFs can also improve significantly upon the introduction of metals that shift the d-band center to lower energy levels. This is the case of NiRu_{0.13}-BDC, a bimetallic MOF, that achieves remarkable HER activity with a remarkably low overpotential of 36 mV at 10 mA cm⁻². Ruthenium incorporation enhances electron interactions and modifies Ni electronic structure, optimizing intermediate adsorption and facilitating H₂ release.¹⁷³ Regarding UOR, Ni-MMOFs facilitate urea oxidation by generating highly oxidizing Ni³⁺ species that enhance electron withdrawal and boost catalytic activity. In one of the reports on multi-metallic Ni MOFs, Fc-NiCo-BDC (Fc denoted as ferrocene carboxylic acid) demonstrates superior UOR and OER activity due to ferrocene electronegativity, which enhances active site accessibility and reduces the bandgap of NiCo-BDC, improving electrical conductivity.¹⁷⁴ Control of the electronic density of Ni and Co by Fc plays a crucial role in adjusting the adsorption of reaction intermediates, which is important to achieving high turnover frequencies. In this way, NiMg-MOF-74-derived Ni–N–C catalyst having single Ni atoms demonstrates a Faradaic



efficiency of 90% in CO_2 reduction towards CO, highlighting its potential for energy storage applications.⁶⁵ In this case, the role of Mg was to dilute Ni in the MOF structure that upon transformation into the N-doped carbonaceous material, becomes isolated as single atoms, rather than forming Ni nanoparticles. Ni metal assignment in MMOFs is fully investigated toward electrocatalysts. Reports demonstrate that Ni is one of the most vital metals for electrocatalysts in MMOFs. Due to the electroactive nature of Ni, this metal can be a pivotal candidate for electrocatalytic activity by reducing the overpotential and energy barrier of RDS. Approximately, most of the Ni incorporation is pertinent to the mixed Ni-FeMOFs, whose synergistic effect demonstrates higher electrocatalytic activity due to the lowering of overpotential by Fe and increased conductivity by Ni. Furthermore, when Ni is adjacent to the Fe and Co can be considered to be a potential candidate for electrocatalysts for MMOFs engineering. For example, $\text{Ni}_5\text{In}_3\text{-Fc/NF}$ MOF, due to the synergistic effect among Ni/In, can optimize the electronic structure and the adsorption of intermediates, including *COOH and *CO, which lead to better CH_4 production via Faradaic efficiency of 76% and superior structural stability during a 16000-second period. The incorporation of FcDA^{2-} (ferrocene-1,1'dicarboxylate) with π -conjugation and reversible redox features, can support the electron conductivity and prompt catalytic selectivity. Based on DFT simulations, the *CO intermediate formation illustrated that Ni/In dual sites have a high energy barrier, validating its role as the rate-determining step for total reaction kinetics. Also, the Ni-only configuration illustrated that the lowest energy barrier for * CH_4 desorption, which leads to the rich active sites and buffers subsequent reactions.¹⁷⁵

Ni-MMOFs have demonstrated exceptional potential for energy storage applications, including batteries and supercapacitors, owing to their ability to enhance charge transport, increase specific capacitance, and generate abundant active sites.^{70, 176, 177} In one of the studies in this area, a bimetallic Ni, Co MOF of 1,3,5-benzenetricarboxylic acid with an optimal 15 %v Co submitted to *in situ* etching exhibits a specific capacity of 108.5 mAh g^{-1} at 0.5 A g^{-1} , with 84.3% retention over 6,500 cycles reported. Its unique morphology, comprising aggregated nanowires, offers abundant active sites that facilitate charge transport and accelerate redox reactions through synergistic interactions.⁷⁰ In another study, a bimetallic NiMn sulfide derived from the corresponding bimetallic MOF-74 having 2,5-dihydroxybenzene-1,4-dicarboxylic acid as linker was transformed into the corresponding sulfide derivative by sulphuration of the mixed NiMn oxide resulting from the calcination at 450°C under air of the MOF. The NiMnS exhibits a specific



capacitance of 2510.15 F g^{-1} at 1 A g^{-1} and 84.5% retention after 5,000 cycles. The reason for this excellent performance is the mesoporous structures that increase surface area and pore size, enhancing ion transfer rates and facilitating electrolyte access. XPS data confirms the presence of Ni^{2+} and Mn^{2+} , which bolster conductivity and introduce redox activity for charge storage.¹⁷⁸ In a trimetallic phosphide supported on carbon derived from NiCoZn-MMOF-74, it was found that segregated ZnO plays the role of preserving the porous structure inherited from the MOF, while Ni and Co undergo phosphidization to form mixed NiCoP nanoparticles in close combination with ZnO. The material stores electrical energy by a mixed mechanism combining double-layer capacitance and faradaic charge storage, reaching energy densities from $44.6\text{ W}\cdot\text{h}\cdot\text{Kg}^{-1}$ at $1500\text{ W}\cdot\text{Kg}^{-1}$ using a liquid electrolyte, and $35.4\text{ W}\cdot\text{h}\cdot\text{Kg}^{-1}$ at $1500\text{ W}\cdot\text{Kg}^{-1}$ with a quasi-solid-state electrolyte. The energy storage capacity was maintained over 90 % of the value of the fresh material after 5000 charge-discharge cycles. This NiCoZnP/C material illustrates the synergistic effects that can be derived from different roles played by the various metals.¹⁷⁶ The redox potential available to Ni ions makes Ni-MMOFs among the most widely used materials for energy storage systems. Several conclusions can be drawn from the analysis of these reports, including:

i) Prevalence of Ni metal: Ni-MMOFs account for 31.25% of total energy storage systems, highlighting the significance of this element in this field; **ii)** Ni-CoMOFs correspond to approximately 75% of the Ni-MMOFs used in electrical energy storage systems implying the synergistic interactions between Ni and Co, attributed to their appropriate redox potentials that allow reaching high specific capacitance, and **iii)** the multiple Mn oxidation states complement Ni, resulting in enhanced charge transport and energy storage efficiency for NiMn-MMOFs. The key features provided by Ni metal in Ni-MMOFs applied to energy storage are: **i)** mixed $\text{Ni}^{2+}/\text{Ni}^{3+}$ valence states occurring at high potentials, enhancing electron availability, supporting higher specific capacitance; **ii)** occurrence of synergistic effects with other metals, such as the previously commented Ni-Co, Ni-Mn pairs, improving conductivity, redox charge storage, and ion transfer rates; **iii)** possibility to synthesize materials with unique morphologies, such as nanowires and mesoporous frameworks providing high surface area and exposure of abundant active sites for electrolyte interaction, and **iv)** durability exhibiting a high energy retention percentage over multiple cycles ensure long-term stability. Table 2 offers additional examples of Ni-MMOFs in energy storage, showcasing their versatility and potential for advancing next-generation battery and supercapacitor technologies.



Regarding thermal catalysis, a Ni-MMOF derivative containing a Ce/Ni atomic ratio of 1/3 was obtained by calcination at 500 °C under the N₂ flow of NiCeMOF with trimesic acid as a linker. The resulting derivative consists of rod-shaped mesoporous CeO₂ with high oxygen vacancy density supported on carbonaceous residue containing Ni nanoparticles. Ni-CeO₂/C demonstrates outstanding catalytic activity for hydrodeoxygenation of lignin model molecules, like vanillin, achieving a >95% conversion rate and 81.4% selectivity to 2-methoxy-4-methylphenol with four-cycle reusability. This performance is attributed to the synergistic effect of Ce and Ni, which increases oxygen vacancy density on the CeO₂, facilitating vanillin conversion.⁷⁹ Ni-MMOFs exhibit significant potential in photocatalysis and removal of dyes due to their synergistic effects between Ni and other metal ions.^{80,179} These effects diminish the energy band gap, which increases light harvesting and improves the regulation of energy barriers and Gibbs-free energy. Ni high affinity for π^* orbitals, enabled by its d⁸ electron configuration, makes it particularly effective for photocatalytic CO₂ reduction and hydrogen evolution. Ni-MMOFs excel in CO₂ photoreduction due to their ability to stabilize intermediates and to lower energy barriers when combined with other metals. In one report, Ni_{0.75}Mg_{0.25}-MOF-74 was found to achieve a yield of 0.64 mmol h⁻¹ g_{MOF}⁻¹ of HCOO⁻ in pure CO₂, much higher than the yield of Ni-MOF-74 as photocatalyst (0.29 mmol h⁻¹ g_{MOF}⁻¹). Mg-MOF-74 was, on the other hand, inactive as a photocatalyst. It was proposed that the activity of Ni_{0.75}Mg_{0.25}-MOF-74 arises from the strong CO₂ affinity of Mg and the synergistic interaction between Mg²⁺ and Ni²⁺, stabilizing the *OCOH intermediate, decreasing the energy barrier and enhancing efficiency.⁴⁶ In another example, NiZrCu-BDC, a two-dimensional trimetallic MOF, reduces CO₂ to methanol and ethanol with efficiencies of 41.05 μ mol h⁻¹ g⁻¹ and 36.62 μ mol h⁻¹ g⁻¹, respectively. The ultrathin structure (4 nm) diminishes the distance required by the charge carriers to reach the surface, while Zr and Cu promote CO₂ chemisorption and intermediate stabilization.¹⁶ Ni-MMOFs are efficient materials to promote HER. Their performance can be further optimized by regulating the free energy values of hydrogen adsorption (ΔG_{H^*}) which is a suitable descriptor to predict the proton reduction efficiency. Incorporating additional metals, like Pt, can increase Ni intrinsic HER catalytic activity. In one illustrative example, a bimetallic 2D HTHATN-Ni-Pt-NS MOF (HTHATN: hexathiohexaazatrinaphthylene; NS: nanosheets) was used as a hydrogen evolution co-catalyst and quencher of ruthenium(II) trisbipyridyl photosensitizer. Upon irradiation with visible light ($\lambda > 420$ nm) using ruthenium(II) polypyridyl complex as light harvesting and in the



presence of N,N-dimethylaniline as sacrificial electron donor, HTHATN-Ni-Pt-NS achieves a H_2 evolution rate of $47.2 \text{ mmol g}^{-1} \text{ h}^{-1}$, significantly outperforming the monometallic counterpart and becoming among the most efficient HER materials in photocatalysis. Pt^{2+} ions create active metal centers and optimize the ΔG_{H^*} value of Ni^{2+} sites, facilitating efficient proton reduction and H_2 desorption. The π -conjugated system of the MOF supports electron transfer, further enhancing activity.⁸² Ni-MMOFs-derived materials show exceptional photocatalytic efficiency for simultaneous overall H_2 and O_2 production. As an example, $\text{Fe}_1\text{-Ni}_2\text{-P}$ phosphide nanotubes derived from Fe-Ni/MIL-88 by phosphatization with in situ generated PH_3 exhibit H_2 production of $5420 \text{ } \mu\text{mol g}^{-1} \text{ h}^{-1}$ and O_2 production of $900.3 \text{ } \mu\text{mol g}^{-1} \text{ h}^{-1}$. The phosphatization process improves kinetics and enhances the photocatalytic activity compared to monometallic Fe_2P or Ni_2P ⁸⁰ (Figure 13). In another instance, derived-FeNi MOFs illustrate the degradation efficiency of 91% for rhodamine B (RhB) and 89% for Congo red, which is superior compared to the conventionally prepared FeNi-MOFs. Based on the DFT simulation, Ni and Fe form clusters that are arranged in proximity to each other and, through proper interaction, modulate the electronic and catalytic features of MOF. Fe/Ni sites decrease the strength of dye molecule bonds and reinforce the degradation procedure; meanwhile, carboxyl groups in bimetallic MOF can provide a potent hydrogen bond and stability.¹⁸⁰

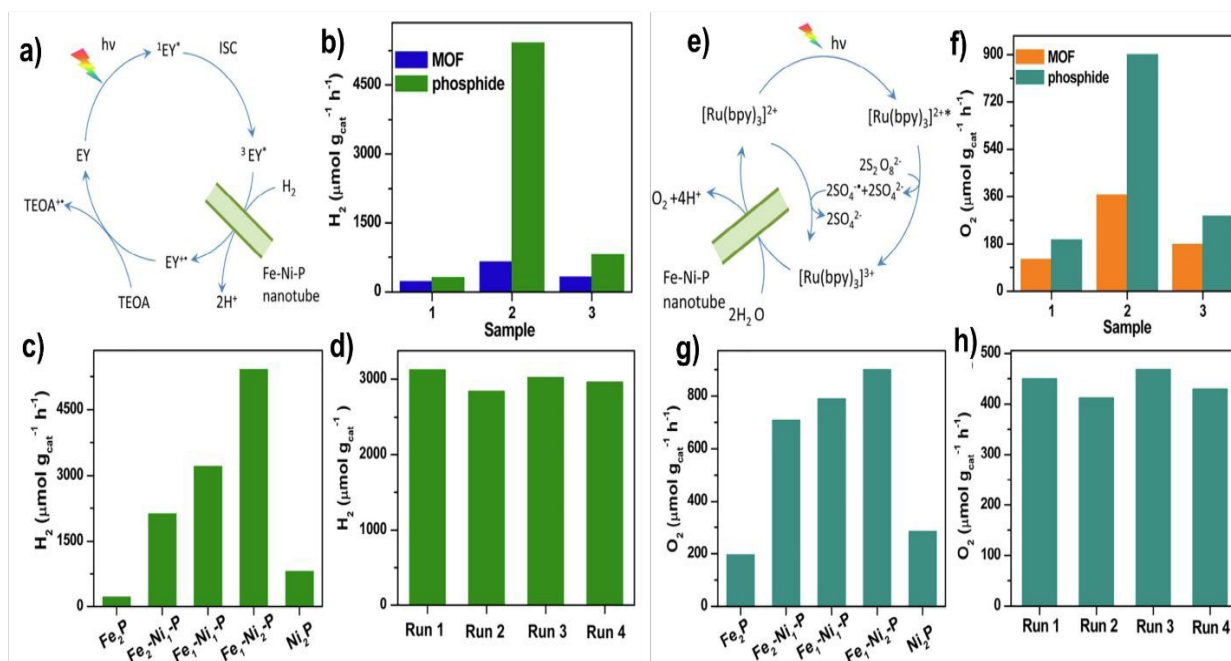


Figure 13. a) Proposed mechanism for the Eosin-Y photosensitized H_2 evolution promoted by MOF-derived bimetallic Fe-Ni-P; b) H_2 production rates of Fe_2P (1), Fe_1-Ni_2-P (2), and Ni_2P (3) and their MOF precursors, c) H_2 production rates of diverse MOF derived phosphides; d) Stability of Fe_1-Ni_2-P nanotubes in the Eosin-Y photosensitized H_2 evolution; e) Proposed mechanism for the O_2 evolution promoted by MOF derived Fe-Ni-P using $Ru(bpy)_3^{2+}$ -photosensitization; f) O_2 production rates of Fe_2P (1), Fe_1-Ni_2-P (2), and Ni_2P (3) and their MOF precursors; g) O_2 production rates of diverse MOF derived phosphides; h) Stability of Fe_1-Ni_2-P nanotubes in the O_2 evolution rates using $Ru(bpy)_3^{2+}$ -photosensitization. Reproduced with permission from ref.⁸⁰ Copyright 2020 Elsevier.

The incorporation of other metal ions creates synergistic effects, improving both performance and durability. Additionally, the mixed valence states of nickel (Ni^{2+}/Ni^{3+}) contribute to the increased electron availability, further enhancing energy storage capabilities. For batteries applications, Ni-MMOFs outperform Ni-MOFs due to the interaction of Ni possessing strong Lewis acid character with anions and other metals. These interactions enable effective electrolyte penetration and ion migration, such as Li^+ ions, through the MOF porous structure. The synergistic effects between Ni and other metals enhance the conductivity, stability, and overall performance of battery systems. Table 2 provides additional examples of Ni-MMOFs in battery systems. For energy storage applications based on Ni-MMOFs, Ni sites via a synergistic effect with adjacent metals can generate more active sites by enhancing charge transport and altering the structure to achieve better performance of energy storage. Also, mixed valence $Ni^{2+/3+}$ alongside other metal ions can generate more electrons during storage applications and increase specific capacitance. Strong Lewis acid/base interactions between Ni and anions, modulated by other metals in Ni-MMOFs can improve the performance of battery applications via synergistic effect due to the effective penetration of the electrolyte and facile migration of ions through the micropores, particularly Li^+ , which is highly relevant in batteries. In total, Ni metal into MMOFs illustrates as one of the most used metals in energy storage systems, which show their significance toward this application. Also, the synergistic effect between Co and Mn is interesting for many researchers. Ni and its synergistic with Co (Ni-CoMOFs) demonstrate higher performance due to rich redox activity and an augmentation in the specific capacitance. Also, Mn and its synergistic effect with Ni exhibit great energy storage performance due to the multi-valent nature of Mn. Besides batteries, Ni-MMOFs are also highly efficient materials for storing electrical energy in supercapacitors due to the high specific capacitance values that Ni-MMOFs can achieve and their



durability over extended charge-discharge cycles. The combination of Ni with metals like Co and Mn enhances the redox activity of the resulting MMOF, accelerating Faraday redox reactions and providing additional active sites for electrolyte interaction. In this way, materials exhibiting pseudo capacitance that combine double-layer charge storage of supercapacitors with reversible redox processes characteristic of batteries can be obtained. Furthermore, Ni can lower the energy barrier of gas formation and evolution, and it has more affinity for π^* orbitals due to the large number of d orbital electrons (d⁸), which is beneficial for reactions requiring CO₂ activation. Furthermore, their synergistic effect with Fe can also enhance the photocatalytic activity due to the increase in the population of attainable active sites and the regulation of the d-band energy center becoming closer to the Fermi level. However, as a general effect, the presence of Fe lowers the affinity of the Ni for CO₂ and increases the affinity of the Fe-Ni MMOF for H₂O due to the lower number of d orbital (d⁶) electrons. Also, similar to the Fe-MMOF, Ni-MMOF can be explored more in the future in terms of application and modulate the content of Ni into MMOF besides other metals to achieve their best performance. However, the electrocatalytic procedures are well defined in this category, but their applications in photocatalytic, sensing, and catalytic organic transformations can be focused more in the future.

Table 2. Summary of the reported studies describing Ni-MMOFs or their derived composites and materials in diverse applications, indicating additional metals and their efficiency data.

Ni-MMOF	Other Metals	Application	Efficiency	Ref.
Er _{0.5} Ni-BDC MOF	Er	Electrocatalyst/Water splitting	C.d: OER: 100 and HER: 10/ O.v: OER: 420 and HER: 310/ T.f: OER: 99.0 and HER: 103	¹⁶⁵
MIL-53(Ru-NiFe)	Ru/Fe	Electrocatalyst/Water splitting	C.d: OER and HER: 50 Cell voltage: 50/ O.v: OER: 210 and HER: 62/ T.f: OER: 42.0 and HER: 49/ C.v: 1.6	¹⁸¹
Mn _{0.52} Fe _{0.71} Ni-MOF-74	Mn/Fe	Electrocatalyst/Water splitting	C.d: OER: 100 and HER: 10/ O.v: OER: 267 and HER: 99/ T.f: OER: 36.7 and HER: 103.8	⁶⁰
Co-Ni-Al-MOFs ^a	Co/Al	Electrocatalyst/Water splitting	C.d: OER and HER: 50 / O.v: OER: 220 and HER: 174/ T.f: OER: 97 and HER: 108	¹⁸²



Pt–NiFeMOF ^b	Pt/Fe	Electrocatalyst/Water splitting	C.d: OER and HER: 100 Cell voltage: 10/ O.v: OER: 261 and HER: 125/ T.f: OER: 40.43 and HER: 77.34/ C.v: 1.45	183
FeCoMnNi-MOF-74	Fe/Co/Mn	Electrocatalyst/Water splitting	C.d: OER: 50, HER: 10, and Cell voltage: 10/ O.v: OER: 250 and HER: 108/ T.f: OER: 41.28 and HER: 72.89/ C.v: 1.62	184
Co _{0.2} Fe _{0.8} Ni-OCNF	Fe/Co	Electrocatalyst/ Water splitting	C.d: OER, HER, and Cell voltage: 10/ O.v: OER: 291 and HER: 259/ T.f: OER: 36.1 and HER: 94.2/ C.v: 1.65	52
Ni-MOF-Fe-2	Fe	Electrocatalyst/ OER	C.d: 10/ O.v: 269/ T.f: 47.1	185
Ni _{0.5} Fe _{0.5} -THQ	Fe	Electrocatalyst/ OER	C.d: 10/ O.v: 272/ T.f: 47.9	168
Fe _{0.5} -BMM-10-700 ^c	Fe	Electrocatalyst/ OER	C.d: 50/ O.v: 359/ T.f: 79.2	186
NiFe-NDC _{0.9} BDC _{0.1}	Fe	Electrocatalyst/ OER	C.d: 10/ O.v: 295/ T.f: 69.4	187
NiFe-MOF-BF4-0.3	Fe	Electrocatalyst/ OER	C.d: 10/ O.v: 237/ T.f: 41	167
NiFc [’] 0.4Fc _{0.6} /NF ^d	Fe	Electrocatalyst/ OER	C.d: 100/ O.v: 213/ T.f: 45	51
NiFe-GA	Fe	Electrocatalyst/ OER	C.d: 100/ O.v: 236/ T.f: 28.74	172
(Ni ₂ Co ₁) _{0.925} Fe _{0.075} -MOF ^e	Fe/Co	Electrocatalyst/ OER	C.d: 10/ O.v: 257/ T.f: 41.3	188
NiCoFe-NDA/NF	Fe/Co	Electrocatalyst/ OER	C.d: 10/ O.v: 215/ T.f: 64	169
FCN-BTC/NF	Fe/Co	Electrocatalyst/ OER	C.d: 300/ O.v: 268/ T.f: 29.3	189
NiCo _{1.09} BDC-Fc _{0.25} /NF	Fe/Co	Electrocatalyst/ OER	C.d: 50/ O.v: 263/ T.f: 41	190
FeCoNi-btz/NF	Fe/Co	Electrocatalyst/ OER	C.d: 10/ O.v: 263/ T.f: 64	191
NiFe _{0.2} Co _{0.3} -ZIF ^f	Fe/Co	Electrocatalyst/ OER	C.d: 100/ O.v: 216/ T.f: 23.25	166
NiFeZn MOF nanosheets ^g	Fe/Zn	Electrocatalyst/ OER	C.d: 10/ O.v: 233/ T.f: 37.8	192
Ni ₁ Fe ₁ Cr _{0.3} -MOFs ^e	Fe/Cr	Electrocatalyst/ OER	C.d: 10/ O.v: 333/ T.f: 66	193
Ni ₄ Co ₄ Fe ₂ -MOFs ^e	Fe/Co	Electrocatalyst/ OER	C.d: 10/ O.v: 243/ T.f: 48.1	194
Ru@NiCo-MOF HPNs	Ru/Co	Electrocatalyst/ OER	C.d: 10/ O.v: 284/ T.f: 78.8	195
(Ni ₃ Co ₁) ₃ Fe ₁ -MOFNss ^e	Fe/Co	Electrocatalyst/ OER	C.d: 10/ O.v: 245/ T.f: 50.9	196
FeCo _{0.5} Ni _{2.5} -NBs	Fe/Co	Electrocatalyst/ OER	C.d: 10/ O.v: 273/ T.f: 51.1	197
FeNiCo-1,3,5-BTC-MOF	Fe/Co	Electrocatalyst/ OER	C.d: 10/ O.v: 239/ T.f: 42.4	198
Fc-NiCo-BDC	Fe/Co	Electrocatalyst/ OER	C.d: 200/ O.v: 234/ T.f: 32	174
NiFe-25 ^g	Fe	Electrocatalyst/ OER	C.d: 10/ O.v: 299/ T.f: 48.1	199



t-NiCoFe-LDH	Fe/Co	Electrocatalyst/ OER	C.d: 10/ O.v: 277/ T.f: 68.83	200
Ni-MOF-Fe-Se-400	Fe	Electrocatalyst/ OER	C.d: 10/ O.v: 242/ T.f: 41.25	201
CoNi-Cu(BDC)	Co/Cu	Electrocatalyst/ OER	C.d: 10/ O.v: 327/ T.f: 75.7	202
FeCoNiMnMOF/NF	Fe/Co/Mn	Electrocatalyst/ OER	C.d: 50/ O.v: 239/ T.f: 62.05	50
HE-MOF	Fe/Co/Zn/Mo	Electrocatalyst/ OER	C.d: 50/ O.v: 254/ T.f: 61	171
CoNiP-0.25 ^h	Co	Electrocatalyst/ HER	C.d: 20/ O.v: 170/ T.f: 52	203
NiMo/ CuO@C	Cu/Mo	Electrocatalyst/ HER	C.d: 10/ O.v: 85/ T.f: 290	204
NiRu _{0.13} -BDC	Ru	Electrocatalyst/ HER	C.d: 10/ O.v: 36/ T.f: 32	173
In/Ni-MOF^o	In	Electrocatalyst/ HER	C.d: 10/ O.v: 215/ T.f: 131.11	205
NiFe-MIL-53-NH ₂	Fe	Electrocatalyst/ UOR	C.d: 50/ O.p: 1.398/ T.f: 14	206
TM-MOF-800	Co/Zn	Electrocatalyst/ UOR	C.d: 10/ O.p: 1.37/ T.f: 137	207
Fc-NiCo-BDC	Fe/Co	Electrocatalyst/ UOR	C.d: 10/ O.p: 1.35/ T.f: 41	174
NiFeMn-pma	Fe/Mn	Battery/ LIBs	C.d: 100/ capacity: 624/ cycle: 100	208
Fe-Co-Ni NFSs	Fe/Co	Battery/ LIBs	C.d: 1000/ capacity: 489/ cycle: 1000	209
Ni-MnO/PC	Mn	Battery/ AZIBs	C.d: 3000/ capacity: 347.4/ cycle: 6000	210
Co/Ni-MOF ⁱ	Co	Supercapacitor	S.p: 2608/ C.d: 1.0 (5000 cycle)/ E.d: 47.3/ P.d: 780/ retention: 88%	211
NiCoMOF-2 ^h	Co	Supercapacitor	S.p: 108.5/ C.d: 0.5 (6500 cycle)/ E.d: 45.7/ P.d: 450.6/ retention: 84.3%	70
2D CoNi(1:6)-MOF ^j	Co	Supercapacitor	S.p: 455/ C.d: 0.5 (3000 cycle)/ E.d: 38.8/ P.d: 263.3/ retention: 73.9%	212
VNi-MOF NSAs/NF	V	Supercapacitors	S.p: 516.5/ C.d: 1.0 (12000 cycle)/ E.d: 43/ P.d: 800/ retention: 85.6%	213
Zn ₁ Ni ₃ -M ^k	Zn	Supercapacitor	S.p: 466.5/ C.d: 0.5 (2500 cycle)/ E.d: 9.55/ P.d: 3600/ retention: 44%	214
NiMn-S ^l	Mn	Supercapacitor	S.p: 2510.15/ C.d: 1.0 (5000 cycle)/ E.d: 82.8/ P.d: 800/ retention: 84.5%	178
Ni-Co-Mn _{0.25} MOF ^j	Co/Mn	Supercapacitor	S.p: 1575/ C.d: 1.0 (5000 cycle)/ E.d: 73.56/ P.d: 399/ retention: 81.64%	215
NiCoMn-MOF ^m	Co/Mn	Supercapacitor	S.p: 1000/ C.d: 4.0 (5000 cycle)/ E.d: 55/ P.d: 2467/ retention: 97%	216



NiCoMn—HMT ^m	Co/Mn	Supercapacitor	S.p: 905/ C.d: 3.0 (5000 cycle)/ E.d: 78/ P.d: 3500/ retention: 96%	217
[Ni(μ_3 -pic) ₂ -K(μ -SCN)] _n	K	Photocatalyst/ Dye degradation	94% / R ² : 0.964/ reuse: 4 cycles	218
Fe-Ni-P ^e	Fe	Photocatalyst/ Water splitting	H ₂ and O ₂ production: 5420 and 900.3/ reuse: 4 cycles	80
FeNi-MOFs ^e	Fe	Photocatalyst/ Pollutant degradation	Fe ²⁺ recovery with Fe ³⁺ /Fe ²⁺ cycling efficiency >58%	219
Ni _{0.75} Mg _{0.25} -MOF-74	Mg	Photocatalyst/ CO ₂ reduction	HCOO ⁻ yield: 0.64	46
HTHATN-Ni-Pt-NS	Pt	Photocatalyst/ Hydrogen evolution	Band gap: 1.11/ hydrogen evolution rate: 47.2 mmol g ⁻¹ h ⁻¹	82
NiZrCu-BDC	Zr/Cu	Photocatalyst/ CO ₂ reduction	Methanol: 41.05 μ mol h ⁻¹ g ⁻¹ / Ethanol: 36.62 μ mol h ⁻¹ g ⁻¹	16
3Ni-Ce/C ^h	Ce	Catalyst/ Hydrodeoxygenation of lignin derivatives vanillin	>95.0%/ selectivity: 81.4%/ reuse: 4 cycles	79
CuNi-MOFs ^e	Cu	Catalyst/ Reduction of 4-nitrophenol	apparent rate constant: 0.153 s ⁻¹ / reuse: 5 cycles	220
Ni/Cu-MOFs ⁿ	Cu	Sensing/ Glucose biosensors	detection limit: 0.51 μ M/ sensitivity: 26.05 μ Ac m^{-2} mM ⁻¹	221
NiCo-HHTP	Co	Sensing/ Biosensor for miRNA-141	detection limit: 0.69 fM	222
Ni/Co(HHTP)MOF	Co	Sensing/ Determination of glucose in serum and beverage	detection limit: 100 nM/ sensitivity: 3250 μ A mM ⁻¹ cm ⁻²	223
NiCo-MOF	Co	Sensing/ Glucose biosensing	detection limit: 0.29 μ M/ sensitivity: 0.6844 mA mM ⁻¹ cm ⁻²	224
NiCoFe-MOF	Fe/Co	Sensing/ H ₂ O ₂	detection limit: 2.1 μ M	225
Ni Fe-MOF	Fe	Removal/ dye and antibiotic	adsorption removal (Q _{max}): 395.9 mg g ⁻¹ / removal of tetracycline : 568.1 mg g ⁻¹	226
BUT-85	Ni	Separation/ C ₂ H ₂ : CO ₂	pH stability: 3 to 13	227

C.d: current density given in A g⁻¹ or mA cm⁻² for energy applications; O.v: overpotential given in mV; T.f: Tafel slope given in mV dec⁻¹; C.v: cell voltage given in V; O.p: onset potential given in V; in the most research capacity and S.p (specific capacitance) is given in F/g, C/g, and mAh g⁻¹; E.d: energy density given in Wh kg⁻¹; P.d: power density given in W kg⁻¹; can see the references; bandgap given in eV; AQE/ photocurrent density (pd) given in μ A cm⁻²; RT: room temperature; TOF; TON; E_a: Energy activation given in kJ mol⁻¹; for further details can see the references. NS: nanosheets; LDH; OCNF: derived oxygen carbon nanoflower; THQ: tetrahydroxy-1,4-benzoquinone hydrate; GA: gallic acid; HPNs: hollow porous nanospheres; NBs: nano-bundles; HE: high entropy; TM: trimetallic;



pma: Benzene-1,2,4,5-tetracarboxylic acid; NFSs: nano frame superstructures; HTHATN: Sterminated hexathiohexaaazatrphinaphthylene; HHTP: 2,3,6,7,10,11-hexahydroxytriphenylene; BUT: Beijing University of Technology; NSAs: nanosheet arrays.

^a BTC and bipyridine as linkers; ^b NiFe-BDC nanosheet agglomerates grown on nickel foam; ^c linkers for BMM denoted as H₃TPO (tris-(4-carboxylphenyl) phosphine oxide) and dabco (1,4-Diazabicyclo [2.2.2]-octane); ^d comprised of mixing ligands 1,1'-ferrocene dicarboxylic acid (Fc') and defective ferrocene carboxylic acid (Fc); ^e BDC as the organic ligand; ^f 2-methylimidazole as organic linker; ^g derived from MOF-74; ^h BTC as linker; ⁱ p-Phthalic acid; ^j BPDC: biphenyldicarboxylate as linker; ^k containing melamine (MA) and 2,5-thiophene dicarboxylic acid (TDA) as ligand; ^l 2,5-dihydroxybenzene-1,4-dicarboxylic acid (H₄DOBDC) as linker, ^m HMT: hexamethylenetetramine as linker; ⁿ glutaraldehyde as linker; ^o BDC and Trz (1,2,4-triazolate) as organic linker.

6. Cobalt-based MMOFs

Co-MMOFs and their relative derived materials are utilized in various applications, including sensing, electrocatalysis, catalysis, energy storage systems, and even photocatalysis.²²⁸⁻²³⁵ The incorporation of a second metal into the structure of cobalt-based MOFs has been reported to enhance the performance of Co-MMOF compared to monometallic Co-based MOFs. Enhanced efficiency can be attributed to the synergistic effect between the multiple metals present in MOFs.²³⁶

It has been demonstrated that the synthesis of bimetallic MOFs with a uniform distribution of metal centers can be achieved by placing two ions with similar radii in the MOF structure. The Co²⁺ ion has a similar radius to that of the Zn²⁺ ion, which allows for the uniform distribution of these two metals. Consequently, Co²⁺ and Zn²⁺ can be distributed uniformly within the bimetallic MOF system, thereby facilitating the synthesis of an appropriate CoZn-MMOF with enhanced performance.²³⁷ For example, Jianbin Zheng and colleagues synthesized a dopamine electrochemical sensor. Dopamine is a neurotransmitter that carries a vital role in the human body. It is widely distributed throughout the cardiovascular system, the central nervous system, the kidneys, and the endocrine system. An elevated concentration of dopamine is indicative of pathological disorders such as Parkinson's disease and schizophrenia. For this reason, the quantification of this substance in body fluids is of great significance. In the 2D Co/Zn-TCPP material (TCPP: tetrakis(4-carboxyphenyl)porphyrin), the doping of cobalt and zinc metal ions is beneficial for electron exchange and transfer with dopamine. Consequently, the cooperative effect of Zn²⁺ and Co²⁺ active centers enhances the electrocatalytic activity of this MOF, thereby



facilitating an excellent sensing capability for dopamine detection with a detection limit of 1.67 nM for a signal-to-noise ratio of 3 and the response being linear with the dopamine concentration in the range from 5 nM–177.8 μ M.²²⁸ Besides parent Co-MMOFs, Co-MMOF-derived materials are widely employed in electrochemical sensing, the removal of organic pollutants, medicine, and other areas. The transformation of the Co-MMOF can be accomplished by calcination under an inert atmosphere. The calcination of Co-MMOFs at low temperatures to carbonize the organic ligand results in the production of metal hybrids in the form of homobimetallic hollow nanocages (C-CoM-HNC; C: carbonization at 350 °C for 2h; HNC: hollow nanocages). This procedure allows for the controlled alteration of the structure of Co-MMOF precursors, while simultaneously facilitating the formation of synergistic active sites with cobalt alloys, thereby enhancing the catalytic activity and subsequently improving the performance of the derived material. These materials are utilized in fields such as catalysis and electrocatalysis, including electrochemical sensing and pollutant removal. For instance, Yuming Huang et al. calcined a CoCu-MOF and employed this material as a multifunctional nano enzyme for the degradation of organic pollutants, including RhB, and for a bioassay targeting acetylcholinesterase (AChE). Copper-doped C-CoCu-HNC nanostructures demonstrate enhanced performance with respect to other monometallic C-Co-HNCs as peroxymonosulfate (PMS) and oxidase activators. The incorporation of copper into the structure of this MOF results in a higher density of surface oxygen vacancies during the conversion of CoCu-MOF to C-CoCu-HNC, thereby enhancing its catalytic activity. The enhanced catalytic activity of C-CoCu-HNC is reflected in the production of higher quantities of $\text{SO}_4^{\cdot-}$ through the effective activation of PMS, thereby accelerating the decomposition of RhB dye. Moreover, this enhanced catalytic activity enables C-CoCu-HNC to exhibit a potent sensitivity for the detection of AChE activity, with a detection limit of 0.1 mU/L. AChE is a primary cholinesterase in the body, and its activity is associated with neurodegenerative disorders such as Alzheimer's disease. Therefore, measuring its activity in real body fluids is important from an analytical standpoint. The C-CoCu-HNC, produced with its oxidation activity, may be considered a sensitive bioassay for screening AChE activity. After configuration optimization, the O_2 chemically binds with one of the terminal oxygens connecting to the surface of Co_3O_4 . But in terms of CuCo_2O_4 , both oxygen atoms connect to the Co and Cu on the surface. This tighter connection can buttress electron transport from the Co and Cu to the antibonding π^* orbital of O_2 and lower the strength of the O–O bond in O_2 . And leads to the superior adsorption and electron-donating



capability toward PMS.²³⁸ In another instance, bimetallic Co–Pr–BDC MOF exhibits performance in bio-sensing applications via response to altering creatinine concentrations, resulting in the detection limits of 0.12 mM. The synergistic effect between Co and Pr (praseodymium), which incorporates lanthanides such as Pr into the structure, can present f-f transitions and boost the absorption in the visible spectrum, and with the possibility of generating hydrogen bonding, can be the cause of better performance of the bimetallic MOF.²³⁹

Also, Co-MMOFs are one of the most used materials in electrocatalysis. In bimetallic Co/M MOFs, the presence of an additional metal can facilitate charge transfer, augment interaction between MOF and electrolyte, tune the redox properties of the active sites, regulate amorphous and crystalline MOF structure, optimize the electronic structure, and raise the intrinsic activity of Co MOFs as electrocatalysts. In one example, a bimetallic Ru-doped Co-oxalate MOF was transformed at 300 °C for 2 h in a muffle to achieve OX-Co₃O₄-Ru that exhibits excellent electrocatalytic activity for HER and OER due to the increase in oxygen vacancies and higher surface hydrophobicity.²⁴⁰ The performance of OX-Co₃O₄-Ru is summarized in Table 3. Another example of multi-metallic Co-based MOF-derived material used in electrochemical water splitting is tetra-metallic Co-V-FeNi LDHs obtained by using ZIF-67 as a source of Co that, in combination with vanadyl acetylacetone and Ni and Fe salts, form a FeNi-LDH doped with Co and V. The role of ZIF-67 is key to controlling the tridimensional morphology of the resulting LDH. This tetrametallic Co-V-FeNi LDHs operates at a cell voltage of 1.62 V at a current density of 10 mA cm⁻², which is a lower voltage than other counterparts. This enhanced performance has been attributed to the morphology inherited from the ZIF-67 with accessible sites, the presence of Co, which is a more active site, the electronic interaction between V and Co, and synergistic effects with the other metal ions, all contributing to the augmentation of intrinsic electrocatalytic activity and a larger surface area.²⁴¹ In one of the examples reporting OER using bimetallic Co-based MOFs, CoFe(dobpdc) (dobpdc: 4,4'-dihydroxybiphenyl-3,3'-dicarboxylate) nanorods grown on NF. As commented earlier, grown electrocatalysts on NF generally result in better electrocatalytic performance due to the lesser internal electrical resistance between the electrocatalyst and the NF because of the better interfacial contact between them. In the present case, the optimal CoFe(dobpdc) shows better electrocatalytic activity compared to another type of synthesized nanorods in both 0.1 M and 1.0 M KOH electrolyte due to the **i**) the appropriate morphology and long aspect ratio improves positively the electrocatalytic activity, Co contributing to the MOF



thickening, therefore, adjusting growth and orientation, **ii)** the solvent used in the MOF synthesis also influences OER activity that requires high wettability of the porous materials to augment affinity of MOF for NF and optimize nanorod growth, and **iii)** analogously to other electrocatalytic processes, also in OER exposure of a high density of active sites and synergistic effect between metal ions improves the electrocatalytic response.²⁴² In another example, a 2D Co-based MOF constituted by ultrathin nanosheets was prepared and submitted to post-synthetic Fe doping to obtain a mixed valent $(\text{Fe(II)}_1\text{Fe(III)}_1)_{0.6}/\text{NMOF-Co}$ (NMOF: MOF nanosheets) This $(\text{Fe(II)}_1\text{Fe(III)}_1)_{0.6}/\text{NMOF-Co}$ was found to exhibit superior OER activity compared to the bulk counterparts and commercial RuO_2 , having lower Tafel slope of 50 mV dec^{-1} in alkaline media. The excellent performance of this MOF was found to derive from the fast charge transport, higher density of exposed active sites, and synergistic effect between mixed valence Fe and Co-based ultrathin nanosheet MOF.²⁴³ In another case of CoFe MMOF, a 2D Co/Fe MOF having tetrapyridyl linkers coordinated in equatorial positions around the metal ions to form the structure and two sulfocyanide groups coordinated in apical positions with the optimal Co/Fe ratio of $\text{Co}_{0.6}\text{Fe}_{0.4}$ -MOF exhibited a superior activity compared to Co-MOF, Fe-MOF, Co/Ce-MOF, Co/Mn-MOF, and Co/Ni-MOF counterparts, thus illustrating the potential of MMOFs to tune the electrocatalytic activity. However, the C_{dl} of Co/Fe-MOF is lower than that of Co/Ce-MOF. Based on XPS data, the larger C_{dl} of Co/Ce-MOF was attributed to the weak coordination of Ce ion, which causes more structural defects and, therefore, larger ECSA. However, despite the larger C_{dl} , Co/Ce-MOF has a scant population of active sites, which is detrimental to the OER activity. The higher Fe/Co-MOF activity is due to the influence of doping Fe into the redox properties of Co-S-Co that makes it easier to reach the Co^{3+} valence state and increases the density of active sites. Also sulfur in this structure plays a positive role in enhancing OER activity.²³⁶ In one case of trimetallic Co MMOF, a 2D Fe–Ni–CoOOH-TPA (TPA denoted as terephthalic acid) with ligand defects exhibited lower R_{ct} and higher C_{dl} for OER activity. The material consisted of a heterojunction of polycrystalline metal (oxy)hydroxide (MOOH) and amorphous metal oxides/hydroxides coordinated with TPA. It was prepared using ZIF-67 as a source of Co^{2+} ions that were etched by TPA to form the novel Fe–Ni–CoOOH-TPA composite. In this heterojunction, the valence band potential of Fe–Ni–CoOOH-TPA is 0.2 eV, which is lower than other counterparts, indicating that the installation of functional 1,4-BDC shifts the valence band of Fe–Ni–CoOOH-TPA closer to the Fermi level (E_F). When the band gap decreases, conductivity can increase by reducing the electron



transition barrier from the valence to the conduction band. Also, the hydrophilicity of Fe–Ni–CoOOH-TPA can enhance electrolyte penetration into the electrocatalyst micropores, resulting in an increased active surface area, and speeding the reaction kinetics, besides the positive impact of structural defects increasing the density of undercoordinated metal positions.²⁴⁴ Co MMOFs have also been used to obtain derived materials to be used as OER electrocatalysts. In one of the examples, bimetallic $\text{Co}_3\text{O}_4/\text{CoFe}_2\text{O}_4$ decorated on NF was derived from mixed metal Co/Fe MOF using nicotinic acid as a linker grown on NF and calcined at 500 °C. The resulting material exhibits an overpotential of 215 mV, this good performance was attributed to: **i**) the presence of Fe^{3+} in octahedral sites of CoFe_2O_4 acting as active site and decreasing overpotential of bimetallic derived MOF, **ii**) the presence of octahedrally coordinated Co^{3+} sites in Co_3O_4 that boosts conductivity and adsorption-desorption of oxygen intermediates and, **iii**) integration and synergistic effect between Co_3O_4 and CoFe_2O_4 cooperating to OER.²⁴⁵ Another example of multi-metallic derived Co-based MOFs as electrocatalysts for OER is the trimetallic $\text{WCoFe}_{0.3}\text{-CNF}$ (CNF: carbon nanoflakes) derived from multimetallic hybrid zeolitic imidazolate framework using Co^{2+} , Fe^{2+} , and WO_4^{2-} ions as metal salts. When the feed Fe/Co ratio is 0.3, the molar ratio of $\text{Co}^{3+}/\text{Co}^{2+}$ reaches 1.38 which is the highest molar ratio among the samples in the series, resulting in the best OER activity in Table. 3. It has been proposed that each metal has a specific prevalent role, Co playing the role of the active site, Fe improves conductivity, and W acts as an electron density donor to optimize the electronic structure of Fe and Co.²⁴⁶ CoY-MOF grown on NF has been reported to be an electrocatalyst for HER-GOR which exhibits major electrocatalytic activity with a low cell voltage of 1.36 V. Co acts as the active center and Y regulating its electronic structure with a synergic effect between them, with the high surface area of the MOF leading to an improved HER and GOR activity by exposure of a large density of active sites. A low overpotential of 100 mV at a current density of 10 mA cm⁻² with a Tafel slope of 68 mV dec⁻¹ was reported for HER. Also, the Tafel slope for GOR was only 98 mV dec⁻¹, indicating faster kinetics than OER for which the Tafel slope on the CoY-MOF/NF electrode was 123 mV dec⁻¹.⁶¹ Regarding ORR and zinc-air batteries, trimetallic MOF-derived MnCoNi-C-D exhibits 0.82 V in half-wave potential for ORR. Moreover, zinc-air batteries reached good power density, specific capacity, and higher open-circuit potential (OCV) in 1.46 V, which indicates better electrochemical performance for this MOF-derived material due to the generation of MnCo_2O_4 and NiO, while the hollow structure facilitates electron transfer and provides a large density of



accessible active centers for the ORR/OER catalysis.²⁴⁷ Furthermore, the presence of an additional metal can also increase the yield and faradaic efficiency of Co in NRR, providing sites for the adsorption and dissociation of N₂ molecules. In the case of NRR, the bimetallic MOF-derived Co-based material, Zn–Co₃O₄, exhibits an ammonia yield of 22.71 µg h⁻¹ mg_{cat}⁻¹. The high electrochemical activity is achieved through a combination of oxygen vacancies, which act as Lewis acid centers, cobalt, which acts as electron-rich centers to buttress the adsorption and dissociation of nitrogen molecules, and doping zinc sites which facilitate electron transport. Based on XPS analysis, electron transfer from zinc to cobalt was observed, thus, increasing the electron density of Co²⁺. Hence for an adequate charge balance in the mixed oxide, some oxygen atoms should exit from the structure and produce oxygen vacancies. Optimization of these parameters leads to the highest NRR activity.⁶⁸ For more details on Co-MMOFs, see Table 3.

Co-MMOFs are one of the most widely used materials for energy storage. The synergistic effect between Co and other metals can result in higher activity and stability of the material as an electrocatalyst in reactions and as a supercapacitor active material, which indicates the positive impact of using mixed valence Co^{2+/3+}. Also, materials derived from Co-MMOFs are among the materials with the highest energy storage performance. For instance, Zn_{0.25}Ni_{0.75}Co-LDH-BA⁻/AA⁻ (BA⁻ = benzoate anion and AA⁻ = acetate anion) shows a specific capacity of 275 mAh g⁻¹ at a current density of 1 A g⁻¹, making the resulting assembled supercapacitor device of this MOF-derived material interesting for energy storage applications. The high specific charge storage performance of this MOF-derived material is the result of **i**) the unique LDH morphology which facilitates penetration of electrolyte into the material and large specific surface area that leads to premier electrochemical proficiency, **ii**) the synergistic impact between the three metal ions and the optimization of Zn/Ni ratio since Co and Ni ions accelerate redox reactions and lead to the regulation of specific capacity, while the Zn ions buttress the electrical conductivity.²⁴⁸ In another example of Co MMOF-derived material employed as an active component in supercapacitors, NiCoMn-S was found to have superior storage efficiency compared to NiCoMn-OH, Co-S, NiCo-S, CoMn-S, Ni₁CoMn₃-S, Ni₃CoMn₁-S, thereby showing that optimized trimetallic derived NiCoMn-S has a better performance compared to its mono-metallic, bi-metallic, and trimetallic analogues with other ratios of the three metals. Thus, optimized trimetallic MMOF-derived NiCoMn-S exhibits a specific capacitance 2098.2 F g⁻¹ at a current density of 1 A g⁻¹, an energy density of 50 Wh kg⁻¹, and a power density of 850 W kg⁻¹, and these data decrease only 73.6 % for



6000 cycles, exhibiting notable capacitance retention. As shown in Figure 14, the potential window of the assembled device made of NiCoMn-S//AC is 0-1.7 V. This high activity was attributed to **i**) the appropriate electronegativity of sulfur being lower than oxygen implying that sulfide structures are more porous and flexible than the oxide counterparts, facilitating electron transport, **ii**) the smaller band gap of sulfides than oxides what increases charge storage efficiency that is responsible for more efficient promotion of redox reactions, **iii**) the larger BET area and higher porosity what leads to more exposed electroactive sites and facilitates electron or ion transport, emphasizing the importance of NiCoMn-S having higher surface area than CoS, α -NiS, CoS₂, NiMn sulfide, NiCo₂S₄, NiCo₂S₄-Co₉S₈, Ni_xCo_{3-x}S₄, Cu(NiCo)₂S₄- Ni₃S₄ counterparts, and **iv**) existence of mixed-valence Ni²⁺/Ni³⁺, Co²⁺/Co³⁺ in the material as revealed by XPS which with their synergistic effect with Mn²⁺ provide higher density of electro-active sites for redox reaction and boost energy storage application.²⁴⁹ Furthermore, incorporation of Co into Mn-MOF also can be effective as new energy storage devices.⁷³ However, based on the properties with a wide range of possible electronic configurations for Mn, it appears reasonable that MMOFs that contain Mn should also have considerable potential in those fields.⁷³ In one example of Mn-MMOF, TTFTB-MnCo-MOF (TTFTB = tetrabenzoate tetrathiofulvalene) the galvanostatic charge-discharge (GCD) performed in the range 0.1 V to 3.0 V versus Li⁺/Li exhibits an efficiency up to 57.1 % in the first specific discharge capacity. The full lithium-ion battery cell having a configuration TTFTB-MnCo-MOF||NMC 622 (NMC 622 corresponds to lithium nickel manganese cobalt oxide, with the numbers indicating the percentage of Ni, Mn and Co, LiNi₆Mn₂Co₂O₂ used as cathode material) reaches a capacity of 154.9 mAh g⁻¹ at 100 mA g⁻¹ in the 200th cycle. Also, TTFTB-MnCo-MOF||AC (AC active carbon) hybrid lithium-ion capacitor can achieve a specific energy of 141.4 Wh kg⁻¹ at a specific power of 0.25 kW kg⁻¹. The high energy storage efficiency is this batter-supercapacitor hybrid device having the TFF moiety in the MOF structure was attributed to several synergistic factors including the high porosity of the MOF, the presence of the sulfur-rich TTF ligand, and the bimetallic Mn²⁺ and Co²⁺ metal nature of the site. XPS analysis provides evidence that the S atoms of the TTF group are the sites associated with Li⁺ storage. Besides the S-rich TTF ligand, Mn²⁺ is responsible for good cycling performance and Co²⁺ increases the specific capacity.⁷³ Furthermore, incorporation of Cu into MOFs as one of the most widely employed elements in MMOFs, illustrates their capability in medicine and energy storage, also used as a corrosion inhibitor and photocatalyst in their mixed-metal forms.²⁵⁰⁻²⁵³ in the case of



energy storage, trimetallic NiCoCu-TPA MOF showed a performance of specific capacity of 417 C g^{-1} at 0.5 A g^{-1} . Also, construction of NiCoCu-TPA//AC attains energy density of 49.05 Wh kg^{-1} at 0.5 A g^{-1} and power density of 6400 W kg^{-1} at 8 A g^{-1} , and exhibits cycling stability. This performance can be attributed to the incorporation and synergistic effect among Ni, Co, and Cu, where Ni induces redox activity, while Co not only can induce redox activity but also improve structural stability, and eventually Cu incorporation can provide more faradaic redox sites and enhance the conductivity within the architecture.²⁵⁴

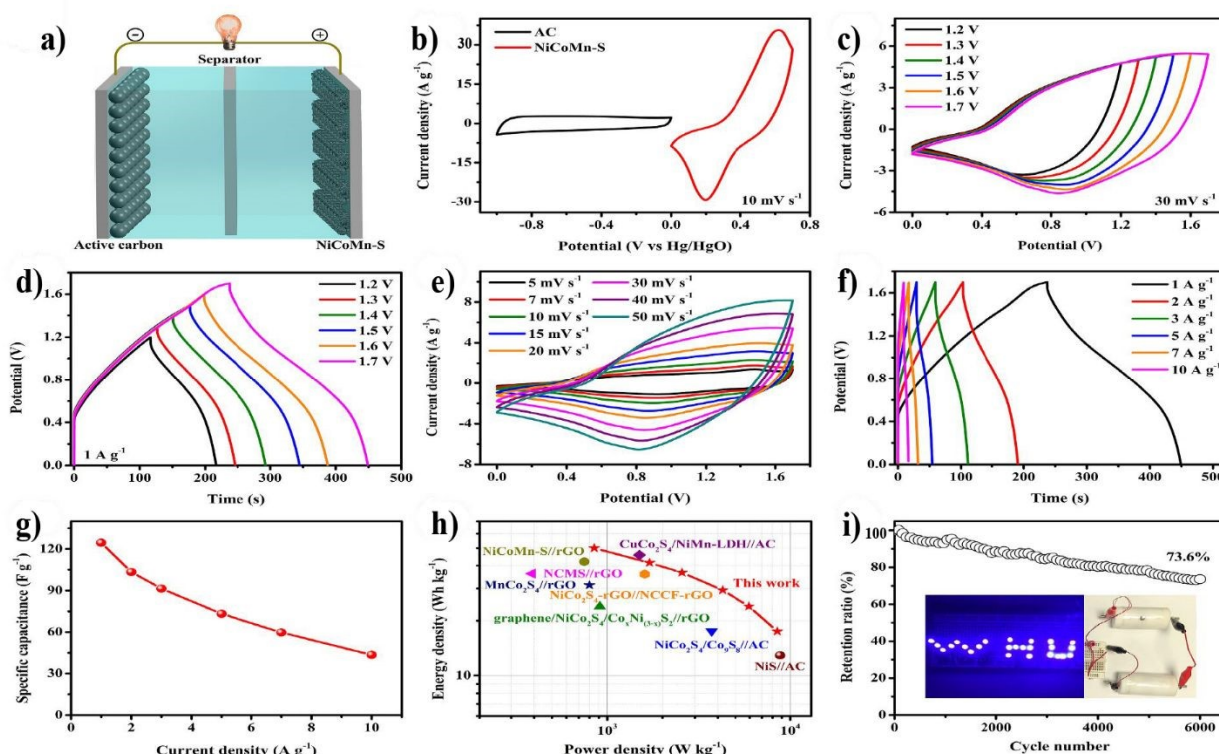


Figure 14. a) Illustration of the assembled NiCoMn-S//AC device; b) CV curves of NiCoMn-S and AC at 10 mV s^{-1} ; c) CV curves at a scan rate of 30 mV s^{-1} at different potential windows for the assembled device; d) GCD curves at a current density of 1 A g^{-1} at different potential windows for the assembled device; e) CV curves at different scan rates; f) GCD curves at different current densities for the assembled device; g) specific capacitance at different current densities for the assembled device; h) Ragone plots (energy density vs power density) of NiCoMn-S//AC and other assembled devices; i) cycling stability of the assembled device at 10 A g^{-1} . Reproduced with permission from ref.²⁴⁹ Copyright 2022 Elsevier.

Co-MMOFs exhibit a wide range of catalyst applications, due to the synergistic effect frequently found for Co combined to other metal ions. Co can easily activate O_2 molecules and

promote catalytic aerobic oxidation reactions and this catalytic activity can be enhanced by combination with other metals. Particularly, Co alongside heavy metals form MOF structures with a larger density of unsaturated coordination positions that can activate substrates and exhibit high TOF values, indicating better catalytic activity. One of the recent examples investigate the catalytic activity of bimetallic $\text{Pd}_{0.3}\text{Co}_{0.7}(\text{bim})_2$ (PdCo-ZIF) having a range of Pd/Co ratios toward CO_2 cycloaddition. It was found that the presence of Pd generate defects at the Co site in structure, reaching a TOF of 2501 h^{-1} which is superior to monometallic counterparts (Co-ZIF, Pd-ZIF). It was found that Pd-ZIF has no activity for this reaction, implying that undercoordinated cobalt ions at defects are the active centers in the material. The role of Pd was proposed to be the generation of a porous material with a high concentration of defective Co distorted sites behaving as Lewis acids.²⁵⁵ Regarding Ir incorporation with Co, they have attracted interest in photocatalyst applications, due to the use of Ir polypyridyl complexes in photo/electroluminescent devices and in photoredox synthesis.²⁵⁶ One of the examples is based on UiO-67, having some 2,2'-bipyridyl-4,4'-dicarboxylic acid ligands able to complex Ir at framework satellite positions. Besides the linker, other coordination positions around Ir were completed by either 2-phenylpyridine (ppy) or coumarin 6 (Cou6) of which the Ir complex with the UiO-67 framework and two Cou6 molecules was the best performing.²⁵⁶ Subsequent incorporation of either Co or Cu in the series of UiO67-Ir (ppy or Cou6) is illustrated in Figure 15. Ir complexes attached to the MMOF lattice act as strong visible-light-absorbing chromophores, particularly when having Cou 6 as a ligand. The presence of Cou6 alters the lowest unoccupied excited state of the system from $^3\text{MLCT}$ to ^3IL state (IL meaning internal ligand), which is much longer lived and more suited for photocatalytic reactions. In this way, when Co is also attached to free 2,2'-bipyridyl units, UiO67-Ir-Cou6/Co system reaches an H_2 production yield of $2440.4\text{ }\mu\text{mol g}^{-1}\text{h}^{-1}$, over 100-fold higher than that of UiO67-Ir-ppy/Co ($22.3\text{ }\mu\text{mol g}^{-1}\text{ h}^{-1}$) with $^3\text{MLCT}$ excited state. Co-incorporation of Cu centers, rather than Co, is very appropriate for photocatalytic CO_2 , forming HCOOH in a remarkable yield of $480.7\text{ }\mu\text{mol g}^{-1}\text{ h}^{-1}$. Therefore, it was concluded that the elaborated UiO67-Ir-Cou6/M, having Zr, Ir, and either Co or Cu, has a remarkable photocatalytic efficiency due to the properties of the ^3IL -type excited state of long lifetime as well as a strong visible light harvesting ability, thus, favoring photoreduction.²⁵⁶



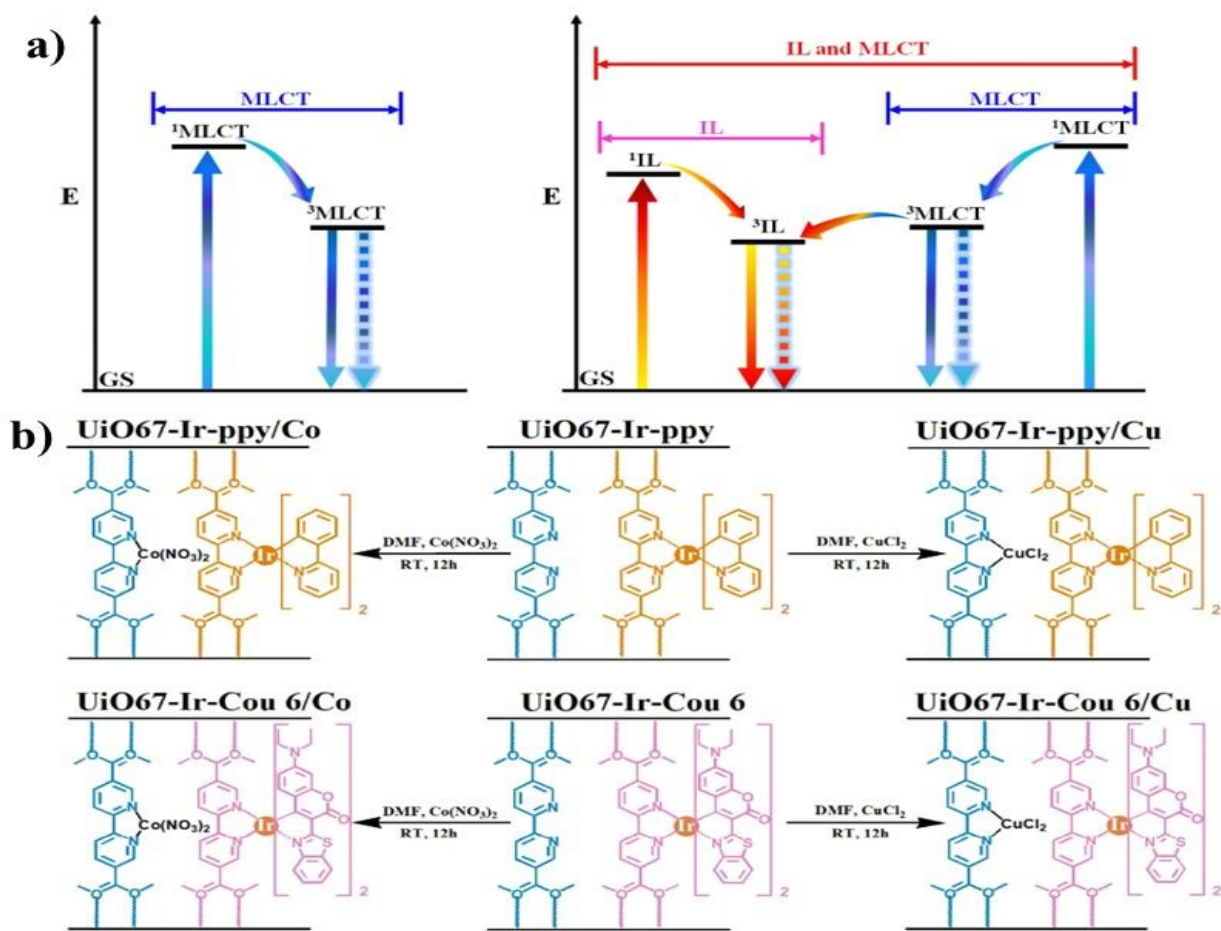


Figure 15. a) Diagram of the various energy levels available for Ir Uio-67 depending on the coordination environment around Ir ions; b) Illustration of the structure and post-synthetic modification of UiO67-Ir to form UiO-67-Ir-ppy or UiO67-Ir-Cou6 and the subsequent incorporation of Co(II) and Cu(II) ions. Reproduced with permission from ref.²⁵⁶ Copyright 2022 Wiley.

In OER, the use of an additional metal adjacent to Co can produce coordinatively unsaturated sites to facilitate nucleophilic attack of OH⁻, making more feasible the formation of reaction intermediates, such as Co(OH)₂ and CoOOH, which result in an enhancement of C_{dl} and the reaction kinetics. Also, the presence of an additional metal can favor the mixed valence of Co³⁺/Co²⁺ with the formation of Co³⁺, which has a higher oxidation potential than Co²⁺, facilitating a better OER performance. In total, Co, compared to other transition metals, is one of the most used metals in the reports dealing with MMOFs in catalytic applications. In one of the most studied combinations, Co and Zn in MMOF and derived materials exhibit a synergistic effect and complementary activity, Co activating O₂, and Zn being particularly efficient for H₂ activation.



This complementarity, together with the tuning of the electron density due to the differences in electronegativity, can be very beneficial for aerobic oxidation. Besides Zn, the combination of Co and heavy metals is beneficial for catalytic activity due to the generation of unsaturated coordination Co ions. Furthermore, the simultaneous incorporation of heavy metals and Zn results in stable, highly porous MMOFs. It seems that Zn induces porosity, while heavy metals increase structural stability. Also, their different affinity compared to the Co and Zn is a powerful tool for further tuning of the electronic density of the active sites. In comparison to other applications, Co-MMOFs have been less studied as photocatalysts. However, it can be implied that crystal engineering regulating Co-MMOF structure should also be beneficial for their photocatalytic activity, as reported also in other sections. Although same approach as Fe and Ni-MMOF is suggested to be focused more in the future, but synergistic effect between Co and Zn can be focused more on diverse applications such as energy storage. But still synergistic impact between Fe, Ni, and Co are growing trend in electrocatalysis with engineering in the content of mentioned metals and altering the linker of MOFs to see what kind of enhancing can occur in their performance compared to the bimetallic and monometallic counterparts, but in some experimental cases this idea might not be properly work due to the structural issues or change in their performance with outstanding results.

Table 3. Summary of reported applications of Co-MMOFs or their derived materials with indication of their efficiency.

Co-MMOF	Other Metals	Applications	Efficiency	Ref.
OX-Co ₃ O ₄ -Ru	Ru	Electrocatalyst/ Water splitting	C.d: OER and HER: 100 Cell voltage: 500/ O.v: OER: 286 and HER: 49/ T.f: OER: 51.2 and HER: 63.3/ C.v: 1.71	240
Co-V-FeNiLDHs	Ni/Fe/V	Electrocatalyst/ Water splitting	C.d: OER: 50 and HER: 10 Cell voltage: 10/ O.v: OER: 244 and HER: 180/ T.f: OER: 58 and HER: 121.5/ C.v: 1.62	241
Ni/ Co-DH	Ni	Electrocatalyst/ OER	C.d: 10/ O.v: 229/ T.f: 86.6	257
NiCo(OH) _x @Co-MOF ^a	Ni	Electrocatalyst/ OER	C.d: 10/ O.v: 210/ T.f: 43	258
CoY-MOF/NF ^b	Y	Electrocatalyst/ OER	C.d: 10/ O.v: 100/ T.f: 68	61
Co/Fe (1:1)-MOF ^c	Fe	Electrocatalyst/ OER	C.d: 500/ O.v: 490/ T.f: 42	259
Co-MOF/Fe ₁₀ ^d	Fe	Electrocatalyst/ OER	C.d: 10/ O.v: 260/ T.f: 46.8	260
Co _{0.6} Fe _{0.4} -S-MOF	Fe	Electrocatalyst/ OER	C.d: 10/ O.v: 260/ T.f: 56	236
CoFe(dobpdc)-III	Fe	Electrocatalyst/ OER	C.d: 300/ O.v: 240/ T.f: 35.1	242



Co _{0.8} Fe _{0.2} -MOF ^e	Fe	Electrocatalyst/ OER	C.d: 10/ O.v: 237/ T.f: 36.3	261
Co _{0.9} Ce _{0.1} -BTC	Ce	Electrocatalyst/ OER	C.d: 10/ O.v: 308/ T.f: 107	262
Co ₁₅ Ni ₁ -MOF-3,5-H ₂ pdc	Ni	Electrocatalyst/ OER	C.d: 10/ O.v: 384/ T.f: 59	263
A _{2.5} B-CoNi MOFs ^f	Ni	Electrocatalyst/ OER	C.d: 10/ O.v: 300/ T.f: 45.27	264
WCoFe _{0.3} -CNF	Fe/W	Electrocatalyst/ OER	C.d: 100/ O.v: 258/ T.f: 44.8	246
G-FeNi-Co-ZIF-L	Fe/Ni	Electrocatalyst/ OER	C.d: 10/ O.v: 248/ T.f: 49.5	265
NF/Co ₃ O ₄ /CoFe ₂ O ₄	Fe	Electrocatalyst/ OER	C.d: 10/ O.v: 215/ T.f: 90	245
Co-CIF:FeNiMo	Fe/Ni/Mo	Electrocatalyst/ OER	C.d: 100/ O.v: 238/ T.f: 34	266
MoCoFe@NC	Fe/Mo	Electrocatalyst/ OER	C.d: 10/ O.v: 285/ T.f: 72	267
FeCo _{0.6} Ni _{0.4} - CAT	Fe/Ni	Electrocatalyst/ OER	C.d: 10/ O.v: 277/ T.f: 44.7	229
Fe-Ni-CoOOH-TPA	Fe/Ni	Electrocatalyst/ OER	C.d: 10/ O.v: 236/ T.f: 39	244
Co _{2.36} Fe _{0.19} Ni _{0.45} -btca	Fe/Ni	Electrocatalyst/ OER	C.d: 10/ O.v: 292/ T.f: 72.6	268
CoNiFe-ZIF-MFs	Fe/Ni	Electrocatalyst/ OER	C.d: 10/ O.v: 273/ T.f: 87	269
CuCoNi-OH	Ni/Cu	Electrocatalyst/ OER	C.d: 10/ O.v: 290/ T.f: 57.8	270
CoNiMn-MOF ^g	Ni/Mn	Electrocatalyst/ OER	C.d: 20/ O.v: 220/ T.f: 66	271
Ir@Co-BPDC	Ir	Electrocatalyst/ HER	C.d: 100/ O.v: 57/ T.f: 33.39	272
CoNi-MOF ^g	Ni	Battery/ ARZBs	C.d: 20000/ capacity: 344/ cycle: 1500	64
TTFTB-MnCo-MOF	Mn	Battery/ NMC 62	C.d: 100/ capacity: 154.9/ cycle: 200	73
Co-Mn-O/C-0.2	Mn	Battery/ LIBs	C.d: 1000/ capacity: 1088.5/ cycle: 600	273
ZNC ZIF-67	Ni/Zn	Supercapacitor	S.p: 247/ C.d: 0.1 (5000 cycle)/ E.d: 27.94/ P.d: 1300/ retention: 99%	231
Cu₂CoSnS₄	Cu/Sn	Supercapacitors	S.p: 393.5/ C.d: 0.7 (8000 cycle)/ retention: 88.5%	274
Ni-Zn-Co-S-0.25 ^a	Ni/Zn	Supercapacitor	S.p: 1930.9/ C.d: 1.0 (10000 cycle)/ E.d: 32.8/ P.d: 864.8/ retention: 92.2%	275
Zn _{0.25} Ni _{0.75} Co-LDH-BA ⁻	Ni/Zn	Supercapacitor	S.p: 275/ C.d: 1.0 (10000 cycle)/ E.d: 51.8/ P.d: 789/ retention: 94.6%	248
ZnCo ₂ Ni-LDH	Ni/Zn	Supercapacitor	S.p: 348.2/ C.d: 1.0 (10000 cycle)/ E.d: 54.4/ P.d: 4439/ retention: 86%	276
NiCoMn-S ^a	Ni/Mn	Supercapacitor	S.p: 2098.2/ C.d: 1.0 (6000 cycle)/ E.d: 50/ P.d: 850/ retention: 73.6%	249
Cu(NiCo) ₂ S ₄ /Ni ₃ S ₄	Ni/Cu	Supercapacitor	S.p: 1320/ C.d: 1.0 (5000 cycle)/ E.d: 40.8/ P.d: 7859.2/ retention: 85%	277
NiCoC/O-NiCoAl LDH	Ni/Al	Supercapacitor	S.p: 2400/ C.d: 1.0 (5000 cycle)/ E.d: 80/ P.d: 750/ retention: 82.3%	278
CoNiSe ₂ /FeNiCoSe ₂ YSBs ^a	Ni/Fe	Supercapacitor	S.p: 1091.2/ C.d: 1.0 (5000 cycle)/ E.d: 76.5/ P.d: 2378.7/ retention: 85%	279
NiCo-MOF-31	Ni	Supercapacitor	S.p: 1697.2/ C.d: 1.0 (5000 cycle)/ E.d: 26.56/ P.d: 750/ retention: 85%	280
NiCo-BDC@MIM	Ni	Supercapacitor	S.p: 2252/ C.d: 1.0 (2000 cycle)/ E.d: 40.2/ P.d: 972/ retention: 73.2%	281



Zn _{0.1} Co ₁ -MOF-D2-24	Zn	Catalyst/ Epoxidation of cycloalkenes	95.5%/ 90°C/ air/ 5h/ selectivity: 96.7%/ reuse: 10 cycles	282
Co₁Cu₁-MOF/PSM	Cu	Catalyst/ Degrades tetracycline in water	98.17%/ 30min/ reuse: 4 cycles	283
CuCo@C	Cu	Catalyst/ Hydrogenation of levulinic acid	100%/ 220°C/ 4h/ reuse: 5 cycles	284
La ₂ Co ₈ -MOF-BTC-H	La	Catalyst/ Epoxidation of cycloalkenes	96.2%/ airflow/ 80°C/ 5h/ selectivity: 98.7%/ reuse: 5 cycles	285
Pd ₂ Co ₈ -ZIF	Pd	Catalyst/ Cycloaddition reaction of CO ₂	E _a : 98.7/ 97.1%/ 12h/ TON: 5754/ TOF: 479/ reuse: 3 cycles	286
Pd _{0.3} Co _{0.7} (bim) ₂	Pd	Catalyst/ Cycloaddition reaction of CO ₂	94.3%/ 80°C/ 6h/ TOF: 2501/ reuse: 3 cycles	255
NUC-31	Tb	Catalyst/ Cycloaddition reaction of CO ₂	98.7%/ n-Bu4NBr/ 75°C/ 12h/ selectivity: 99%/ TOF: 8.23/ reuse: 5 cycles	230
Cu₆Fe_{0.8}Co_{3.2}@MIL-101	Fe/Cu	Catalyst/ Ammonia borane hydrolysis	E _a : 37.2/ 298k/ TOF: 23.2/ reuse: 7 cycles	287
CoNi-MOF ^h	Ni	Sensing/ Deoxynivalenol (DON) and salbutamol (SAL)	detection limits: 0.05 and 0.30 $\mu\text{g}\cdot\text{mL}^{-1}$ toward DON and SAL	288
Cu-Co-ZIF	Cu	Sensing/ Glucose	high sensitivity: 18.68 mA $\text{mM}^{-1}\text{cm}^{-2}$ / response time: 1.5 s/ detection limit: 2 μM	289
CoZn-MOF	Zn	Sensing/ Dopamine	detection limit: 0.67 μM	290
MnCo-MOF-74	Mn	Sensing/ Glucose	Sensitivity: 233.8 $\mu\text{A}\text{mM}^{-1}\text{cm}^{-2}$ / detection limit: (S/N: 3) : 1.31 μM	291

C.d: current density based on A g⁻¹ or mA cm⁻² for energy applications/ O.v: overpotential based on mV/ T.f: Tafel slope based on mV dec⁻¹/ C.v: cell voltage based on V/ O.p: onset potential based on V/ in the most research capacity and S.p (specific capacitance) is based on F/g, C/g, and mAh g⁻¹/ E.d: energy density based on Wh kg⁻¹/ P.d: power density based on W kg⁻¹/ all percentage in photocatalyst or catalyst represent yield, conversion or any efficiency of MMOFs which for further details can see the references/ bandgap based on eV/ apparent quantum efficiency (AQE)/ photocurrent density (pd) based on $\mu\text{A}\text{cm}^{-2}$ / RT: room temperature/ TOF: turn over frequency/ TON: turn over number/ E_a: Energy activation based on kJ mol⁻¹/ for further details can see the references. LDH: layered double hydroxide; NC: N-doped carbon; dobpd: 4,4'-dihydroxybiphenyl-3,3'-dicarboxylate; H₂pd: pyridine-2,4-dicarboxylic acid; CNF: carbon nanoflakes; TPA: terephthalic acid; btca: benzotriazole-5-carboxylate; BPDC: biphenyldicarboxylate; YSBs: yolk-shell nano boxes; TTFTB: tetrabenzoate TTF (tetraphiafulvalene).

^a MIM: 2-methylimidazole as organic ligand; ^b mixing ligand of triethylenediamine (TED) and 1,4-benzenedicarboxylic acid (BDC); ^c 4,40 -oxydibenzoic acid as linker; ^d BDC as the organic ligand; ^e dobpd as linker;



^f terephthalic acid (A) and 2, 5-dihydroxyterephthalic acid (B); ^g BTC as linker; ^h mixed organic ligand of 4-(1H-tetrazol-5-yl)benzoic acid (H₂TZB) and 2,4,6-tri(4-pyridyl)-1,3,5-triazine (TPT).

7. Zirconium-based MMOFs

Zr-MMOFs have been less investigated for energy storage and conversion systems due to their lower conductivity or when doping with other Zr MOFs. However, Zr-MMOFs have unique structures and considerable stability which can be beneficial for some energy applications. Thus, the addition of electroactive metals to Zr-MOFs can mitigate this low electrical conductivity, reaching a good stability/conductivity balance that makes Zr-MMOFs worth exploring in diverse energy applications. In one example, multi-metallic Zr-based MOFs 10Fe:90Ni@Zr-BTB (BTB: 1,3,5-tris(4-carboxyphenyl)benzene) was studied as an OER electrocatalyst exhibiting a high efficiency as indicated in Table 4. Initially, Zr-based MOF was chosen for this application due to its unique morphology, but large concentrations of Ni and Fe are required to promote OER activity. Also, Ni@Zr-BTB exhibits a high overpotential of 647 mV, showing the introduction of Fe into the MOF structure is necessary to regulate the activity of Ni oxyhydroxide and enhance OER catalytic activity.²⁹² Also, in term of medicine these types of materials are less explored. In this case, there are examples for using Zr-MMOFs in medicine, such as Zr–Cu MOF@ES@aH, which illustrates their efficiency toward human epidermal growth factor receptor 2-positive (HER2+) breast cancer.²⁵⁰ The role of Cu can be attributed to the conversion of Cu²⁺ to Cu⁺, which produces •OH to hamper redox homeostasis and Cu⁺ binding to lipoylated tricarboxylic acid (TCA) cycle proteins, destabilizing iron-sulfur clusters that lead to mitochondrial proteotoxicity.²⁵⁰

Due to the high valence of Zr⁴⁺, this element can introduce ultra-high structural stability, while modifying the acidity of Lewis centers, resulting in high catalytic activity of other metal ions present in the composition of the MOF.²⁹³⁻²⁹⁵ Also, in the case of high entropy MOFs, they can reduce the energy barrier and help the hydrogenation process.²⁹⁶ Thus, a bimetallic Zr-based MOF was prepared starting from Zr₆(μ₃-O)₄(μ₃-OH)₄ (MOF-808, BTC as ligand) with ZnEt₂ to form MOF-808-Zn. This bimetallic ZrZn-MOF was used as a catalyst for the selective CO₂ hydrogenation to methanol. The MOF catalyst was stable for at least 100 h at 250 °C. This stability is remarkable considering the relatively high temperature and H₂O is formed also as reaction products.²⁹⁷ It was found that the notable catalytic activity of bimetallic MOF was due to the formation of Zn²⁺–O–Zr⁴⁺ centers in the post-treatment of MOF-808, as confirmed by XAS



analyses. H_2 activated by Zn^{2+} centers and open $\text{Zn}^{2+}-\text{O}-\text{Zr}^{4+}$ sites result in CO_2 adsorption, activation, and conversion to methanol. The mechanism was addressed by DFT calculations that indicate that H_2 should be able to easily produce $\text{Zn}^{2+}-\text{H}^-$ and $\text{Zr}^{4+}-\text{O}-\text{H}^+$ through heterolytic H-H splitting at the $\text{Zr}^{4+}-\text{O}-\text{Zn}^{2+}$ center with a low energy barrier of 17.1 kcal/mol. Then, in the second step, H_2 can also be dissociated by the zinc (II) ion site and another $\text{Zr}^{4+}-\text{OH}$ group, triggering the production of the HCOO^* intermediate with an activation energy of 11.2 kcal/mol, even lower than the first step.²⁹⁸ In another instance, a bimetallic Ce Zr-MMOF with UiO-66 structure and aminoterephthalate ligand was used as a catalyst in the synthesis of propylene carbonate under batch conditions. The Ce Zr-MMOF was relatively stable with lesser leaching after 4 cycles. It is known that the presence of NH_2 as a substituent of the terephthalate ligand increases CO_2 adsorption of the MOF due to its basicity. In addition, bifunctional Lewis acid/base catalysts like UiO-66- NH_2 (Zr/Ce), having nodal defects with acid character and basic $-\text{NH}_2$ substituents, are very appropriate to promote CO_2 insertion into epoxides due to the dual activation of CO_2 by basic sites and epoxide by the nearby acid sites according to the mechanism indicated in Figure 16. The role of Ce in UiO-66- NH_2 (Zr/Ce) is to generate defective structural centers by effectively decreasing the coordination of the nodal joints. Appropriate control of the Ce/Zr ratio to 5 % results in an optimal UiO-66- NH_2 (Zr/Ce).²⁹³



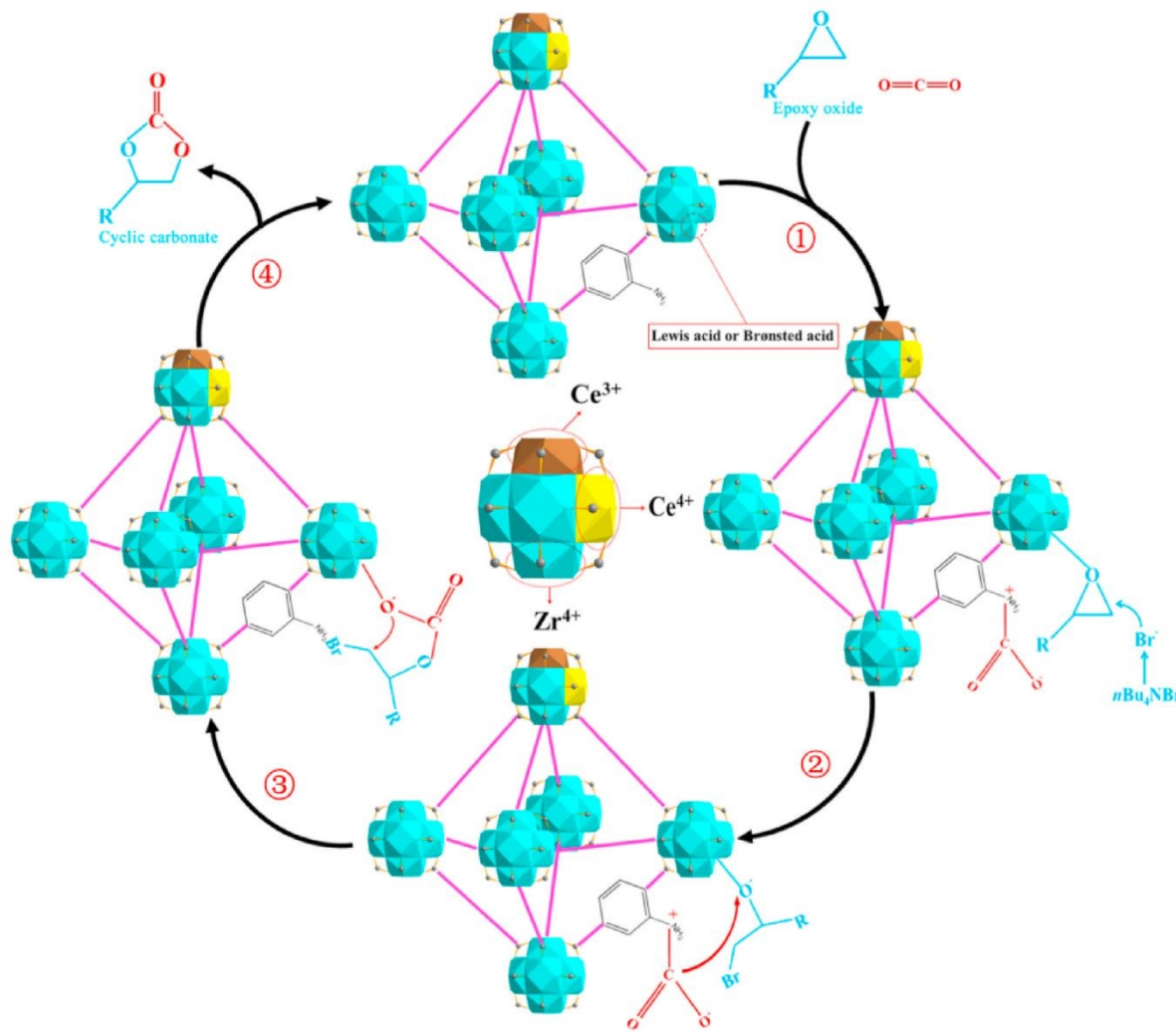


Figure 16. Proposed mechanism for the cycloaddition of CO_2 and epoxides by defective bimetallic $\text{UiO-66-NH}_2(\text{Zr/Ce})$ catalyst. 1) Through the catalyst, epoxy oxide is integrated with Lewis or Brønsted acid sites and is activated. Due to the presence of the $-\text{NH}_2$ group on MOF, CO_2 is adsorbed and polarized; 2) The nucleophilic Br^- ion attacks the β carbon atom of epoxide to form the Oxygen anion intermediate; 3) The intermediate interacts with CO_2 to create halogenated carbonate; 4) Through internal cyclization, halogenated carbonate is converted into cyclic carbonate, meanwhile the catalyst is regenerated. Reproduced with permission from ref.²⁹³ Copyright 2021 Elsevier.

Zr-MMOFs have also found applications as photocatalysts and for adsorption.²⁹⁹⁻³⁰² Theoretical modeling of crystal orbitals in some Zr MOFs , however, indicates that the overlap between the empty Zr^{4+} 4d atomic orbitals and the π^* aromatic orbitals of the ligand is very poor, hampering an efficient photoinduced electron transfer between the electronic excited state of the linker to the metal node. Inserting additional metals in the structure Zr-MMOFs can aid a better



overlapping between these two orbitals, resulting in increased photocatalytic activity. This is apparently the reason for the higher photocatalytic activity observed upon insertion of Ti in UiO-66(Zr). The 3d orbital of Ti is larger in size and higher in energy than the smaller 4d orbital of Zr, therefore, it is better suited to overlap with the terephthalate linker in its excited state.³⁰³ Doping Zr with other metal ions can also lead to the enrichment of these metals on the outer surface, which can be correlated to better CO₂ adsorption and to the enhanced photocatalytic activity for CO₂ reduction. For instance, MIL-173(Zr/Ti), having 5,10,15,20-tetrakis(3,4,5-trihydroxyphenyl)porphyrin as a linker with 40 % of Ti produces 381 and 145 $\mu\text{mol g}^{-1}$ for H₂ and O₂, respectively, in an overall water splitting reaction that is higher than the single metal MIL-173(Zr) photocatalyst. The better photocatalytic activity of the mixed metal MIL-173(Zr/Ti) can be attributed to the **i**) porphyrin linker, which acts as a natural light harvester having a high absorption in the visible region. **ii**) Ti 3d orbitals having a closer energy to the oxygen orbitals than Zr 4d orbitals, therefore they have better overlap to produce a crystalline orbital, **iii**) decrease of the band gap, and **iv**) higher efficiency of the photoinduced LMCT elementary step.²⁹⁹

In total, Zr-MMOFs can be beneficial for diverse applications. Applying Zr in nodal positions with various metals, including Ti, Ce, or even Zn, can be focused more in the future for catalytic transformations and photocatalytic reactions, including CO₂ hydrogenation or reduction. In the case of sensing applications, Zr-MMOFs are less investigated, but their synergistic effect can be explored with lanthanides. Due to the high porosity and stability that some of the Zr-MOFs can induce, indications can lead to their multi-metallic structure, especially with lanthanides in sensing applications. Although in electrocatalysis and energy storage, Zr-MOFs can provide higher stability, but their non-electroactive intrinsic features can hamper their vast usage in the mentioned applications. Therefore, using the synergistic effect between Zr and Ni, Fe, Co, or even Mn can lead to enhancing their capability toward energy conversion and storage. In that case, the indication can lead us to believe that Zr-MMOFs with electro-active metal introductions cannot only possess high stability but also provide higher activity toward energy applications, including batteries, supercapacitors, and water-splitting. But structural issues can also hamper this goal; therefore, optimizing the content of each metal can be vital.

Table 4. Represent reported Zr-MMOFs or derived materials in diverse applications, with their efficiency in specific applications.



Zr-MMOF	Other Metals	Applications	Efficiency	Ref.
10Fe:90Ni@Zr-BTB ^a	Ni/Fe	Electrocatalyst/ OER	C.d: 10/ O.v: 380/ T.f: 72	292
MIL-173(Zr/Ti)-40	Ti	Photocatalyst/ Water splitting	381 and 145 $\mu\text{mol g}^{-1}$ for H ₂ and O ₂ production/ 35°C/ 22h/ reuse: 3 cycles	299
ZrCeTi-UiO-66-NH ₂	Ti/Ce	Photocatalyst/ Dye degradation	38%	304
UiO-66 (Zr/Ti)	Ti	Catalyst/ PET polycondensation	E _a : 22.37	47
UiO66-NH ₂ (Zr/Ce)	Ce	Catalyst/ Synthesis of propylene carbonate	94%/ 5% Ce/ nBu ₄ NBr/ 100°C/ 4h/ selectivity: 98%/ reuse: 5 cycle	293
Zr-CPB-Cu	Cu	Catalyst/ Carboxylation of styrene	97%/ TBHP/ nBu ₄ NBr/ 80°C/ 12h/ selectivity: 95%/ reuse: 6 cycles	305
MOF-808-Zn	Zn	Catalyst/ CO ₂ Hydrogenation	190.7 $\text{mg}_{\text{MeOH}} \text{g}_{\text{Zn}}^{-1} \text{h}^{-1}$ / 250°C/ selectivity: 99%	298
Ni-Ce-Zr MOF ^b	Ni/Ce	Catalyst/ Reduction of MB	99.77%/ reuse: 4 cycles	306

C.d: current density based on A g⁻¹ or mA cm⁻² for energy applications/ O.v: overpotential based on mV/ T.f: Tafel slope based on mV dec⁻¹/ C.v: cell voltage based on V/ O.p: onset potential based on V/ in the most research capacity and S.p (specific capacitance) is based on F/g, C/g, and mAh g⁻¹/ E.d: energy density based on Wh kg⁻¹/ P.d: power density based on W kg⁻¹/ all percentage in photocatalyst or catalyst represent yield, conversion or any efficiency of MMOFs which for further details can see the references/ bandgap based on eV/ apparent quantum efficiency (AQE)/ photocurrent density (pd) based on $\mu\text{A cm}^{-2}$ / RT: room temperature/ TOF: turn over frequency/ TON: turn over number/ E_a: Energy activation based on kJ mol⁻¹/ for further details can see the references. CPB: 1,2,3,4,5,6-hexakis(4-carboxyphenyl)-benzene.

^a BTB: 1,3,5-tris(4-carboxylatephenyl)benzene; ^b BDC as organic linker

8. Zinc-based MMOFs

Zn is one of the transition metal elements that is highly biocompatible with the human body and can also act as an antibacterial and anti-inflammatory agent, as well as possess medicinal properties. Zinc is a relatively inexpensive element that can be used as a substitute for more costly elements in the medical field, such as silver.^{307, 308} The Zn²⁺ ion is a vital component of the human body, fulfilling a multitude of essential functions. Zinc-based MOFs are employed in a multitude of fields, including medicine, sensing, and other areas. The several applications of Zn-MOFs in medicinal chemistry are due to the antibacterial properties of Zn²⁺, as exemplified by TMU-3.³⁰⁹ Such MOFs can provide a stable and long-lasting antibacterial effect by gradually releasing Zn²⁺ as an antibacterial agent. Zn-based MOFs possess the capacity to function as chemical sensors due



to the luminescent properties of Zn complexes. Zn^{2+} , having a d^{10} electronic configuration with full d orbital shells, is a suitable transition metal condition for the purpose of building a fluorescent probe. This phenomenon requires the placement of the desired ligand within the MOF structure, but also the incorporation of another metal in conjunction with Zn has been reported as an appropriate strategy for fluorescent sensing and detection purposes.³¹⁰⁻³¹² Consequently, the incorporation of additional metals into the composition of Zn-based MOFs has the potential to yield diverse applications with enhanced performance, a subject that will be elaborated upon subsequently.

Zn-MMOFs exhibit novel properties and enhanced performance relative to their monometallic counterpart in medicine, as well as environmental pollutants adsorption and removal applications.³¹³⁻³¹⁵ For example, Lin Wang and colleagues employed Mn-ZIF-8 to accelerate the healing of infected wounds. The incorporation of manganese ions was found to influence the activity of immune cells (macrophages and neutrophils) and inflammatory cells by modulating the surrounding oxidation-reduction environment. Manganese nanoenzymes have the potential to perform the same functions as superoxide dismutase (SOD), glutathione peroxidase (GPx), and catalase (CAT). The final inhibitory effect on inflammation is exerted by copper, iron, and zinc. Zn in Mn-ZIF-8 was found to exhibit antibacterial activity, effectively destroying bacteria associated with infected wounds. Mn present in this MMOF is responsible for reducing inflammation, and the overall result is better wound healing through its SOD activity. Furthermore, the simultaneous presence of Mn^{2+}/Mn^{4+} in ZIF-8 frameworks enables the scavenging of excessive reactive oxygen species (ROS). It was clearly proven that bimetallic Mn-ZIF-8 exhibits an enhanced performance relative to its monometallic counterparts. The incorporation of 20% Mn into the ZIF-8 structure improves its bactericidal efficacy approximately two-fold with respect to ZIF-8, thereby substantiating its role as a key contributor. The combination of the two metals results in a synergistic effect that enhances the performance of Mn-ZIF-8. Figure 17 illustrates the synthesis of bimetallic Mn-ZIF-8 and its action mechanism, accelerating the healing of infected wounds.³¹³



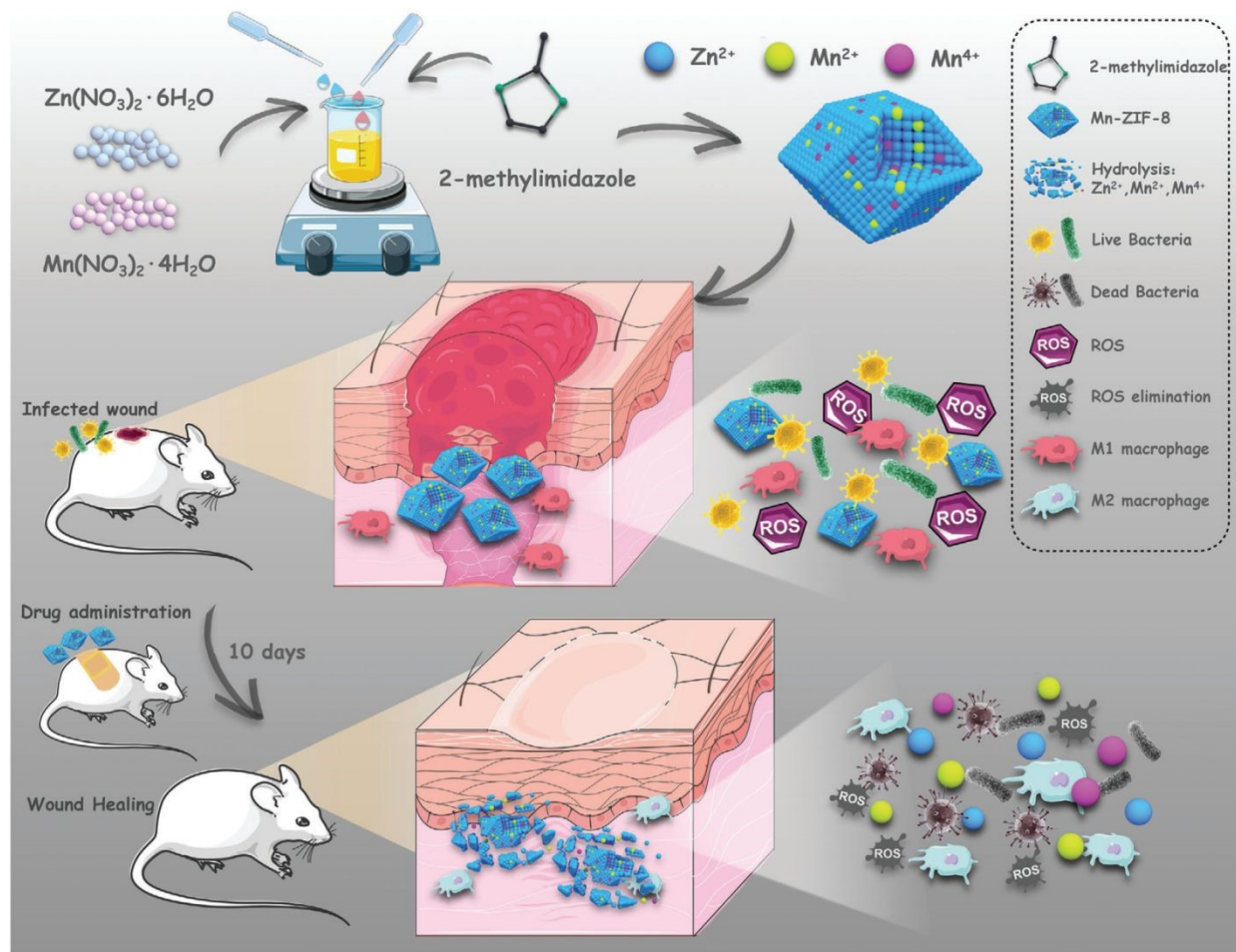


Figure 17. Synthesis of bimetallic Mn-ZIF-98 and its healing mechanism on infected wounds.

Reproduced with permission from ref.³¹³ Copyright 2021 Wiley.

Compared to MMOFs based on Ni, Co, and Fe, the number of reports exploring Zn-MMOFs as electrocatalysts is much less, but from the existing literature, it can be concluded that the incorporation of Zn ions into the MMOF structure can assist the electrocatalytic activity of the resulting MMOF. Thus, typically Zn/M MOFs exhibit lower charge transfer resistance and higher electrical conductivity. Due to its d^{10} electronic configuration in its orbital, Zn^{2+} ions can shuttle electrons to other metal ions with open d orbitals in their valence shell and stabilize the structure in the alkaline environment. As an example, Zn adjacent to other electronegative metal ions was found to increase NH_3 yield and higher electrocatalytic NRR activity. In one example of application of Zn-based bimetallic MOFs for OER, the performance of pillared MnZn-MUM-1 ($Zn_2(\mu_4\text{-odba})_2(\mu\text{-bpdh})_n \cdot nDMF$; odba: 4,4'-oxydibenzoinic acid and bpdh: 2,5-bis(4-pyridyl)-3,4-diaza-2,4-hexadiene) grown on NF having various ratios of Mn and Zn was studied.³¹⁶ It was found



that $\text{Mn}_{0.5}\text{Zn}_{0.5}$ -MUM-1 exhibits excellent OER performance compared to other counterparts, measuring an overpotential of 253 mV and a Tafel slope of 73 mV dec^{-1} at a current density of 10 mA cm^{-2} , and high C_{dl} proficiency of 9.2 mF cm^{-2} . These values indicate that $\text{Mn}_{0.5}\text{Zn}_{0.5}$ -MUM-1 exhibits excellent OER activity and the chronoamperometric measurements shown in Figure 18 indicate that this material also has great stability after 6000 cycles. It has been proposed that the reason behind the better performance of ZnMn-MMOF is related to the **i**) adjustable Zn/Mn ratio and their integration with NF, **ii**) porosity and open internal channel of MOF, **iii**) synergistic effect between the two metal ions with Mn acting as an active site for electrochemical process, and **iv**) easy penetration of electrolyte ions into the catalyst for enhancing charge transport.³¹⁶ In another study of Zn-MMOF as electrocatalysts, UOR activity of bimetallic $\text{Zn}_{0.33}\text{V}_{0.66}$ -MOF [$\text{Zn}_6(\text{IDC})_4(\text{OH})_2(\text{Hprz})_2$]_{*n*} (IDC imidazole-4,5-dicarboxylate, and Hprz: piperazine) grown on NF was investigated, reaching a current density of 50 mA cm^{-2} at a potential of 1.42 V (vs RHE) and measuring a Tafel slope of 122 mV dec^{-1} . Increasing the V percentage potentially enhances UOR activity up to an optimal ratio of 0.66 due to the alteration of the crystalline structure and the positive synergistic effect played by Zn over the active centers of UOR.⁶⁷ Beyond electrocatalysis, there are a few examples of the influence of Zn in MMOFs for energy storage systems. In these systems, the proposed role of Zn is similar in electrocatalysis, enhancing charge transport and increasing electrical conductivity. Among the examples in the use of Zn-MMOFs to build supercapacitors, the synthesized NiCoZn-BDC-MOF and NiCoZn-BTC-MOF were assembled in symmetric charge storage devices. Among them, BDC-MOF exhibits an energy storage performance of 95.22 F g^{-1} , this good value being attributed to the synergistic effect among the metals and also their pseudocapacitive behavior.³¹⁷ Also revealed that controlling of Mg/Zn ratio in Zn-MMOFs can lead to the removal of MgO nanoparticles contributes to the creation of a micro-pore structure, effectively augmenting specific capacitance which these types of materials can be explored more in the near future.³¹⁸ In one report on the MMOF derivative for developing innovative battery devices, trimetallic MOF MnZnNi-BDC was pyrolyzed to obtain the bimetallic Ni-MnO/PC (PC: porous carbon) derived material, in which Zn sublimed during the process and Ni-doped MnO.²¹⁰ Ni-MnO/PC was used as the cathode in an aqueous Zn-ion battery, achieving a discharge capacity of 349 mAh g^{-1} at a current density of 100 mA g^{-1} with ultra-long stability. Even operating at a current density of 3000 mA g^{-1} , the synthesized bimetallic MOF-derived



material retains 91.1 % of its initial capacity in 6000 cycles. Mechanistic studies indicate that Zn storage on MNi-MnO/PC occurs through co-intercalation of H^+ and Zn^{2+} .²¹⁰

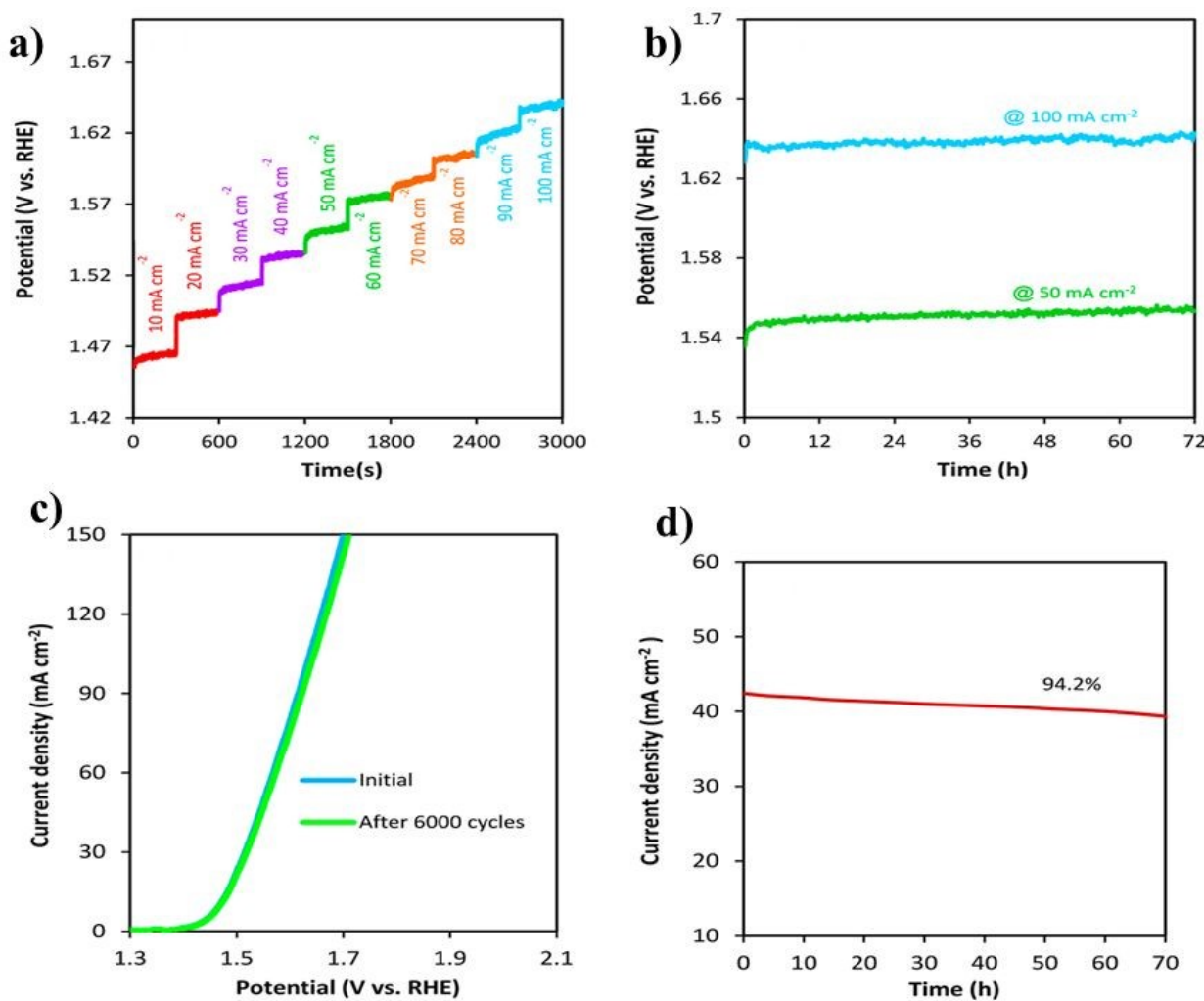


Figure 18. a) and b) Chronopotentiometric plots for $Mn_{0.5}Zn_{0.5}$ -MUM-1 at the indicated current density values; c) LSV curves for $Mn_{0.5}Zn_{0.5}$ -MUM-1; and d) chronopotentiometry curve measured at 1.53 V vs RHE for $Mn_{0.5}Zn_{0.5}$ -MUM-1. Reproduced with permission from ref.³¹⁶ Copyright 2022 American Chemical Society.

Regarding the use of Zn-MMOFs in thermal catalysis, it has been reported that the combination of heavy metal ions with Zn into the MOF structure increases accessibility to the heavy metal active sites by the porosity of the MOF, while the different affinity to ligands of Zn and heavy metals can serve to regulate the resulting catalytic activity. Thus, it is known that Zn-MOFs cannot activate oxygen molecules, but the incorporation of a heavy metal can introduce this catalytic activity, thereby resulting in a catalyst with interesting aerobic oxidation activity. In



contrast to oxygen activation, Zn can activate H₂ and control hydrogenation selectivity. One well-known case is the selective CO₂ hydrogenation to methanol, in which the combination of Cu and Zn is necessary to drive methanol formation. In a realization of this concept in Zn-MMOFs a bimetallic MOF-74(Zn) (2,5-dihydroxyterephthalate as linker) was prepared by mechanochemical synthesis. Cu was incorporated subsequently, taking advantage of the dual coordination sites of the linker, either at the carboxylate sites or the phenolic hydroxyl groups Zn-based MOFs. Generation of defects by further mechanochemical treatment of desolvated samples results in an amorphous, low surface area and non-porous a-ZnCu-MOF-74 that presents a better catalytic activity for CO₂ reduction and selectivity toward methanol compared to inactive monometallic Cu-MOF-74 and crystalline ZnCu-MOF-74. The reasons behind the better catalytic activity and selectivity of the catalyst are related to **i**) Zn increases the binding energy of the reaction intermediates decreasing activation energy and providing more attainable active sites, **ii**) the incorporation of defect sites in the MOF increases the population of more active sites, and **iii**) the amorphization reduces the surface area, but it also decreases the particle sizes and alters the coordination environment of the nodes in MOF-74, therefore augmenting the methanol productivity.³¹⁹ In one of these examples related to catalysis, bimetallic [Cd₂Zn-(DPTTZ)_{0.5}(OBA)₃(H₂O)(HCOOH)] (DPTTZ = 2,5-di(4-pyridyl)thiazolo[5,4-*d*]thiazole and OBA = 4,4'-oxybis(benzoic acid) was found to exhibit good performance as catalyst in cyclooctene epoxidation.³²⁰ Good yields were obtained with this CdZn-MMOF after optimization in the material of various parameters including: **i**) the reaction temperature, since higher temperatures facilitate to overcoming the activation barrier of the rate-limiting step, **ii**) the nature of the oxidizing reagent, since *tert*-butylhydroperoxide (TBHP) was found more convenient than H₂O₂ in aqueous medium, **iii**) catalyst amount, since higher amount leads to higher yields, **iv**) reaction time, with optimum times avoiding overoxidation and epoxide decomposition, **v**) solvent, epoxidation performing better using CCl₄ due to its low coordination capability and low dielectric constant which can impact diffusion to the active centers. complexing solvents diminishing the epoxide yield by inhibiting the coordination environment around the metal center, and **vi**) the presence of co-catalyst and Lewis acid, since the presence of Al³⁺ ions as Lewis acid site leads us to enhanced reactivity.³²⁰ In one study, a Pb, Zn-based bimetallic MOF, namely PbZn_{0.5}L(H₂O)]_{0.5}NMP H₂O}_n (L: 1H-tetrazol-5-yl)terephthalic acid, NMP: N-methyl-2-pyrrolidone) was synthesized for catalysis procedure.³²¹ The ligand selection, synthesis, and



resulting structure of PbZn-MMOF follows the rules of the hard-soft acid-base theory, since Pb has a preference to coordinate with the oxygen atoms of the carboxylate groups, while Zn coordination occurs through the N atoms of the tetrazole unit. In that way, while monometallic Pb or Zn with the tetrazolylterephthalate do not form porous structures, the bimetallic Pb_xZn_{1-x}-MMOF is a porous framework, therefore, corresponding to a MOF material that requires porosity as a structural property.³²¹ This PbZn-MMOF is a catalyst for the CO₂ fixation onto epoxides to form cyclic carbonates, a reaction of importance to obtain solvents and monomers.³²¹ Up to 98 % yield for CO₂ conversion was achieved for epichlorohydrin 1-butene oxides using tetra N-butylammonium bromide as a co-catalyst. In this PbZn-MMOF, Zn provides porosity in structure, the synergistic structural effect between them resulting in a highly stable porous MOF via the efficiency of CO₂ conversion up to 98%. The two possible reaction mechanisms were suggested involving either interaction of epoxide O atom with the Lewis sites of the MOF with the assistance of the bromide to the epoxide ring opening or activation of CO₂ by the MMOF.³²¹

In total, Zn-MMOFs can be used as electrocatalysts and in energy storage systems, because they can facilitate charge transfer. Therefore, the synergistic effect between Ni, Co, and Mn can be beneficial for energy applications. Due to its d¹⁰ electronic configuration in its orbital, Zn²⁺ ions can shuttle electrons to other metal ions with open d orbitals in their valence shell and stabilize the structure in the alkaline environment; therefore, cannot only be beneficial for energy applications but also can be useful for photocatalysis, catalysis, and sensing applications. Table 5 summarizes recent work on Zn-MMOFs for various applications, including key performance metrics.

Table 5. Summary of reported Zn-MMOFs or derived materials, indicating their use and data on their performance.

Zn-MMOF	Other Metals	Applications	Efficiency	Ref.
Mn _{0.5} Zn _{0.5} -MUM-1	Mn	Electrocatalyst/ OER	C.d: 10/ O.v: 253/ T.f: 73	³¹⁶
Zn _{0.33} V _{0.66} -MOF/NF ^a	V	Electrocatalyst/ UOR	C.d: 50/ O.p: 1.42/ T.f: 122	⁶⁷
NiCoZn-BDC-MOF	Ni/Co	Supercapacitor	S.p: 582.8/ C.d: 5 (3000 cycle)/ E.d: 47.59/ P.d: 1376.42/ retention: 92.44%	³¹⁷
CDZ-20	Cu	Photocatalyst/ Water splitting	H ₂ Generation rate: 13.9/ Bandgap: 4.42/ AQE: 9.08%/ P.D: 34	³²²



Cu@ZIF-8	Cu	Catalyst/ Hydrocarbon oxidation	16%/ 120°C/ O ₂ / 24h/ selectivity: 85%/ reuse: 2 cycles	323
Cu@ZIF-8	Cu	Catalyst/ Hydrogenation of Alkenes	>99%/ RT/ N ₂ H ₄ .H ₂ O/14h/ selectivity: 99%/ reuse: 3 cycles	324
NUC-51a	Ba	Catalyst/ Knoevenagel condensation reaction	97%/ 55°C/ n-Bu ₄ NBr/ 5h/ selectivity: 99%/ TON: 97.2/ TOF: 16.2/ reuse: 5 cycles	325
PtZn-MOF-74	Pt	Catalyst/ CO oxidation	E _a : 101.31/ TOF: 2.32/ reuse: 5 cycles	326
a-ZnCu-MOF-74	Cu	Catalyst/ CO ₂ reduction	E _a : 78.6/ 200°C/ selectivity: 99%	319
IUST-4	Cd	Catalyst/ Epoxidation Reaction of Olefins	99%/ TBHP/ 60°C/ 4h/ selectivity: 99%/ reuse: 5 cycles	320
PbZn_{0.5}L(H₂O)_{0.5}NMP H₂O₃_n	Pb	Catalyst/ CO ₂ conversion	98%/ TBAB/ RT	321
Zn/Ca-MOF ^b	Ca	Sensing/ Fe ³⁺ and Cr ₂ O ₇ ²⁻	detection limits: 18.8 μM for Fe ³⁺ and 29.1 μM for Cr ₂ O ₇ ²⁻	327

C.d: current density based on A g⁻¹ or mA cm⁻² for energy applications/ O.v: overpotential based on mV/ T.f: Tafel slope based on mV dec⁻¹/ C.v: cell voltage based on V/ O.p: onset potential based on V/ in the most research capacity and S.p (specific capacitance) is based on F/g, C/g, and mAh g⁻¹/ E.d: energy density based on Wh kg⁻¹/ P.d: power density based on W kg⁻¹/ all percentage in photocatalyst or catalyst represent yield, conversion or any efficiency of MMOFs which for further details can see the references/ bandgap based on eV/ apparent quantum efficiency (AQE)/ photocurrent density (pd) based on μA cm⁻²/ RT: room temperature/ TOF: turn over frequency/ TON: turn over number/ E_a: Energy activation based on kJ mol⁻¹/ for further details can see the references.

^a linear N-donor piperazine (Hprz), rigid planar imidazole-4,5-dicarboxylate (IDC³⁻) as linkers; ^b 5,5'-(propanen-1,3-diyl)-bis(oxy)diisophthalic acid as linker

9. Lanthanide-based MMOFs

In recent years, multi-metal MOFs based on lanthanides (La-MMOFs) have been the subject of considerable scientific interest especially in sensing applications.^{328, 329} However, the use of La-MMOFs as catalysts is considerably less explored.^{330, 331}

Lanthanides have partially filled 4f orbital, which makes possible many accessible electronic levels leading to interesting optical properties. Except for Lu³⁺(4f¹⁴) and La³⁺ (4f⁰), all lanthanide ions exhibit luminescence emission, some in the visible region and some in the near-infrared region. The electronic transitions observed in lanthanide-based polynuclear MOFs, including charge transfer (such as metal-to-metal charge transfer (MMCT), metal-to-ligand charge



transfer (MLCT), and ligand-to-metal charge transfer (LMCT) charge transfer) and 4f-5d transitions, can result in atomic emission from the lanthanide ions.³³²

The unique behavior of some luminescent MOFs to respond to specific external stimuli by modifying the emission intensity or turning the emission off and on has attracted the attention of the scientific community.³³³ La-MMOFs have demonstrated efficacy in sensing a range of analytes, including small molecules, ionic species, pH, explosives, and temperature, due to these optical properties of lanthanides. Moreover, the intrinsic chemical and structural attributes of MOFs containing lanthanides render them valuable in bioassays. Illustrative examples of the use of La-MMOFs for sensing are described below.³³²

The sensing of hydrogen peroxide, as one ROS in living organisms, is significant, for example, to gain a deeper understanding of the mechanism of activity enhancement and the early detection of plant health. In this context, Kun Wang et al. reported a bimetallic- Ce/Zr organic framework (Ce/Zr-MOF) that demonstrated enhanced performance in mimicking enzymatic peroxidase activity. The peroxidase (POD) activity of the bimetallic-organic Ce/Zr framework was found to be higher than those of the corresponding monometallic MOFs. In addition to exhibiting sensing properties, this Ce/Zr metal framework also displays catalytic characteristics. In the catalytic cycle, the Ce and Zr redox cycles operate synergistically, enhancing the activity of POD and facilitating the highly sensitive detection of hydrogen peroxide. The biosensor can be quantitative, being capable of providing information regarding the concentration of hydrogen peroxide. The color change is visually discernible to the naked eye, obviating the need for expert interpretation and rendering the process highly accessible. The enhanced POD-like activity mainly relied on the incorporation of Ce, which enhanced the conductivity and electron transport capability of Ce/Zr-MOF and boosted the production of •OH.³³⁴

Mercury ions are highly toxic, and their detection and quantification are crucial for human health and the quality of water, food, and medicine. Mercury detection has attracted the attention of numerous scientists, who have sought to develop more efficient methods for measuring Hg^{2+} ions. In response to this need, Lian Xia and colleagues synthesized a bimetallic La-MMOF using Ce^{4+} and Eu^{3+} and a 5-boronoisophthalic acid (5-bop) ligand for Hg^{2+} ion sensing. The LMCT in Ce^{4+} is more facile due to the lower energy of its 4f empty band in comparison to the Eu^{3+} ion. Consequently, Ce^{4+} exhibits a greater capacity to absorb energy than Eu^{3+} . For this reason, Ce^{4+}



exhibits a more extensive and robust fluorescent emission than Eu^{3+} . Upon exposure to Hg^{2+} , the bimetallic La-MMOF undergoes an LMCT, whereby the boric acid group is replaced by a mercury ion. This process considerably disturbs the emission of the EuCe-MMOF, resulting in a decrease in the fluorescence intensity of Eu^{3+} and an increase in the fluorescence intensity of Ce^{4+} . This behavior makes the bimetallic CeEu-MOF capable of detecting Hg^{2+} with high selectivity. The employment of this bimetallic MMOF instead of the monometallic analogs results in the improved detection of Hg^{2+} with a lower detection limit and higher selectivity (Figure 19).³²⁸

In another report on the use as a sensor of a bimetallic La-MMOF, Eu/Zr-UiO-66 was synthesized to quantify volatile organic compounds (VOCs), with a particular focus on cyclohexanone and styrene. The BDC ligand in this MOF exhibits a strong emission effect due to the π -system in its aromatic rings, which is enhanced by the addition of Eu^{3+} . The bimetallic MOF displays a higher fluorescence intensity than UiO-66, which can be attributed to the "antenna effect" and the strongest $^5\text{D}_0 \rightarrow ^7\text{F}_2$ transition. In this study, the fluorescence intensity of Eu/Zr-UiO-66 was investigated in the presence of different VOCs. It was observed that the fluorescence intensity of the MOF increased by 54 % when exposed to cyclohexane and decreased by 76 % when exposed to styrene. However, in the presence of other VOCs, no discernible change was observed. Styrene as VOC displays greater sensitivity and larger fluorescence change compared to aliphatic compounds. This higher response for styrene can be attributed to the effect of the aromatic ring and its p electron cloud, which should interact better with the metal ions and the MOF terephthalate linker. As the UV absorption spectrum of cyclohexanone and styrene overlaps with the emission spectrum of Eu/Zr-UiO-66, exposure of this compound to cyclohexanone and styrene results in a decrease in emission intensity and cessation of emission due to the fluorescence resonance mechanism and energy transfer, in which light emitted by the terephthalate linker is absorbed by the analytes and not detectable. This is attributable to the synergistic effect of the two metals and the superior performance of a bimetallic MOF in comparison to a monometallic one.³²⁹ Besides fluorescence and VOC sensing ability, other collateral effects of the incorporation of Eu^{3+} in the MOF structure are a more uniform pore distribution and a larger surface area in Eu/Zr-UiO-66 (1:9) compared to a monometallic Zr-UiO-66.³²⁹

In a synthesis of La-MMOF reported by de Azambuja, Parac-Vogt, and co-workers, Zr/Ce-MOF-808 was obtained, which can function as a peptidase enzyme. The role of Ce^{4+} , in this case,



is of particular importance to enhance the enzymatic activity of MOF-808, as Ce^{4+} is a more efficient center for peptide bond hydrolysis than Zr^{4+} , which explains the enhanced performance of the bimetallic MOF in comparison to the monometallic.³³⁵ Furthermore, Ce^{4+} increases the durability of this MMOF in an aqueous environment. This is a crucial point regarding the catalytic activity as demonstrated in this and other examples.

In another instance, Li, Yang, and coworkers reported a bimetallic La/Ca-BDC MOF for the application of phosphate removal in water. By incorporating Ca into a La-BDC MOF, the phosphate removal capacity was significantly increased. In addition, this bimetallic MOF works in a wide range of pH from 3 to 9, which indicates the high performance of this bimetallic MOF in comparison to La-BDC, particularly under basic pH values.³³⁶

As previously stated, the measurement of H_2O_2 in biological fluids is important because this substance, despite its low toxicity, has the potential to generate ROS responsible for damaging carbohydrates, proteins, and lipids. It has been proposed that hydrogen peroxide formed as a byproduct of aerobic metabolism can accumulate in the body causing oxidative stress that may result in cell malfunction. Consequently, scientists have devised various methods for measuring this substance. In this context, it is known that certain metal oxides, including TiO_2 , MnO_2 , Co_3O_4 , CeO_2 , and Fe_2O_3 , can be used for the detection of hydrogen peroxide. Among these metal oxides, CeO_2 has garnered particular interest from scientists in the fields of medicine and biology for its ability to decompose hydrogen peroxide mitigating the negative effects of free ROS and its effective catalytic activity. In this regard, Guo et al. have reported the synthesis of two metal oxides derived from bimetallic rare earth homotypic metals to measure hydrogen peroxide, homotypic meaning that the Ce and the second rare earth metals are similar in properties and exchangeable³³⁷. Two issues were taken into consideration during the development of this sensor. First, the researchers employed two homotypic metals to ascertain the potential for a synergistic effect, in addition to the similar properties of the homotypic elements. As is the most general case when substitution of two elements with similar atomic mass, oxidation state, and radius, this substitution results in the formation of a highly stable framework. The utilization of porous MOF precursor facilitates the generation of large surface area and precise channel interconnections, which finally leads to an enhanced sensing efficiency.³³⁷ Accordingly, MMOFs were employed as a precursor to prepare homotypic porous bimetallic oxides. To this end, the $\text{Ce}_{0.9}\text{Tb}_{0.1}$ -MOF (BTC as linker)



crystal was initially synthesized, its XRD peaks agreeing with those of Ce-MOF. Upon heating the material to 400 °C in air, the Ce-MMOF underwent decomposition, resulting in the formation of the $\text{Ce}_{0.9}\text{Tb}_{0.1}\text{O}_y$ crystal through the MOF-derived process. XRD pattern of the obtained mixed oxide is consistent with the crystallography of CeO_2 . The resulting solid oxide exhibits some of the characteristics of $\text{Ce}_{0.9}\text{Tb}_{0.1}$ -MOF, particularly its porosity. The formation mechanism of the final micron-sized porous $\text{Ce}_{0.9}\text{Tb}_{0.1}\text{O}_y$ is proposed to occur in two steps, in which first $\text{Ce}_{0.9}\text{Tb}_{0.1}$ -MOF decomposes, forming bimetallic oxide nanoparticles that, in a second step, undergo sintering of the bimetallic nanoparticles and growth, giving rise to the micron-sized crystals but retaining a considerable degree of porosity. Compared to CeO_2 , the bimetallic oxide sample exhibits a larger pore volume and surface area, thereby providing a higher density of accessible catalytic sites. XPS was used to investigate the surface composition and oxidation states of both CeO_2 and $\text{Ce}_{0.9}\text{Tb}_{0.1}\text{O}_y$ samples. The comparison of these two spectra shows that the relative O_y percentage on the surface of $\text{Ce}_{0.9}\text{Tb}_{0.1}\text{O}_y$ is higher than that of the monometallic crystal. Ce^{3+} ion plays a role in electron transfer rate. Ce^{3+} content in $\text{Ce}_{0.9}\text{Tb}_{0.1}\text{O}_y$ is higher than in CeO_2 . This indicates that by incorporating Tb in the crystal structure it is possible to increase the population of Ce^{3+} , the result being a higher sensing ability in measuring H_2O_2 for $\text{Ce}_{0.9}\text{Tb}_{0.1}\text{O}_y$ in comparison to CeO_2 (Figure 20).³³⁷ All reported sensing and other applications in La-MMOFs are summarized in Table 6.



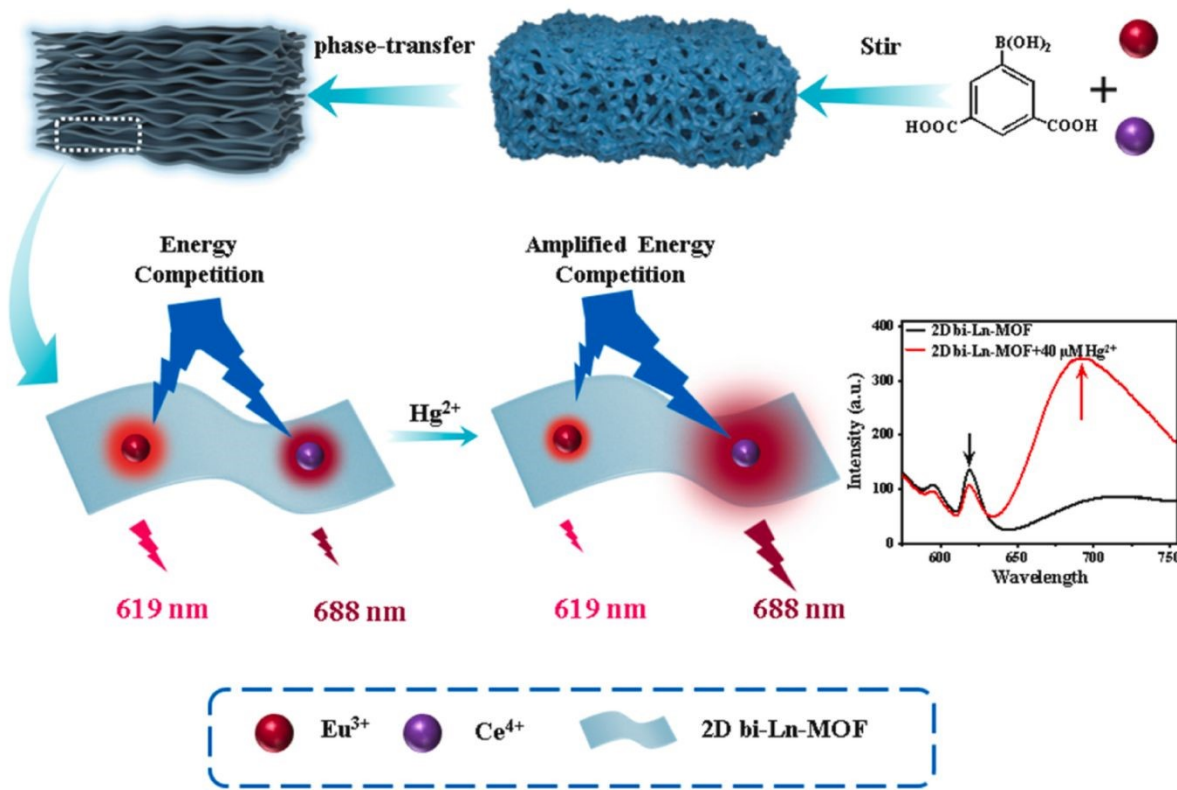
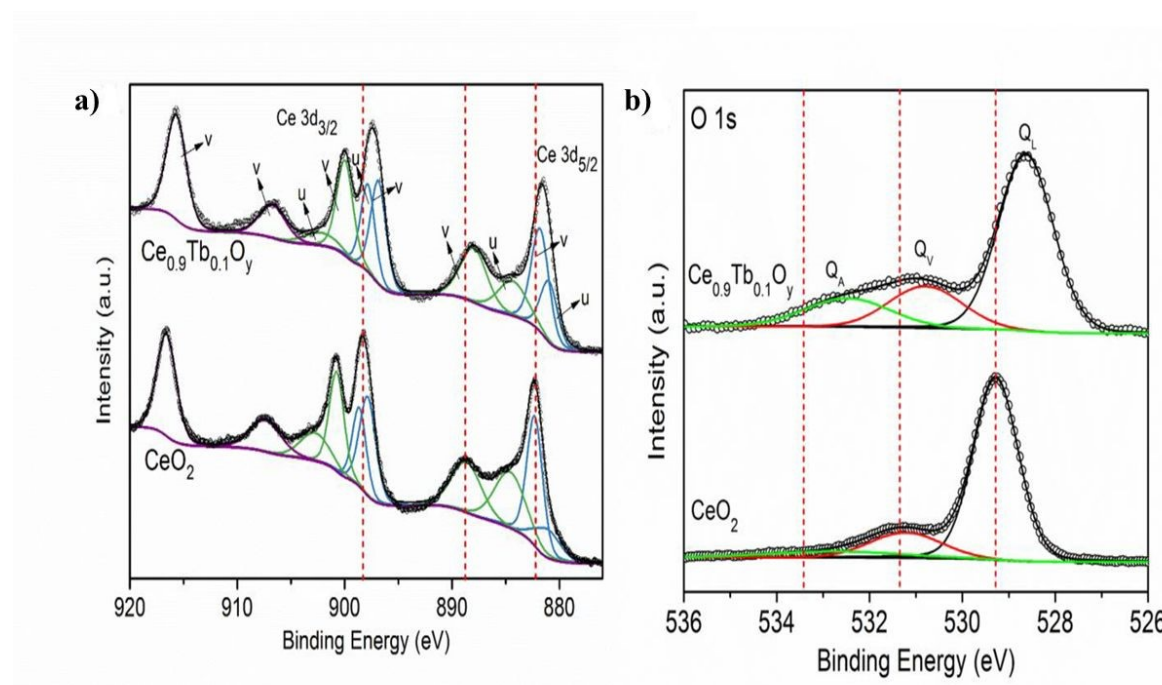
Figure 19. Synthesis of bimetallic La-MMOF and its application in the detection of Hg²⁺ ions.Reproduced with permission from ref.³²⁸ Copyright 2024 Elsevier.

Figure 20. XPS data of a) Ce 3d and b) O 1s for CeO_2 and porous $\text{Ce}_{0.9}\text{Tb}_{0.1}\text{Oy}$ obtained by thermal treatment of the corresponding MMOF. Reproduced with permission from ref.³³⁷ Copyright 2019 Elsevier.

La-MMOFs have been much less investigated for applications related to electrocatalysis, catalysis, and removal.^{330, 338, 339} For La-based bimetallic MOF used as catalysts, an example worth mentioning is bimetallic Ce-UiO-66-Co, which exhibits lower activation energy for the chemoselective methane oxidation to methanol by H_2O_2 under high pressure than the Zr-UiO-66-Co counterpart, resulting in a better catalytic performance for the former.⁷⁸ This better performance of Ce-UiO-66-Co was attributed to: **i**) the higher activity and selectivity for Ce compared to when Zr is in the structure, **ii**) the higher electron deficiency on Co due to the electronegativity of the Ce^{4+} -oxo cluster node that renders Co more similar to a Co^{3+} species, thereby enhancing C-H activation of methane via σ -bond metathesis, and **iii**) a certain increase in pore size for the Ce-UiO⁷⁸. Mechanistic studies on bimetallic Ce-MOF have led to the proposal that coordination of H_2O_2 to Co ion, followed by removal of H_2O , results in the formation of a Co-OOH intermediate. A scheme of the proposed mechanism of methane activation by Ce-UiO-66-Co is depicted in Figure 21. Subsequent steps involve the formation of a $\text{CH}_3\text{-O}$ bond by σ -bond metathesis between the C-H bond of methane and the Co-O bond of Co-OOH. Finally, CH_3OH is released by the replacement of the Ce-OCH₃ bond by Co-OH, closing the catalytic cycle.⁷⁸



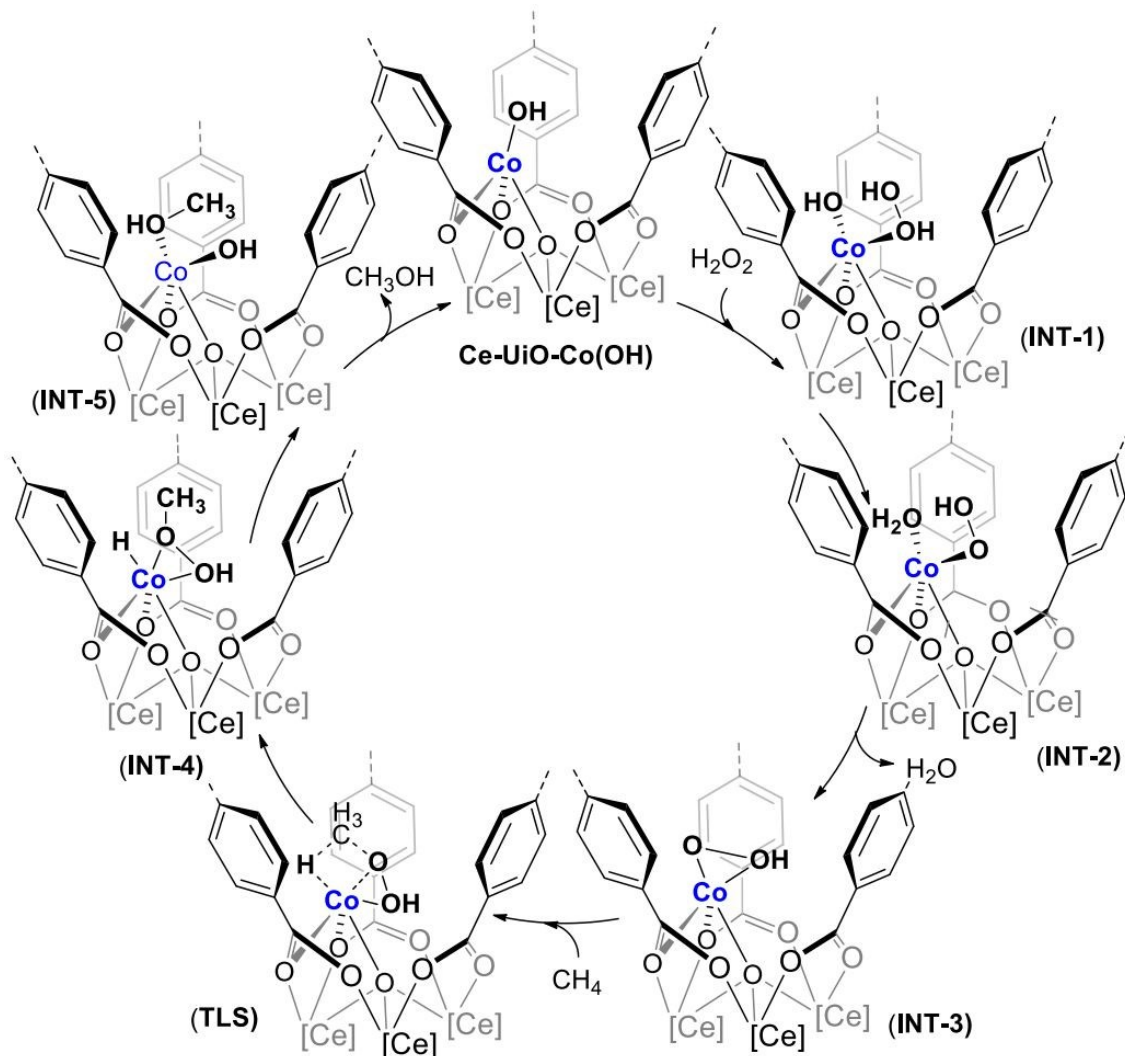


Figure 21. Proposed mechanism for the activation of methane by Ce-UiO-Co MOF H_2O_2 in bimetallic. Reproduced with permission from ref.⁷⁸ Copyright 2022 American Chemical Society.

Lanthanide incorporation is the most frequently employed strategy in MMOFs and derivatives for application in sensing, due to the remarkable atomic fluorescence properties of these metals. From the existing literature, it appears that co-incorporation of more than one lanthanide element is generally favorable and can increase sensing efficiency even more. Therefore, the most common usage of these materials can be pertinent to sensing. However, besides their less investigated capability in energy applications, findings indicate that they can have intrinsic activity in water-splitting, especially doping or incorporation of Ce into the structure of MMOFs, which can augment electrocatalytic activity and serve to introduce structural defects, which should increase the population of active sites, thereby boosting the catalytic performance

with respect to the parent monometallic MOF. In the future, not only can focus on sensing properties of La-MMOFs, but also can be demanding that explores the role of lanthanides in the electro-/photocatalytic procedures, catalytic organic transformations, and removal.

Table 6. Summary of reports on La-MMOFs or derived materials for diverse applications with some metrics regarding their efficiency.

La-MMOFs	Other Metals	Applications	Efficiency	Ref.
Ce-MOF@Pt ^a	Pt	Electrocatalyst/ Water splitting	C.d: OER and HER: 10/ O.v: OER: 340 and HER: 208/ T.f: OER:47.9 and HER: 188.1	330
Pd/LaQS	Pd	Catalyst/ Hydrogenation of Furfural	>99%/ 30min/ selectivity: 99%/ reuse: 4 cycles	331
Ce-UiO-Co	Co	Catalyst/ Methane Oxidation to Methanol	2166 mmol g _{cat-1} / H ₂ O ₂ / 80°C/ selectivity: 99%/ TON: 3250	78
NUC-56a	In	Catalyst/ Knoevenagel condensation reaction	96%/ 65°C/ n-Bu ₄ NBr/ 7h/ TON: 960/ TOF: 137/ reuse: 10 cycles	340
Tb-Ce-MOFs ^b	-	Sensing/ Phosphate ion	LOD: 28 nM/ Metrics: water	341
Eu _{0.048} Tb _{0.052} Gd _{0.9} -CPBA	-	Sensing/ Glyphosate	LOD: 0.47 μM/ Metrics: water	342
Tb _{0.4} /Eu _{0.6} - BTC	-	Sensing/ Dipicolinic acid	LOD: 4.9 nM/ Metrics: soil and water samples	343
Cu/UiO-66	Cu	Sensing/ Chloramphenicol	LOD: 0.09 nM/ Metrics: fish	344
Tb _{0.6} Eu _{0.4} -MOF ^a	-	Sensing/ Sulfamerazine	LOD: 0.1 μM/ Metrics: fish	345
Eu _{0.05} Tb _{0.95} L ^b	-	Sensing/ Nitrofurazone	LOD: 0.013 μM	346
Eu/Zr-MOFs ^b	Zr	Sensing/ Acrylamide	LOD: 2.4×10^{-8} M/ Metrics: food	347



Eu _{0.07} Gd _{0.03} -MOF ^c	-	Sensing/ Fe ³⁺	LOD: 0.091 μM/ Metrics: water	348
Eu _{0.075} Tb _{0.925} -MOF	-	Sensing/ Fe ³⁺	LOD: 2.71×10^{-7} M to 8.72×10^{-7} M/ Metrics: water	349
Zn ₃ Eu ₂ -L ^d	Zn	Sensing/ Fe ³⁺	LOD: 16.8 μM	350
Zn/Eu-MOF	Zn	Sensing/ Ofloxacin	LOD: 0.44 μM/ Metrics: food	351
La-MOFs	-	Sensing/ F ⁻	LOD: 96 ppb/ Metrics: water	352
Eu/Tb(BTC)	-	Sensing/ Bacillus anthracis	LOD: 1087 nM	353
Tb _{0.9} Gd _{0.1} -PBA	-	Sensing/ Anthrax biomarker	LOD: 1.03 μM/ Metrics: urine and water	354
Eu _{2.2} Tb _{97.8} -TCA	-	Sensing/ Water	LOD: 0.016% v/v/ Metrics: Organic solvent	355
Eu _{0.00667} Tb _{0.99333} ^e	-	Sensing/ Temperature	-	356
Fe/Eu-MOF	Fe	Sensing/ Serum alkaline phosphatase (ALP)	LOD: 0.9 U/L	357
Eu/Zr-MOFs ^b	Zr	Sensing/ Acrylamide	LOD: 2.4×10^{-8} M	347
EuTb-MOF-1	-	Sensing/ Pb ²⁺ sulfamethoxazole (SMZ) sulfadiazine (SDZ)	LOD: 0.037 μM 0.041 μM/ Metrics: water	358
Tb _{1.7} Eu _{0.3} (BDC) ₃ (H ₂ O) ₄	-	Sensing/ dipicolinic acid (DPA)	LOD: 2 to 100 μM/ Metrics: water	359

C.d: current density based on A g⁻¹ or mA cm⁻² for energy applications/ O.v: overpotential based on mV/ T.f: Tafel slope based on mV dec⁻¹/ C.v: cell voltage based on V/ O.p: onset potential based on V/ in the most research capacity and S.p (specific capacitance) is based on F/g, C/g, and mAh g⁻¹/ E.d: energy density based on Wh kg⁻¹/ P.d: power density based on W kg⁻¹/ all percentage in photocatalyst or catalyst represent yield, conversion or any efficiency of MMOFs which for further details can see the references/ bandgap based on eV/ apparent quantum efficiency (AQE)/



photocurrent density (pd) based on $\mu\text{A cm}^{-2}$ / RT: room temperature/ TOF: turn over frequency/ TON: turn over number/ E_a : Energy activation based on kJ mol^{-1} for further details can see the references. LaQS: La-based metal-organic framework; CPBA: 3,5-bis-(3-carboxyphenoxy)benzoic acid; TCA: 4, 4', 4"-nitrilotribenzoic acid.

^a BTC as an organic linker; ^b NH₂-BDC as linker; ^c 2,3,5,6-tetrafluoroterephthalic acid (H₂tfBDC) as linker; ^d H₆TTHA: 1, 3, 5-triazine-2, 4, 6-triamine hexaacetic acid as linker; ^e H₂TDC: 2, 5-thiophenedicarboxylic acid as linker.

10. Conclusions

Having a simple procedure for synthesizing MMOFs is always beneficial for any application. Especially suitable methods are *in situ* or one-pot synthesis since they are the simplest methods, consisting of the formation of the MMOF by a mixture of all the components. Also, the use of preformed clusters can be a practical strategy with the advantage of fine control of the molar ratio of the metals prior to the formation of MMOFs, which appears to be very appropriate considering that an optimal molar ratio is usually required to achieve the highest efficiency in most applications. For energy storage applications with Ni-containing MMOFs, one of the most favorable strategies is the *in-situ* growth of the Ni-MMOF on nickel foam, since in this way, the nickel foam acts as the source of Ni and the resulting MMOF exhibits a premier electrocatalytic activity or specific capacitance impossible to reach in other synthetic methods. Similar strategies using other metal foams or metal elements are, however, still to be developed, but appear promising in view of the excellent results achieved with Ni foam. In other cases, the metallo-ligand strategy in which a preformed metal complex is used in the MMOF synthesis can be a practical route for certain specific MMOFs due to their well-defined incorporation of suitable complexes acting as linkers. Metallo-ligands in MMOFs can especially introduce some response in the materials, transferring electrons amid structure, particularly in electrocatalytic applications, frequently establishing a synergistic effect with other metals in the structure. In comparison to electrocatalysis, the use of metallo-ligands in MMOFs is much less explored in photocatalysis, for which nevertheless the reported examples already show considerable potential, and it is even less investigated in catalysis. This is somehow unexpected considering that metal complexes have very rich catalytic activity as homogeneous catalysts in a variety of reactions. Regarding MMOF-derived materials, thermal treatment causes the collapse of the crystal structure, rendering an amorphous structure, but still with high specific areas, very small particle size, and a large population of attainable active sites. Depending on the atmosphere of the thermal process and the temperature, the organic linker can completely disappear, forming an inorganic solid, like oxides,



or can be carbonized, becoming transformed into amorphous porous carbon. The loss of the crystal structure is particularly interesting for the use of the resulting derivative in electrocatalysis and as active material in supercapacitors. Post-modification methods to obtain MMOFs have been divided into the core-shell, insertion, and exchange routes, and all of them are less explored compared to the pre-modification approach and MMOF derivatization, probably due to their higher complexity. It has been found that post-synthesis incorporation of additional metals in a preformed structure can diminish its crystallinity, which can be beneficial or detrimental depending on the application. As a general comment, it seems that post-modification strategies, although having considerable potential, still require much further attention to overcome their limitations, such as complexity or high cost of precursors.

This review has described the use of MMOFs and their derivatives for applications related to electrical energy conversion and storage, catalysis, photocatalysis, and sensing. As a general summary, it can be concluded that MMOFs perform better than the corresponding monometallic MOFs due to the appearance of synergistic effects. Typically, there is an optimum molar ratio of each metal to achieve a balance between the site accessibility and crystallinity of MMOFs and composition that results in higher efficiency, abundance and affordability, and the appropriate redox potentials of the various Ni oxidation states providing efficient electroactive catalytic sites. In addition, Ni establishes synergistic effects with other metal ions, such as Fe and Co, resulting in an increase in Faradaic efficiency, including lowering overpotential, smaller Tafel slope, lesser energy barrier of the rate-determining step, lower charge resistance and increased double-layer capacitance, and higher turnover frequency. Also, for energy storage applications, Ni-MMOFs are again the most frequently reported in the literature due to the high electroactivity of Ni ions and their synergistic effect with Co and Mn, leading to a boost of the specific capacitance. In comparison to energy storage and conversion, the nature of the metals in MMOFs for catalytic applications is wider and more diverse, although the literature is at present dominated by Co, followed by Zn and Cu, as the prevalent three elements in MMOF structures. Due to the favorable accessibility of a porous structure, a larger population of defects generated almost universally by the native metal and regulation of the electronic properties of the active sites, MMOFs frequently exhibit a better catalytic performance than monometallic MOFs, achieving higher conversion and yields in the catalytic reactions. Regarding photocatalysis, MMOFs can also perform better than monometallic analogs by diminishing the bandgap, what results in an enhanced light harvesting



and regulating the d-band center to the Fermi level. The most frequently employed metals in MMOF photocatalysts are Ni and Fe, besides heavy metal ions and lanthanides. Lanthanides are by far the most used MMOFs utilized in sensing due to their atomic fluorescence. Incorporation of lanthanides into MMOFs enhances their sensing performance relative to their monometal counterparts, a phenomenon attributed to the synergistic effect between the constituent metals. Besides their use as sensors, Ce-MMOFs are also employed as catalysts and photocatalysts. In terms of other applications, such as removal of pollutants and adsorption, medicine and separation, there are already several reports showing that Fe as a second or third metal can be effective in increasing the performance of the material acting either as an active site or providing a selective coordination environment. Besides experimental measurements, further rationalization and deeper understanding of the specific role of each metal in MMOFs is still necessary in general. Also, better control of crystal engineering and a wider toolbox of possible modifications to prepare the required MMOF and derivatives at will are still wanted. Enhancing the efficiency of MMOFs by using other metal combinations can lead to optimal performance of these materials for specific applications. Using abundant elements to obtain materials with the highest activity remains a challenge in this area. Also, some drawbacks such as controlling crystalline structures of MOFs by introduction of multiple metals, providing commensurate metal salts precursors, modulation of molar ratio, and choosing appropriate content of each metal for higher efficiency, complexity of some synthesis routes, scalability, and stability in some cases can be noticed more in the future for achieving the best performance of MMOFs. Future research in this area should be focused not only on synthesizing new MMOFs with optimal molar ratios but also on providing an understanding of the specific role of each metal and the reasons for their synergy, including more in-situ analysis, analysis that evaluate alteration in electronic structure before and after operations, and theoretical simulations such as DFT.

11. Outlook and Future Prospects

The synthesis and application of MMOFs and their derivatives is a fast-growing area that has shown the unique performance of these materials as a consequence of the combination of two or more metals, but that currently encounters several limitations and bottlenecks. Further understanding of each metal's role in MMOFs and investigation of the reasons for improved efficiency is mandatory to advance the field. This could provide some guidelines for the selection



of the composition of the optimal materials for a given application. Computational modeling must assist in gaining this knowledge and in predicting optimal materials. Novel, general synthesis strategies that could allow the obtainment of the wanted MMOF with a good balance between affordability and performance are also needed for future development of the area. Although many studies have shown improved performance in diverse fields of MMOFs compared to single-metal MOFs, the understanding of the role of metals for each in application from catalysis, energy-related applications, sensing, and pollutant adsorption is still limited. Therefore, investigating the role of metals and the origin of the synergistic effect derived from the combination of transition metals is still necessary and will be extremely important to orient future research toward further performance optimization of MMOFs and derived materials. Tailoring band structure in photocatalysis, a change in the stability of MOFs, buttresses catalytic site diversity and activity, which can be achieved by using MMOFs. Recent breakthroughs of MMOFs and their derivation, which can be explored further in the future, can be related to the: **i)** MMOFs and their derivatives are less investigated in the applications such as NRR, CO₂RR, electrochemical sensing, and CO₂ hydrogenation, **ii)** improving their efficiency and stability via various modification from functionalization (such as defect engineering beside mixed-metal) to exchange metals in most applications that have been investigated more, such as OER/HER, batteries, and supercapacitors via emphasize on the role of metal synergy, **iii)** using various trend materials and their incorporation with MMOFs such as single-atom catalysis procedures, **iv)** increase in conductivity of MMOFs and their derivatives for better electrochemical response and signal-to-noise ratio issues, **v)** applying diverse metal-based, and carbon-based materials such as MXene, oxides, graphene, and others to MMOF and their derivations to form MMOF composites and to develop in-situ analysis beside engineering of materials.

Acknowledgements

Support of this investigation by Tarbiat Modares University is gratefully acknowledged. H.G. is thankful for financial support by the Spanish Ministry of Science and Innovation (CEX-2021-001230-S and PDI2021-0126071-OB-CO21 funded by MCIN/AEI/ 10.13039/501100011033) and Generalitat Valenciana (Prometeo 2021/038 and Advanced Materials programme Graphica MFA/2022/023 with funding from European Union NextGenerationEU PRTR-C17.I1). A.D. is a beneficiary of a grant María Zambrano in Universitat Politècnica de València within the



framework of the grants for the retraining in the Spanish university system (Spanish Ministry of Universities, financed by the European Union, NextGeneration EU).

References

1. S. Kitagawa and M. Kondo, *Bulletin of the Chemical Society of Japan*, 1998, **71**, 1739–1753.
2. H. Li, M. Eddaoudi, M. O'Keeffe and O. M. Yaghi, *Nature*, 1999, **402**, 276–279.
3. A. K. Cheetham, G. Férey and T. Loiseau, *Angewandte Chemie International Edition*, 1999, **38**, 3268–3292.
4. H. Ghasempour, F. Zarekarizi and A. Morsali, *CrystEngComm*, 2022, **24**, 4074–4084.
5. R. R. Moslehabadi, Z. Hedayati, M. Mazraeh, S. Asghar, F. Rouhani and A. Morsali, *Journal of Materials Chemistry B*, 2025, **13**, 7554–7608.
6. X.-W. Yan, A. Hakimifar, F. Bigdeli, Y. Hanifehpour, S.-J. Wang, K.-G. Liu, A. Morsali and S. W. Joo, *Crystals*, 2023, **13**, 1344.
7. D. Ma, B. Li, K. Liu, X. Zhang, W. Zou, Y. Yang, G. Li, Z. Shi and S. Feng, *Journal of Materials Chemistry A*, 2015, **3**, 23136–23142.
8. Z. Karimzadeh, B. Shokri and A. Morsali, *Applied Physics Letters*, 2023, **123**.
9. X.-W. Yan, F. Bigdeli, M. Abbasi-Azad, S.-J. Wang and A. Morsali, *Coordination Chemistry Reviews*, 2024, **520**, 216126.
10. H. Wang, X. Pei, M. J. Kalmutzki, J. Yang and O. M. Yaghi, *Accounts of Chemical Research*, 2022, **55**, 707–721.
11. F. Afshariazar, A. Morsali, J. Wang and P. C. Junk, *Chemistry – A European Journal*, 2020, **26**, 1355–1362.
12. M. Rubio-Martinez, C. Avci-Camur, A. W. Thornton, I. Imaz, D. Maspoch and M. R. Hill, *Chemical Society Reviews*, 2017, **46**, 3453–3480.
13. M. Y. Masoomi, A. Morsali, A. Dhakshinamoorthy and H. Garcia, *Angewandte Chemie*, 2019, **131**, 15330–15347.
14. G. Xu, C. Zhu and G. Gao, *Small*, 2022, **18**, 2203140.
15. R. Abazari, S. Sanati and A. Morsali, *Inorganic Chemistry*, 2022, **61**, 3396–3405.
16. M. Hu, J. Liu, S. Song, W. Wang, J. Yao, Y. Gong, C. Li, H. Li, Y. Li, X. Yuan, Z. Fang, H. Xu, W. Song and Z. Li, *ACS Catalysis*, 2022, **12**, 3238–3248.
17. H. Wang, X. Zhang, X. Wu, Y. Kang, Y. Huang, Z. Zhao, Z. Li, T. Zhou, J. Wang, W. Zhu and C. Pan, *Journal of Materials Chemistry A*, 2025, **13**, 9952–9962.
18. Q. Qian, P. A. Asinger, M. J. Lee, G. Han, K. Mizrahi Rodriguez, S. Lin, F. M. Benedetti, A. X. Wu, W. S. Chi and Z. P. Smith, *Chemical Reviews*, 2020, **120**, 8161–8266.
19. X.-G. Han, P.-F. Wang, Y.-H. Zhang, H.-Y. Liu, J.-J. Tang, G. Yang and F.-N. Shi, *Inorganica Chimica Acta*, 2022, **536**, 120916.
20. S. Kubendhiran, R.-J. Chung, C. Kongvarhodom, H.-M. Chen, S. Yougbaré, M. Saukani, Y.-F. Wu and L.-Y. Lin, *ACS Applied Energy Materials*, 2025, **8**, 6339–6352.
21. H. Shu, T. Lai, J. Ren, X. Cui, X. Tian, Z. Yang, X. Xiao and Y. Wang, *Nanotechnology*, 2022, **33**, 135502.
22. A. M. Rice, G. A. Leith, O. A. Ejegbabwo, E. A. Dolgopolova and N. B. Shustova, *ACS Energy Letters*, 2019, **4**, 1938–1946.
23. R. E. Sikma, K. S. Butler, D. J. Vogel, J. A. Harvey and D. F. Sava Gallis, *Journal of the American Chemical Society*, 2024, **146**, 5715–5734.
24. S. Abednatanzi, P. Gohari Derakhshandeh, H. Depauw, F.-X. Coudert, H. Vrielinck, P. Van Der Voort and K. Leus, *Chemical Society Reviews*, 2019, **48**, 2535–2565.



- Open Access Article. Published on 12 Februar 2026. Downloaded on 16.02.26 09:35:19.
This article is licensed under a Creative Commons Attribution-NonCommercial 3.0 Unported Licence.
25. J. Bitzer and W. Kleist, *Chemistry – A European Journal*, 2019, **25**, 1866–1882.
26. M. Ahmed, *Inorganic Chemistry Frontiers*, 2022, **9**, 3003–3033.
27. L. Chen, H.-F. Wang, C. Li and Q. Xu, *Chemical Science*, 2020, **11**, 5369–5403.
28. X. Luo, R. Abazari, M. Tahir, W. K. Fan, A. Kumar, T. Kalhorizadeh, A. M. Kirillov, A. R. Amani-Ghadim, J. Chen and Y. Zhou, *Coordination Chemistry Reviews*, 2022, **461**, 214505.
29. R. Rajak, R. Kumar, S. N. Ansari, M. Saraf and S. M. Mobin, *Dalton Transactions*, 2020, **49**, 11792–11818.
30. S. Sanati, R. Abazari, J. Albero, A. Morsali, H. García, Z. Liang and R. Zou, *Angewandte Chemie International Edition*, 2021, **60**, 11048–11067.
31. J.-E. Zhou, J. Chen, Y. Peng, Y. Zheng, A. Zeb and X. Lin, *Coordination Chemistry Reviews*, 2022, **472**, 214781.
32. Q. Liang, J. Chen, F. Wang and Y. Li, *Coordination Chemistry Reviews*, 2020, **424**, 213488.
33. X. Qin, D. Kim and Y. Piao, *Carbon Energy*, 2021, **3**, 66–100.
34. J. Du, F. Li and L. Sun, *Chemical Society Reviews*, 2021, **50**, 2663–2695.
35. S. Sanati, A. Morsali and H. García, *Energy & Environmental Science*, 2022, **15**, 3119–3151.
36. J. Ji, W. Lou and P. Shen, *International Journal of Hydrogen Energy*, 2022, **47**, 39443–39469.
37. D. H. Taffa, D. Balkenhol, M. Amiri and M. Wark, *Small Structures*, 2023, **4**, 2200263.
38. S. Navalón, A. Dhakshinamoorthy, M. Álvaro, B. Ferrer and H. García, *Chemical Reviews*, 2023, **123**, 445–490.
39. R. Jaryal, R. Kumar and S. Khullar, *Coordination Chemistry Reviews*, 2022, **464**, 214542.
40. C. Zhang, Q. Liu, P. Wang, J. Zhu, D. Chen, Y. Yang, Y. Zhao, Z. Pu and S. Mu, *Small*, 2021, **17**, 2104241.
41. Y. Li, Y. Xu, W. Yang, W. Shen, H. Xue and H. Pang, *Small*, 2018, **14**, 1704435.
42. H. Wu, X. Li, S. Huai, S. Zhang, W. Ruan, X. Huang, C. Cheng, M. Qu, P. Li and X. Yu, *Journal of Materials Chemistry A*, 2025, **13**, 30324–30337.
43. M. Cui, B. Xu, X. Shi, Q. Zhai, Y. Dou, G. Li, Z. Bai, Y. Ding, W. Sun, H. Liu and S. Dou, *Journal of Materials Chemistry A*, 2024, **12**, 18921–18947.
44. M. S. Khan, Y. Li, D.-S. Li, J. Qiu, X. Xu and H. Y. Yang, *Nanoscale Advances*, 2023, **5**, 6318–6348.
45. Z. Qian, R. Zhang, Y. Xiao, H. Huang, Y. Sun, Y. Chen, T. Ma and X. Sun, *Advanced Energy Materials*, 2023, **13**, 2300086.
46. S.-H. Guo, X.-J. Qi, H.-M. Zhou, J. Zhou, X.-H. Wang, M. Dong, X. Zhao, C.-Y. Sun, X.-L. Wang and Z.-M. Su, *Journal of Materials Chemistry A*, 2020, **8**, 11712–11718.
47. J. Wang, S. Zhang, Y. Han, L. Zhang, Q. Wang, G. Wang and X. Zhang, *Molecular Catalysis*, 2022, **532**, 112741.
48. H. Dong, X. Zhang, X.-C. Yan, Y.-X. Wang, X. Sun, G. Zhang, Y. Feng and F.-M. Zhang, *ACS Applied Materials & Interfaces*, 2019, **11**, 45080–45086.
49. N. K. Chaudhari, H. Jin, B. Kim and K. Lee, *Nanoscale*, 2017, **9**, 12231–12247.
50. S. Mao, L. Ye, S. Jin, C. Zhou, J. Pang and W. Xu, *Inorganic Chemistry*, 2024, **63**, 6005–6015.
51. J. Ding, D. Guo, N. Wang, H.-F. Wang, X. Yang, K. Shen, L. Chen and Y. Li, *Angewandte Chemie International Edition*, 2023, **62**, e202311909.
52. Y. Li, M. Lu, Y. Wu, H. Xu, J. Gao and J. Yao, *Advanced Materials Interfaces*, 2019, **6**, 1900290.
53. R. Bhosale, S. Bhosale, V. Chavan, C. Jambhale, D.-k. Kim and S. Kolekar, *ACS Applied Nano Materials*, 2024, **7**, 2244–2257.
54. M. R. Tamtam, G. S. Choi, S. P. Kumar Vangala, J. Shim, N. N. Nguyen and N. N. Dang, *The Journal of Physical Chemistry Letters*, 2025, **16**, 10655–10668.
55. S. Khan, T. Noor, N. Iqbal and E. Pervaiz, *ChemNanoMat*, 2022, **8**, e202200115.
56. Y. Peng, S. Sanati, A. Morsali and H. García, *Angewandte Chemie International Edition*, 2023, **62**, e202214707.

- Open Access Article. Published on 12 Februar 2026. Downloaded on 16.02.26 09:35:19.
This article is licensed under a Creative Commons Attribution-NonCommercial 3.0 Unported Licence.
57. Y. Liu, S. Wang, Z. Li, H. Chu and W. Zhou, *Coordination Chemistry Reviews*, 2023, **484**, 215117.
58. M. Z. Iqbal, U. Aziz, S. Aftab and H. H. Hegazy, *International Journal of Hydrogen Energy*, 2023, **48**, 17801–17826.
59. C. Li, Y. Liu, L. Guan, K. Li, G. Wang and Y. Lin, *Chemical Engineering Journal*, 2020, **400**, 125884.
60. W. Zhou, Z. Xue, Q. Liu, Y. Li, J. Hu and G. Li, *ChemSusChem*, 2020, **13**, 5647–5653.
61. Y. Xu, Q. Zhou, T. Liu, T. Ren, H. Yu, K. Deng, Z. Wang, L. Wang and H. Wang, *Chemical Communications*, 2023, **59**, 7623–7626.
62. A. Abdelhafiz, M. H. Mohammed, J. Abed, D.-C. Lee, M. Chen, A. S. Helal, Z. Ren, F. Alamgir, E. Sargent, P. A. Kohl, S. K. Elsaidi and J. Li, *Advanced Energy Materials*, 2024, **14**, 2303350.
63. C. Zhang, R. Lu, C. Liu, J. Lu, Y. Zou, L. Yuan, J. Wang, G. Wang, Y. Zhao and C. Yu, *Advanced Science*, 2022, **9**, 2104768.
64. H. Wang, J. Bai, Q. He, Y. Liao, S. Wang and L. Chen, *Journal of Colloid and Interface Science*, 2024, **665**, 172–180.
65. F. Ismail, A. Abdellah, V. Sudheeshkumar, A. Rakhsha, W. Chen, N. Chen and D. C. Higgins, *ACS Applied Energy Materials*, 2022, **5**, 9408–9417.
66. S. L. Fereja, Z. Zhang, Z. Fang, J. Guo, X. Zhang, K. Liu, Z. Li and W. Chen, *ACS Applied Materials & Interfaces*, 2022, **14**, 38727–38738.
67. R. Abazari, S. Sanati, P. Stelmachowski, Q. Wang, A. Krawczuk, J. Goscianska and M. Liu, *Inorganic Chemistry*, 2024, **63**, 5642–5651.
68. L. Wen, X. Li, R. Zhang, H. Liang, Q. Zhang, C. Su and Y.-J. Zeng, *ACS Applied Materials & Interfaces*, 2021, **13**, 14181–14188.
69. X. Wang, G. Zhang, W. Yin, S. Zheng, Q. Kong, J. Tian and H. Pang, *Carbon Energy*, 2022, **4**, 246–281.
70. J. Wang, J. Liang, Y. Lin, K. Shao, X. Chang, L. Qian, Z. Li and P. Hu, *Chemical Engineering Journal*, 2022, **446**, 137368.
71. T.-L. Wu, X.-N. Tan, T.-T. Nong, Y.-J. Pan, P.-F. Qiu, J.-Q. He, Y. Zhou, X.-C. Tan, Z.-Y. Huang and L. Han, *Chemical Engineering Journal*, 2023, **457**, 141238.
72. H. Jiang, J. Xian, R. Hu, S. Mi, L. Wei, G. Fang, Z. Wu, S. Xu, M. Fan, K. Liu, H. Yu, W. Xu and J. Wan, *Chemical Engineering Journal*, 2023, **455**, 140804.
73. L.-J. Ma, C.-Y. Luo, R.-N. Wang, Y.-C. Tan, J.-L. Hou and Q.-Y. Zhu, *ACS Energy Letters*, 2023, **8**, 4427–4437.
74. K.-B. Wang, R. Bi, Z.-K. Wang, Y. Chu and H. Wu, *New Journal of Chemistry*, 2020, **44**, 3147–3167.
75. Y. Chen, W. Du, B. Dou, J. Chen, L. Hu, A. Zeb and X. Lin, *CrystEngComm*, 2022, **24**, 2729–2743.
76. T. Zhao, H. Wu, X. Wen, J. Zhang, H. Tang, Y. Deng, S. Liao and X. Tian, *Coordination Chemistry Reviews*, 2022, **468**, 214642.
77. C. Vallés-García, E. Gkaniatsou, A. Santiago-Portillo, M. Giménez-Marqués, M. Álvaro, J.-M. Gómez, N. Steunou, C. Sicard, S. Navalón, C. Serre and H. García, *Journal of Materials Chemistry A*, 2020, **8**, 17002–17011.
78. N. Antil, M. Chauhan, N. Akhtar, R. Newar, W. Begum, J. Malik and K. Manna, *ACS Catalysis*, 2022, **12**, 11159–11168.
79. C. Chen, X. Ji, Y. Xiong and J. Jiang, *Chemical Engineering Journal*, 2024, **481**, 148555.
80. S. Li, J. Tan, Z. Jiang, J. Wang and Z. Li, *Chemical Engineering Journal*, 2020, **384**, 123354.
81. S.-C. Fan, S.-Q. Chen, J.-W. Wang, Y.-P. Li, P. Zhang, Y. Wang, W. Yuan and Q.-G. Zhai, *Inorganic Chemistry*, 2022, **61**, 14131–14139.
82. J.-M. Li, Q.-C. Lin, N. Li, Z.-H. Li, G. Tan, S.-J. Liu, L.-H. Chung, W.-M. Liao, L. Yu and J. He, *Advanced Functional Materials*, 2023, **33**, 2210717.
83. Y. Yang, X. Hu, G. Wang, J. Han, Q. Zhang, W. Liu, Z. Xie and Z. Zhou, *Advanced Functional Materials*, 2024, **34**, 2315354.

- Open Access Article. Published on 12 Februar 2026. Downloaded on 16.02.26 09:35:19.
This article is licensed under a Creative Commons Attribution-NonCommercial 3.0 Unported Licence.
84. W. Wang, B. Ibarlucea, C. Huang, R. Dong, M. Al Aiti, S. Huang and G. Cuniberti, *Nanoscale Horizons*, 2024, **9**, 1432–1474.
85. P. Mhettar, N. Kale, J. Pantwalawalkar, S. Nangare and N. Jadhav, *ADMET and DMPK*, 2024, **12**, 27–62.
86. A. Wang, M. Walden, R. Ettlinger, F. Kiessling, J. J. Gassensmith, T. Lammers, S. Wuttke and Q. Peña, *Advanced Functional Materials*, 2024, **34**, 2308589.
87. F. Zadehahmadi, N. T. Eden, H. Mahdavi, K. Konstas, J. I. Mardel, M. Shaibani, P. C. Banerjee and M. R. Hill, *Environmental Science: Water Research & Technology*, 2023, **9**, 1305–1330.
88. Q. Xia, H. Wang, B. Huang, X. Yuan, J. Zhang, J. Zhang, L. Jiang, T. Xiong and G. Zeng, *Small*, 2019, **15**, 1803088.
89. X. Liu, T. Liang, R. Zhang, Q. Ding, S. Wu, C. Li, Y. Lin, Y. Ye, Z. Zhong and M. Zhou, *ACS Applied Materials & Interfaces*, 2021, **13**, 9643–9655.
90. S. Zhang, Y. Zhang, F. Baig and T.-F. Liu, *Crystal Growth & Design*, 2021, **21**, 3100–3122.
91. M. Al Haydar, H. R. Abid, B. Sunderland and S. Wang, *Drug design, development and therapy*, 2018, 23–35.
92. Z. Mu, S. Wu, J. Guo, M. Zhao and Y. Wang, *ACS Sustainable Chemistry & Engineering*, 2022, **10**, 2984–2993.
93. S. Kulandaivel, Y.-K. Lu, C.-H. Lin and Y.-C. Yeh, *Journal of Materials Chemistry B*, 2025, **13**, 151–159.
94. Z. Deng, J. Cao, L. Zhao, Z. Zhang and J. Yuan, *Molecules*, 2024, **29**, 3739.
95. D. Zhao, W. Jiang, W. Zhang, C. Zhang, W. Zhao, Z. Chen, Y. Liu and J. Xu, *Chemistry of Materials*, 2025, **37**, 4853–4867.
96. C. Ding, W. Zhong, Y. Cao, T. Ma, H. Ye, Z. Fang, Y. Feng, S. Zhao, J. Yang, Y. Li, L. Shen and W. He, *Chemical Engineering Science*, 2025, **302**, 120888.
97. M. Burud, S. A. Patil, V. Jadhav, P. Chougale, S. Mane-Gavade, R. Ustad, J. Shen, A. Supale, S. Sabale and D.-K. Kim, *Energy & Fuels*, 2025, **39**, 13648–13657.
98. R. Li, J. Wang, B. Guo, J. Zhang, Y. Sun, J. Wang, H. Zhang, W. Li and X. Feng, *Journal of Alloys and Compounds*, 2025, **1036**, 181892.
99. G. Arunkumar, G. Deviga, M. Mariappan, M. Pannipara, A. G. Al-Sehemi and S. P. Anthony, *Dalton Transactions*, 2025, **54**, 4225–4233.
100. X. Hou, Z. Han, X. Xu, D. Sarker, J. Zhou, M. Wu, Z. Liu, M. Huang and H. Jiang, *Chemical Engineering Journal*, 2021, **418**, 129330.
101. H. Xu, C. Shan, X. Wu, M. Sun, B. Huang, Y. Tang and C.-H. Yan, *Energy & Environmental Science*, 2020, **13**, 2949–2956.
102. W. Zhang, M. Niu, J. Yu, S. Li, Y. Wang and K. Zhou, *Advanced Functional Materials*, 2023, **33**, 2302014.
103. Y. Kong, D. Xiong, C. Lu, J. Wang, T. Liu, S. Ying, X. Ma and F.-Y. Yi, *ACS Applied Materials & Interfaces*, 2022, **14**, 37804–37813.
104. Y. Xie, F. Le, X. Yang, W. Shu, R. Sheng, A. Liu and W. Jia, *Dalton Transactions*, 2025, **54**, 10907–10915.
105. B. Yan, D. Wang, W. Ji and Y. Fu, *Journal of Materials Chemistry C*, 2025, **13**, 11756–11763.
106. Y. Zhao, J. Ma, J. Yin, H. Han, X. Zhang, Y. Cao and W. Cai, *Applied Surface Science*, 2024, **657**, 159783.
107. Y. Han, J. Wang, X. Yan, D. Wang, H. Han and C. Sun, *Journal of Hazardous Materials*, 2025, **499**, 140196.
108. H. Ghasempour, F. Zarekarizi, B. Habibi, G. Zhang, A. Ramazani and A. Morsali, *CrystEngComm*, 2025, **27**, 4826–4834.
109. H. Feng, Q. Xu, T. Lv and H. Liu, *Applied Catalysis B: Environment and Energy*, 2024, **351**, 123949.

- Open Access Article. Published on 12 Februar 2026. Downloaded on 16.02.26 09:35:19.
This article is licensed under a Creative Commons Attribution-NonCommercial 3.0 Unported Licence.
- (cc) BY-NC
110. Y. Zhu, Q. Dong, A. Sial, A. Labidi, K. Zhao, X. Li, J. Wang and C. Wang, *Applied Catalysis O: Open*, 2025, **200**, 207030.
 111. X. Zhong, J. Xu and S. Song, *Applied Surface Science*, 2025, **690**, 162659.
 112. S. Adak, R. Ghosh Chaudhuri and Mrinal K. Mandal, *Applied Organometallic Chemistry*, 2025, **39**, e70412.
 113. Z. Yin, J. Liang, Z. Zhang, H. Luo and J. Zhou, *Journal of Colloid and Interface Science*, 2022, **623**, 405–416.
 114. L. Karuppasamy, L. Gurusamy, S. Ananan, S. C. Barton, C.-H. Liu and J. J. Wu, *Electrochimica Acta*, 2023, **449**, 142242.
 115. C. Feng, Q. An, Q. Zhang, L. Huang, N. Wang, X. Zhang, Y. Xu, M. Xie, R. Wang, Y. Jiao and J. Chen, *International Journal of Hydrogen Energy*, 2024, **55**, 189–198.
 116. Q. Zhai, M. Zhang, H. Ji, H. Bian, H. Wu, Y. Ma, Y. Yang, S. Tang, M. Cui and X. Meng, *The Journal of Physical Chemistry C*, 2022, **126**, 20204–20212.
 117. Q. Wang, X. Ma, P. Ma, R. Bi and S. Song, *ACS Applied Nano Materials*, 2023, **6**, 9339–9350.
 118. W. Ke, Y. Zhang, A. L. Imbault and Y. Li, *International Journal of Hydrogen Energy*, 2021, **46**, 20941–20949.
 119. W.-D. Zhang, H. Yu, T. Li, Q.-T. Hu, Y. Gong, D.-Y. Zhang, Y. Liu, Q.-T. Fu, H.-Y. Zhu, X. Yan and Z.-G. Gu, *Applied Catalysis B: Environmental*, 2020, **264**, 118532.
 120. C. Chen, Y. Tuo, Q. Lu, H. Lu, S. Zhang, Y. Zhou, J. Zhang, Z. Liu, Z. Kang, X. Feng and D. Chen, *Applied Catalysis B: Environmental*, 2021, **287**, 119953.
 121. Y. Zhang, Z. Li, K. Zhang, Z. Wu, F. Gao and Y. Du, *Applied Surface Science*, 2022, **590**, 153102.
 122. W. Dong, N. Huang, Y. Zhao, Y. Feng, G. Zhao, S. Ran and W. Liu, *Journal of Electroanalytical Chemistry*, 2024, **959**, 118184.
 123. D. Senthil Raja, C.-L. Huang, Y.-A. Chen, Y. Choi and S.-Y. Lu, *Applied Catalysis B: Environmental*, 2020, **279**, 119375.
 124. D. Xing, H. Wang, Z. Cui, L. Lin, Y. Liu, Y. Dai and B. Huang, *Journal of Colloid and Interface Science*, 2024, **656**, 309–319.
 125. I. W. P. Chen, W.-Y. Chen and T. Y. Liu, *Materials Today Chemistry*, 2024, **35**, 101873.
 126. X.-N. Lv, Y.-H. Zhang, P.-P. Sun, P.-F. Wang, J.-J. Tang, G. Yang, Q. Shi and F.-N. Shi, *Journal of Solid State Chemistry*, 2022, **306**, 122786.
 127. W. Sun, S. Chen and Y. Wang, *Dalton Transactions*, 2019, **48**, 2019–2027.
 128. L. Fan, X. Guo, W. Li, X. Hang and H. Pang, *Chinese Chemical Letters*, 2023, **34**, 107447.
 129. S. Ebrahimi-Koodehi, F. E. Ghodsi and J. Mazloom, *International Journal of Energy Research*, 2022, **46**, 24368–24380.
 130. C. Xu, M. Bao, J. Ren and Z. Zhang, *RSC Advances*, 2020, **10**, 39080–39086.
 131. H.-T. T. Nguyen, K.-N. T. Tran, L. Van Tan, V. A. Tran, V.-D. Doan, T. Lee and T. D. Nguyen, *Materials Chemistry and Physics*, 2021, **272**, 125040.
 132. L. Gu, G. Deng, R. Huang and X. Shi, *Nanoscale*, 2022, **14**, 15821–15831.
 133. Y. Zhang, R. Huang, Y. Fang, J. Wang, Z. Yuan, X. Chen, W. Zhu, Y. Cai and X. Shi, *Separation and Purification Technology*, 2024, **336**, 126164.
 134. C. Li, H. Yu, S. Guo, J. Jia, Y. Chang, M. Jia and J. Wang, *New Journal of Chemistry*, 2024, **48**, 3364–3369.
 135. Q. Liu, J.-Y. Tan, J.-Y. Zhang, N. Zhang and Z.-J. Liu, *Microporous and Mesoporous Materials*, 2021, **310**, 110626.
 136. Y. Hu, J. Zhang, H. Huo, Z. Wang, X. Xu, Y. Yang, K. Lin and R. Fan, *Catalysis Science & Technology*, 2020, **10**, 315–322.
 137. O. K. T. Nguyen, L. X. Nong, V. H. Nguyen and T. D. Nguyen, *ChemistrySelect*, 2023, **8**, e202302598.

- Open Access Article. Published on 12 Februar 2026. Downloaded on 16.02.26 09:35:19.
This article is licensed under a Creative Commons Attribution-NonCommercial 3.0 Unported Licence.
138. D. Zeng, G. Zhu and C. Xia, *Fuel Processing Technology*, 2022, **235**, 107374.
139. Y. Li, G. Zhao, B. An, K. Xu, D. Wu, X. Ren, H. Ma, X. Liu, R. Feng and Q. Wei, *Analytical Chemistry*, 2024, **96**, 4067–4075.
140. A. Yousaf, Z. Zhao, L. Wu, S. Hanif and N. Akhtar, *Process Safety and Environmental Protection*, 2024, **191**, 102–111.
141. P. Yuan, Z. Deng, P. Qiu, Z. Yin, Y. Bai, Z. Su and J. He, *Food Control*, 2023, **144**, 109357.
142. H.-R. Zhang, X.-H. Ren, D.-W. Wang, X.-W. He, W.-Y. Li and Y.-K. Zhang, *Talanta*, 2023, **259**, 124506.
143. C. Duan and J. Zheng, *Journal of The Electrochemical Society*, 2019, **166**, B942.
144. F. T. Alshorifi, S. M. El Dafrawy and A. I. Ahmed, *ACS omega*, 2022, **7**, 23421–23444.
145. W. A. El-Yazeed, Y. Abou El-Reash, L. Elatwy and A. I. Ahmed, *RSC advances*, 2020, **10**, 9693–9703.
146. Z. Zhang, J. Liu, Z. Wang and J. Zhang, *Industrial & Engineering Chemistry Research*, 2020, **60**, 781–789.
147. Q. Guo, X.-P. Ma, L.-W. Zheng, C.-X. Zhao, X.-Y. Wei, Y. Xu, Y. Li, J.-J. Xie, K.-G. Zhang and C.-G. Yuan, *Ecotoxicology and Environmental Safety*, 2022, **245**, 114097.
148. W. A. El-Yazeed, Y. Abou El-Reash, L. Elatwy and A. I. Ahmed, *Journal of the Taiwan Institute of Chemical Engineers*, 2020, **114**, 199–210.
149. Z. Garazhian, A. Farrokhi, A. Rezaeifard, M. Jafarpour and R. Khani, *RSC advances*, 2021, **11**, 21127–21136.
150. J. Yao, Z. Zhao, L. Yu, J. Huang, S. Shen, S. Zhao, Y. Wu, X. Tian, J. Wang and Q. Xia, *Journal of Materials Chemistry A*, 2023, **11**, 14728–14737.
151. Q. Wu, M. S. Siddique and W. Yu, *Journal of Hazardous Materials*, 2021, **401**, 123261.
152. R. Liu, W. Zhang, Y. Chen and Y. Wang, *Colloids and Surfaces A: Physicochemical and Engineering Aspects*, 2020, **587**, 124334.
153. X. Liu, H. Yang, Y. Diao, Q. He, C. Lu, A. Singh, A. Kumar, J. Liu and Q. Lan, *Chemosphere*, 2022, **307**, 135729.
154. A. Helal, S. Shaheen Shah, M. Usman, M. Y. Khan, M. A. Aziz and M. Mizanur Rahman, *The Chemical Record*, 2022, **22**, e202200055.
155. X. Zha, W. Yang, L. Shi, Y. Li, Q. Zeng, J. Xu and Y. Yang, *ACS Applied Materials & Interfaces*, 2022, **14**, 37843–37852.
156. G. Li, Y. Liu, Y. Shen, Q. Fang and F. Liu, *Frontiers in Chemical Engineering*, 2021, **3**, 636439.
157. C. Lin, X. Guo, L. Chen, T. You, J. Lu and D. Sun, *Journal of Colloid and Interface Science*, 2022, **628**, 731–744.
158. X. Han, W. Yang, C. Yin, X. Zhang, C. Yi and Z. Fan, *Applied Surface Science*, 2025, **679**, 160964.
159. Y. Yao, K. Wei, S. Zhao, H. Zhou, B. Kui, G. Zhu, W. Wang, P. Gao and W. Ye, *ACS Sustainable Chemistry & Engineering*, 2025, **13**, 1245–1252.
160. Y. Wang, L. Fu, J. Wu, F. Yang and L. Feng, *ChemSusChem*, 2025, **18**, e202401580.
161. X. Sun, L. Yang, D. Li and Z. Tian, *Journal of Molecular Structure*, 2025, **1322**, 140549.
162. Z.-H. Pu, S.-E. Yu, C.-C. Hsu, I. C. Ni, C.-I. Wu, N. Devi, C.-X. Liu, Y.-S. Chen, I. C. Cheng and J.-Z. Chen, *International Journal of Hydrogen Energy*, 2025, **113**, 429–440.
163. R. Pavadai, M. Arivazhagan, S. Prabu, S. Ingavale, G. Honnu, V. M. Gowri, S. Thongmee, C. Issro, D. Khamboonrueang and S. Kityakarn, *Materials Chemistry and Physics*, 2025, **345**, 131245.
164. W.-S. Liu, X. Hu, K. Zeng, C.-H. Ji, H. Feng, Y.-G. Zhou and Q.-Y. Cai, *Journal of Materials Chemistry A*, 2025, **13**, 3174–3184.
165. Sonadia, Z. Iqbal, W. Miran, A. Ul-Hamid, K. S. Ayub and F. Azad, *Energy & Fuels*, 2024, **38**, 5397–5406.

- Open Access Article. Published on 12 Februar 2026. Downloaded on 16.02.26 09:35:19.
This article is licensed under a Creative Commons Attribution-NonCommercial 3.0 Unported Licence.
- 
166. M. Ding, J. Chen, M. Jiang, X. Zhang and G. Wang, *Journal of Materials Chemistry A*, 2019, **7**, 14163–14168.
167. Z.-Y. Zhao, X. Sun, H. Gu, Z. Niu, P. Braunstein and J.-P. Lang, *ACS Applied Materials & Interfaces*, 2022, **14**, 15133–15140.
168. L. Zhao, J. Yan, H. Huang, X. Du, H. Chen, X. He, W. Li, W. Fang, D. Wang, X. Zeng, J. Dong and Y. Liu, *Advanced Functional Materials*, 2024, **34**, 2310902.
169. K. Yue, J. Liu, Y. Zhu, C. Xia, P. Wang, J. Zhang, Y. Kong, X. Wang, Y. Yan and B. Y. Xia, *Energy & Environmental Science*, 2021, **14**, 6546–6553.
170. J. Hou, N. Chen, D. Bi, Z. Liu and Y. Liang, *International Journal of Hydrogen Energy*, 2025, **101**, 1070–1076.
171. S. Xu, M. Li, H. Wang, Y. Sun, W. Liu, J. Duan and S. Chen, *The Journal of Physical Chemistry C*, 2022, **126**, 14094–14102.
172. M. Fang, X. Gao, J. Liang, B. Guo, L. Zou, J. Lu, Y. Gao, E. C. M. Tse and J. Liu, *Journal of Materials Chemistry A*, 2022, **10**, 7013–7019.
173. Y. Sun, Z. Xue, Q. Liu, Y. Jia, Y. Li, K. Liu, Y. Lin, M. Liu, G. Li and C.-Y. Su, *Nature Communications*, 2021, **12**, 1369.
174. M. Li, H. Sun, J. Yang, M. Humayun, L. Li, X. Xu, X. Xue, A. Habibi-Yangjeh, K. Temst and C. Wang, *Chemical Engineering Journal*, 2022, **430**, 132733.
175. Y. Xu, Y. Xia, S. Fan, W. Gao, Z. Gao and C. Wang, *Small*, **n/a**, e08771.
176. J. Hu, A. Rendón-Patiño, I. S. Khan, L. Garzon-Tovar, D. Mateo, J. Albero, J. Gascon and H. García, *Journal of Energy Storage*, 2025, **108**, 114990.
177. N. Kumar, P. Bhattacharya, A. Jana and S. Kumar, *Inorganic Chemistry Communications*, 2025, **177**, 114445.
178. X. Wang, C. Hao, J. Zhang, C. Ni, X. Wang and Y. Shen, *Journal of Power Sources*, 2022, **539**, 231594.
179. A. Umar, S. Alam, N. u. Rehman, M. Zahoor, R. Ullah, E. A. Ali and M. N. Umar, *Inorganic Chemistry Communications*, 2025, **180**, 114942.
180. G. Karthikeyan, S. Mohan, P. M. Austeria and R. G. Balakrishna, *Small*, 2025, **21**, 2409133.
181. M. Zhao, H. Li, W. Li, J. Li, L. Yi, W. Hu and C. M. Li, *Chemistry – A European Journal*, 2020, **26**, 17091–17096.
182. M. Manivannan, V. Rajagopal, L. Krishnamoorthy, S. Dhanasurya, V. Suryanarayanan, M. Kathiresan, T. Raju and L. A. Jones, *New Journal of Chemistry*, 2023, **47**, 6330–6341.
183. J. Yin, C. Wang, J. Li, S. Yu, Z. Wu, Y. Zhang and Y. Du, *Inorganic Chemistry*, 2024, **63**, 5167–5174.
184. M. Zhang, W. Xu, T. Li, H. Zhu and Y. Zheng, *Inorganic Chemistry*, 2020, **59**, 15467–15477.
185. Q. Mou, Z. Xu, W. Zuo, T. Shi, E. Li, G. Cheng, X. Liu, H. Zheng, H. Li and P. Zhao, *Materials Chemistry Frontiers*, 2022, **6**, 2750–2759.
186. S. Xu, Q. Huang, J. Xue, Y. Yang, L. Mao, S. Huang and J. Qian, *Inorganic Chemistry*, 2022, **61**, 8909–8919.
187. H. Zhao, L. Zhang, L. Dai, F. Yao, Y. Huang, J. Deng, Y. Fu, J. Zhu and J. Sun, *Applied Surface Science*, 2022, **592**, 153252.
188. Q. Qian, Y. Li, Y. Liu, L. Yu and G. Zhang, *Advanced Materials*, 2019, **31**, 1901139.
189. Z. Li, S. Deng, H. Yu, Z. Yin, S. Qi, L. Yang, J. Lv, Z. Sun and M. Zhang, *Journal of Materials Chemistry A*, 2022, **10**, 4230–4241.
190. Q. Liang, Y. Liu, Z. Xue, Z. Zhao, G. Li and J. Hu, *Chemical Communications*, 2022, **58**, 6966–6969.
191. S. Li, Z. Wang, T. Wang, Y. Yang, Y. Xiao, Y. Tian, H. Zhu, X. Jing and G. Zhu, *Chemistry – A European Journal*, 2023, **29**, e202301129.
192. H. Xu, C. Wang, G. He and H. Chen, *Dalton Transactions*, 2023, **52**, 8466–8472.

- Open Access Article. Published on 12 Februar 2026. Downloaded on 16.02.26 09:35:19.
This article is licensed under a Creative Commons Attribution-NonCommercial 3.0 Unported Licence.
193. Y. Zhang, Y. Mo, S. Wang, H. Zhong, Z. Cao and X. Ma, *Colloids and Surfaces A: Physicochemical and Engineering Aspects*, 2022, **642**, 128469.
194. Q. Li, Y. Liu, S. Niu, C. Li, C. Chen, Q. Liu and J. Huo, *Journal of Colloid and Interface Science*, 2021, **603**, 148–156.
195. D. Liu, H. Xu, C. Wang, H. Shang, R. Yu, Y. Wang, J. Li, X. Li and Y. Du, *Inorganic Chemistry*, 2021, **60**, 5882–5889.
196. S. Niu, C. Li, J. Huo, W. Dong, S. El Hankari, Y. Liang and Q. Li, *ACS Omega*, 2021, **6**, 13946–13952.
197. T. Liu, Y. Zhang, C. Ye, D. Wang, C. Wang and Y. Du, *Journal of Colloid and Interface Science*, 2024, **655**, 466–473.
198. W. Li, H. Zhang, K. Zhang, Z. Cheng, H. Chen, G. Tan, X. Feng, L. Wang and S. Mu, *Chemical Communications*, 2023, **59**, 4750–4753.
199. M. Rinawati, Y.-X. Wang, K.-Y. Chen and M.-H. Yeh, *Chemical Engineering Journal*, 2021, **423**, 130204.
200. K. Karuppasamy, R. Bose, D. B. Velusamy, D. Vikraman, P. Santhoshkumar, P. Sivakumar, A. Alfantazi and H.-S. Kim, *ACS Sustainable Chemistry & Engineering*, 2022, **10**, 14693–14704.
201. K. Srinivas, F. Ma, Y. Liu, Z. Zhang, Y. Wu and Y. Chen, *ACS Applied Materials & Interfaces*, 2022, **14**, 52927–52939.
202. J. Ma, B. Lu, S. Wang, W. He, X. Bai, T. Wang, X. Zhang, Y. Li, L. Zhang, J. Chen, F. Meng and Y. Fu, *New Journal of Chemistry*, 2020, **44**, 2459–2464.
203. Y. Du, M. Zhang, Z. Wang, Y. Liu, Y. Liu, Y. Geng and L. Wang, *Journal of Materials Chemistry A*, 2019, **7**, 8602–8608.
204. E. Sadeghi, S. Chamani, I. D. Yildirim, E. Erdem, N. S. Peighambardoust and U. Aydemir, *ACS Applied Materials & Interfaces*, 2024, **16**, 10078–10092.
205. T. Chen, C. Lu, J. Wang, Y. Kong, T. Liu, S. Ying, X. Ma and F.-Y. Yi, *Electrochimica Acta*, 2024, **480**, 143927.
206. Z. Gao, Y. Wang, L. Xu, Q. Tao, X. Wang, Z. Zhou, Y. Luo, J. Yu and Y. Huang, *Chemical Engineering Journal*, 2022, **433**, 133515.
207. S. Gopi, S. Perumal, E. M. Al Olayan, O. D. AlAmri, A. S. Aloufi, M. Kathiresan and K. Yun, *Chemosphere*, 2021, **267**, 129243.
208. D.-X. Yang, P.-F. Wang, H.-Y. Liu, Y.-H. Zhang, P.-P. Sun and F.-N. Shi, *Journal of Solid State Chemistry*, 2022, **309**, 122947.
209. J. Lin, C. Xu, M. Lu, X. Lin, Z. Ali, C. Zeng, X. Xu and Y. Luo, *ENERGY & ENVIRONMENTAL MATERIALS*, 2023, **6**, e12284.
210. Y. Chen, X. Hu, X. Chen, J.-H. Liu, Y. Huang and D. Cao, *Chemical Engineering Journal*, 2023, **478**, 147411.
211. H.-y. Chen, Y.-q. Huo, K.-z. Cai and Y. Teng, *Synthetic Metals*, 2021, **276**, 116761.
212. X. Hang, B. Liu, G. Yuan, X. Wang, Y. An and H. Pang, *Materials Today Chemistry*, 2023, **34**, 101754.
213. Y. Xie, H. Zhang, K. Zhang, R. Liu, Y. Sun, X. Gao, H. Bai, F. Yao and H. Yue, *Electrochimica Acta*, 2024, **477**, 143784.
214. Y. Zhu, Z. Tao, C. Cai, Y. Tan, A. Wang and Y. Yang, *Inorganic Chemistry Communications*, 2022, **139**, 109391.
215. B. Zhang, S. Song, W. Li, L. Zheng and X. Ma, *Ionics*, 2021, **27**, 3553–3566.
216. M. R. Abdul Karim, W. Khalid and R. Zahid, *Energy Technology*, 2024, **12**, 2301160.
217. R. Zahid, M. R. Abdul Karim, W. Khalid and M. A. Marwat, *Energy Technology*, 2024, **12**, 2300883.
218. M. Abedi, G. Mahmoudi, P. Hayati, B. Machura, F. I. Zubkov, K. Mohammadi, S. Bahrami, H. Derikvandi, Z. Mehrabadi and A. M. Kirillov, *New Journal of Chemistry*, 2019, **43**, 17457–17465.

- Open Access Article. Published on 12 Februar 2026. Downloaded on 16.02.26 09:35:19.
This article is licensed under a Creative Commons Attribution-NonCommercial 3.0 Unported Licence.
- (cc) BY-NC
- 219. D. Wang, M. Suo, S. Lai, L. Deng, J. Liu, J. Yang, S. Chen, M.-F. Wu and J.-P. Zou, *Applied Catalysis B: Environmental*, 2023, **321**, 122054.
 - 220. Z. Song, R. Li, D. Wen, J. Pei, H. Zhu and S. Ruan, *ACS Materials Letters*, 2023, **5**, 473–479.
 - 221. B. Wang, Y. Luo, L. Gao, B. Liu and G. Duan, *Biosensors and Bioelectronics*, 2021, **171**, 112736.
 - 222. Y. Yang, J.-L. Zhang, W.-B. Liang, J.-L. Zhang, X.-L. Xu, Y.-J. Zhang, R. Yuan and D.-R. Xiao, *Sensors and Actuators B: Chemical*, 2022, **362**, 131802.
 - 223. Z. Xu, Q. Wang, H. Zhangsun, S. Zhao, Y. Zhao and L. Wang, *Food Chemistry*, 2021, **349**, 129202.
 - 224. W. Li, S. Lv, Y. Wang, L. Zhang and X. Cui, *Sensors and Actuators B: Chemical*, 2019, **281**, 652–658.
 - 225. Y. Ma, P. Wei, M. Chen, X. Shi, X. Lu, X. Zhang and D. Sun, *Journal of Electroanalytical Chemistry*, 2023, **940**, 117490.
 - 226. F. M. Jais, S. Ibrahim, C. Y. Chee and Z. Ismail, *Journal of Environmental Chemical Engineering*, 2021, **9**, 106367.
 - 227. G.-R. Si, W. Wu, T. He, Z.-C. Xu, K. Wang and J.-R. Li, *ACS Materials Letters*, 2022, **4**, 1032–1036.
 - 228. J. Ma, W. Bai, X. Liu and J. Zheng, *Microchimica Acta*, 2022, **189**, 20.
 - 229. X. Shi, R. Hua, Y. Xu, T. Liu and G. Lu, *Sustainable Energy & Fuels*, 2020, **4**, 4589–4597.
 - 230. T. Zhang, H. Chen, L. Wang, Y. Liang and X. Zhang, *ACS Applied Nano Materials*, 2022, **5**, 15220–15227.
 - 231. E. Raphael Ezeigwe, L. Dong, J. Wang, L. Wang, W. Yan and J. Zhang, *Journal of Colloid and Interface Science*, 2020, **574**, 140–151.
 - 232. T. Zhang, X. Sun, S. Weng, S. Zhang, C. Xu, X. Gao and N. Zhu, *Journal of Molecular Structure*, 2025, **1321**, 140190.
 - 233. S. Tavakoli and A. Abbasi, *Research on Chemical Intermediates*, 2025, **51**, 1457–1472.
 - 234. F. Zheng, J. Lu, Q. Xu, M. Zhang, B. Zhao, J. Ji and Z. Zhou, *Journal of the Energy Institute*, 2025, **123**, 102339.
 - 235. S. K. Konavarapu, G. Kim, K. Shin and S. Y. Kim, *Chemistry – A European Journal*, 2025, **31**, e202500010.
 - 236. T.-m. Li, B.-q. Hu, J.-h. Han, W. Lu, F. Yu and B. Li, *Inorganic Chemistry*, 2022, **61**, 7051–7059.
 - 237. S. Ketrat, T. Maihom, S. Wannakao, M. Probst, S. Nokbin and J. Limtrakul, *Inorganic Chemistry*, 2017, **56**, 14005–14012.
 - 238. S. Li, Y. Hou, Q. Chen, X. Zhang, H. Cao and Y. Huang, *ACS Applied Materials & Interfaces*, 2020, **12**, 2581–2590.
 - 239. F. Akram, M. Tariq, A. Raza and N. Akhtar, *Polyhedron*, 2026, **283**, 117848.
 - 240. Y. Zou, W.-D. Zhang, M. Chen, J. Liu, Z.-G. Gu and X. Yan, *Journal of Colloid and Interface Science*, 2024, **653**, 11–19.
 - 241. F. Zheng, M. A. Gaikwad, Z. Fang, S. Jang and J. H. Kim, *Energy & Fuels*, 2024, **38**, 6290–6299.
 - 242. Z. Xu, C.-L. Yeh, Y. Jiang, X. Yun, C.-T. Li, K.-C. Ho, J. T. Lin and R. Y.-Y. Lin, *ACS Applied Materials & Interfaces*, 2021, **13**, 28242–28251.
 - 243. M. Zhao, T. Guo, W. Qian, Z. Wang, X. Zhao, L. Wen and D. He, *Chemical Engineering Journal*, 2021, **422**, 130055.
 - 244. H. Chu, R. Li, P. Feng, D. Wang, C. Li, Y. Yu and M. Yang, *ACS Catalysis*, 2024, **14**, 1553–1566.
 - 245. M. Nozari-Asbemarz, M. Amiri, A. Khodayari, A. Bezaatpour, S. Nouhi, P. Hosseini, M. Wark, R. Boukherroub and S. Szunerits, *ACS Applied Energy Materials*, 2021, **4**, 2951–2959.
 - 246. Y. Li, T. Zhao, M. Lu, Y. Wu, Y. Xie, H. Xu, J. Gao, J. Yao, G. Qian and Q. Zhang, *Small*, 2019, **15**, 1901940.
 - 247. X. Wang, J. Zhang, D. Ma, X. Feng, L. Wang and B. Wang, *ACS Applied Materials & Interfaces*, 2021, **13**, 33209–33217.

- Open Access Article. Published on 12 Februar 2026. Downloaded on 16.02.26 09:35:19.
This article is licensed under a Creative Commons Attribution-NonCommercial 3.0 Unported Licence.
248. Y. Li, B. Huang, X. Zhao, Z. Luo, S. Liang, H. Qin and L. Chen, *Journal of Power Sources*, 2022, **527**, 231149.
249. C. Kang, L. Ma, Y. Chen, L. Fu, Q. Hu, C. Zhou and Q. Liu, *Chemical Engineering Journal*, 2022, **427**, 131003.
250. M. Liu, H. Miao, T. Ye, J. Gao, L. Tan, Y. Tian, Z. Fu, L. Wen, M. Yan, W. Gu, G. Gu, Y. Wang and Y. Wang, *Advanced Functional Materials*, **n/a**, e12905.
251. H. Tariq, M. S. Khan, M. A. Khan, A. Ali, A. Shuja, M. Owais, S. Alam, Y. Khan and I. Murtaza, *ChemistrySelect*, 2025, **10**, e05134.
252. A. Veysi, M. Roushani and H. Najafi, *Heliyon*, 2025, **11**.
253. S. Wang, J. Lu, Q. Liu, H. Cui, H. Wang, X. Feng, K. Ge, Y. Yang and Y. Zhao, *Journal of Environmental Chemical Engineering*, 2025, **13**, 117176.
254. M. A. Karim, M. R. Abdul Karim, A. Ahmed and M. A. Marwat, *Electrochimica Acta*, 2025, **542**, 147509.
255. K.-R. Oh, H. Lee, G.-N. Yun, C. Yoo, J. W. Yoon, A. Awad, H.-W. Jeong and Y. K. Hwang, *ACS Applied Materials & Interfaces*, 2023, **15**, 9296–9306.
256. S. Guo, L. H. Kong, P. Wang, S. Yao, T. B. Lu and Z. M. Zhang, *Angewandte Chemie*, 2022, **134**, e202206193.
257. G. Li, L. Lu, L. Pei, Z. Ma, Y. Yuan, M.-L. Hu, Q. Miao and J. Zhong, *Inorganic Chemistry*, 2022, **61**, 738–745.
258. Y. Wu, W. Wang, W. Jiang, H. Li, Y. Ma, C. Liu and X. Yang, *International Journal of Hydrogen Energy*, 2022, **47**, 31587–31595.
259. Y. Pan, J. Zhang, Z. Zhao, L. Shi, B. Wu and L. Zeng, *International Journal of Hydrogen Energy*, 2021, **46**, 34565–34573.
260. R. Yu, C. Wang, D. Liu, X. Wang, J. Yin and Y. Du, *Inorganic Chemistry*, 2023, **62**, 609–617.
261. X. Hou, J. Zhou, X. Xu, X. Wang, S. Zhang, H. Wang and M. Huang, *Catalysis Communications*, 2022, **165**, 106445.
262. L. Ai, Y. Luo, W. Huang, Y. Tian and J. Jiang, *International Journal of Hydrogen Energy*, 2022, **47**, 12893–12902.
263. Y. Li, B. Thomas, C. Tang and T. Asefa, *Dalton Transactions*, 2023, **52**, 17834–17845.
264. L. Ma, Q. Xue, Y. Dang, L. Wang and Y. Zhou, *Journal of Colloid and Interface Science*, 2024, **655**, 234–242.
265. J. Ma, S. Wang, W. He, H. Chen, X. Zhai, F. Meng and Y. Fu, *ChemSusChem*, 2021, **14**, 5042–5048.
266. W. H. Choi, K.-H. Kim, H. Lee, J. W. Choi, D. G. Park, G. H. Kim, K. M. Choi and J. K. Kang, *Advanced Science*, 2021, **8**, 2100044.
267. R. Qi, Z. Zhong, F. Chen, X. Zhen, Q. Li, Y. Yang and Q. Ye, *Fuel*, 2024, **357**, 129882.
268. J.-T. Yuan, J.-J. Hou, X.-L. Liu, Y.-R. Feng and X.-M. Zhang, *Dalton Transactions*, 2020, **49**, 750–756.
269. S. S. Sankar, K. Manjula, G. Keerthana, B. Ramesh Babu and S. Kundu, *Crystal Growth & Design*, 2021, **21**, 1800–1809.
270. X. Deng, H. Qin, X. Liu, S. Zhu, J. Li, L. Ma and N. Zhao, *Journal of Alloys and Compounds*, 2022, **918**, 165650.
271. D. Taherinia, H. Hatami and F. Mirzaee Valadi, *Journal of Electroanalytical Chemistry*, 2022, **922**, 116720.
272. R. Li, X. Chen, H. Zhang, Y. Wang, Y. Lv, H. Jiang, B. Guo and X. Feng, *Inorganic Chemistry*, 2024, **63**, 2282–2288.
273. Y. Gong, L. Sun, J. Hu, F. Xie, H. Tan, Y. Qu, K. Wang and Y. Zhang, *Materials Today Energy*, 2021, **21**, 100825.
274. W. Wu, X. Wang, Y. Yan and X. Li, *Materials Letters*, 2023, **334**, 133722.

- Open Access Article. Published on 12 Februar 2026. Downloaded on 16.02.26 09:35:19.
This article is licensed under a Creative Commons Attribution-NonCommercial 3.0 Unported Licence.
275. X. Zhao, Q. Bi, C. Yang, K. Tao and L. Han, *Dalton Transactions*, 2021, **50**, 15260–15266.
276. D. K. Yadav, J. Muhammed and S. Deka, *ACS Applied Nano Materials*, 2023, **6**, 13513–13523.
277. W. Zhao, G. Yan, Y. Zheng, B. Liu, D. Jia, T. Liu, L. Cui, R. Zheng, D. Wei and J. Liu, *Journal of Colloid and Interface Science*, 2020, **565**, 295–304.
278. S. Li, T. Yu, F. Li, T. Chen, L. Zhang, G. Wang, J. Xin and D. Zhang, *Energy & Fuels*, 2022, **36**, 5492–5501.
279. Z. Andikaey, A. A. Ensafi, B. Rezaei and J.-S. Hu, *Electrochimica Acta*, 2022, **417**, 140338.
280. P. Panda, S. Roy, R. Samanta and S. Barman, *ACS Applied Nano Materials*, 2023, **6**, 15916–15924.
281. S. Y. Lee, H. J. An, J. Moon, D. H. Kim, K. W. Park and J. T. Park, *Electrochimica Acta*, 2023, **451**, 142291.
282. H. Zhang, X. Lu, L. Yang, Y. Hu, M. Yuan, C. Wang, Q. Liu, F. Yue, D. Zhou and Q. Xia, *Molecular Catalysis*, 2021, **499**, 111300.
283. Q. Mo, H. Zheng and G. Sheng, *Molecular Catalysis*, 2024, **553**, 113817.
284. A. Ibrahim, X. Liu, C. N. Uguna and C. Sun, *Materials Today Sustainability*, 2023, **23**, 100424.
285. H. Zhang, F. Sun, X. Lu, H. Guo, Y. Dong, Q. Zhang, J. Chen, D. Zhou and Q. Xia, *Molecular Catalysis*, 2023, **535**, 112903.
286. K.-R. Oh, H. Lee, H.-W. Jeong, G.-N. Yun, A. Awad, A. Nimbalkar, M. Lee and Y. K. Hwang, *Journal of CO₂ Utilization*, 2023, **78**, 102633.
287. Y. Li and S. Li, *International Journal of Hydrogen Energy*, 2020, **45**, 10433–10441.
288. Y. Song, M. Xu, Z. Li, L. He, M. Hu, L. He, Z. Zhang and M. Du, *Sensors and Actuators B: Chemical*, 2020, **311**, 127927.
289. C. Chen, Y. Zhong, S. Cheng, Y. Huang, T. Li, T. Shi, G. Liao and Z. Tang, *Journal of The Electrochemical Society*, 2020, **167**, 027531.
290. X. Zhang, D. Li, Y. Sun, C. Dong, H. Zhu, X. Li, Q. Cao, J. Shen, F. Yan and Y. Wei, *Materials Letters*, 2021, **293**, 129739.
291. Y. Zhang, Y. Huang, P. Gao, W. Yin, M. Yin, H. Pu, Q. Sun, X. Liang and H.-b. Fa, *Microchemical Journal*, 2022, **175**, 107097.
292. S. Binyamin, R. Shiloni, I. Liberman, R. Ifraimov, A. Tashakory and I. Hod, *ACS Applied Materials & Interfaces*, 2024, **16**, 13849–13857.
293. L. Jin, H. Liu, A. Xu, Y. Wu, J. Lu, J. Liu, S. Xie, Y. Yao, L. Dong, M. Zhang, S. Kai and M. Fan, *Microporous and Mesoporous Materials*, 2021, **317**, 110997.
294. K. Tong, G. Lu, F. Kong, Z. Wei, Z. Zhan and X. Wang, *ACS Applied Nano Materials*, 2025, **8**, 17440–17450.
295. H. Zhang, S. Zhang, Y. Zhang, X. Chen, H. Zhan and D. Cai, *Catalysis Letters*, 2025, **155**, 1–13.
296. M. Ma, E. Chen, H. Yue, G. Tian and S. Feng, *Nature Communications*, 2025, **16**, 367.
297. A. Dhakshinamoorthy, S. Navalón, A. Primo and H. García, *Angewandte Chemie*, 2024, **136**, e202311241.
298. J. Zhang, B. An, Z. Li, Y. Cao, Y. Dai, W. Wang, L. Zeng, W. Lin and C. Wang, *Journal of the American Chemical Society*, 2021, **143**, 8829–8837.
299. B. Gikonyo, E. Montero-Lanzuela, H. G. Baldovi, S. De, C. Journet, T. Devic, N. Guillou, D. Tiana, S. Navalón and A. Fateeva, *Journal of Materials Chemistry A*, 2022, **10**, 24938–24950.
300. Z. Yongjia, M. A. Islam and B. B. Saha, *Colloids and Surfaces A: Physicochemical and Engineering Aspects*, 2025, **713**, 136524.
301. K. Lin, J. Qin, Z. Liu, W. Xu, M. Li, Y. Zheng, W. Han, G. Zhou, J. Fang, Z. Fang, F. Peng and K. L. Yeung, *Environmental Research*, 2025, **279**, 121789.
302. C. Shi, N. Tang, S. Pu, H. Xin, L. Wu and X. Hou, *Chemical Engineering Journal*, 2025, **503**, 158621.
303. A. Santiago Portillo, H. G. Baldoví, M. T. García Fernandez, S. Navalón, P. Atienzar, B. Ferrer, M. Alvaro, H. Garcia and Z. Li, *The Journal of Physical Chemistry C*, 2017, **121**, 7015–7024.

304. A. Bhattacharyya, M. Gutiérrez, B. Cohen, A. Valverde-González, M. Iglesias and A. Douhal, *Materials Today Energy*, 2022, **29**, 101125.
305. Y. B. N. Tran, P. T. K. Nguyen, V.-A. Dao and V.-D. Le, *New Journal of Chemistry*, 2024, **48**, 5300–5310.
306. A. A. Meshram and S. M. Sontakke, *Materials Today: Proceedings*, 2023, **72**, 47–54.
307. S. Bahrani, S. A. Hashemi, S. M. Mousavi and R. Azhdari, *Drug metabolism reviews*, 2019, **51**, 356–377.
308. A. G. Eldin, E. H. Mohamed, S. M. El-Sheikh, S. M. Sheta, A. O. Youssef, E. Elshahat, M. S. Attia and M. N. Abou-Omar, *RSC Advances*, 2025, **15**, 34149–34159.
309. M. Nakhaei, K. Akhbari, M. Kalati and A. Phuruangrat, *Inorganica Chimica Acta*, 2021, **522**, 120353.
310. R. Safdar Ali, H. Meng and Z. Li, *Molecules*, 2021, **27**, 100.
311. W. Li, D. Li, Y. Yang, S. Su, S. Qie, Y. Jia and M. Hu, *Journal of Molecular Structure*, 2025, **1321**, 139974.
312. W. Wei, H. Wang, P. Su, J. Song and Y. Yang, *Talanta*, 2025, **291**, 127862.
313. Y. Wan, J. Fang, Y. Wang, J. Sun, Y. Sun, X. Sun, M. Qi, W. Li, C. Li and Y. Zhou, *Advanced healthcare materials*, 2021, **10**, 2101515.
314. A. Radwan, A. A. A. Aziz, A. M. Abdel-Aziz, M. E. Sidqi and M. A. Sayed, *Inorganic Chemistry Communications*, 2025, **179**, 114870.
315. J. Komara, J. P. Karumuri and M. Gudivada, *Research on Chemical Intermediates*, 2025, 1–19.
316. R. Abazari, A. R. Amani-Ghadim, A. M. Z. Slawin, C. L. Carpenter-Warren and A. M. Kirillov, *Inorganic Chemistry*, 2022, **61**, 9514–9522.
317. R. Bhosale, S. Bhosale, D. Narale, C. Jambhale and S. Kolekar, *Langmuir*, 2023, **39**, 12075–12089.
318. U. A. Kolachi, N. H. Solangi, Y. Sun, R. Andavar, I. Shahid, J. Zhao and J. Pan, *Journal of Materials Chemistry A*, 2025, **13**, 22142–22154.
319. T. Stolar, A. Prašnikar, V. Martinez, B. Karadeniz, A. Bjelić, G. Mali, T. Friščić, B. Likozar and K. Užarević, *ACS Applied Materials & Interfaces*, 2021, **13**, 3070–3077.
320. A. Karbalaei Hosseini, F. Moghadaskhou, A. Tadjarodi and B. Safarkoopayeh, *Inorganic Chemistry*, 2023, **62**, 21156–21163.
321. J. Liu, Y. Zhao, L.-L. Dang, G. Yang, L.-F. Ma, D.-S. Li and Y. Wang, *Chemical Communications*, 2020, **56**, 8758–8761.
322. S. Varangane, C. S. Vennapoosa, A. Tiwari, S. K. Nataraj, T. P. Yendrapati and U. Pal, *Applied Organometallic Chemistry*, 2022, **36**, e6815.
323. N. Nagarjun and A. Dhakshinamoorthy, *New Journal of Chemistry*, 2019, **43**, 18702–18712.
324. N. Nagarjun, K. Arthy and A. Dhakshinamoorthy, *European Journal of Inorganic Chemistry*, 2021, **2021**, 2108–2119.
325. H. Lv, L. Fan, H. Chen, X. Zhang and Y. Gao, *Dalton Transactions*, 2022, **51**, 3546–3556.
326. B. Yi, H. Zhao, L. Cao, X. Si, Y. Jiang, P. Cheng, Y. Zuo, Y. Zhang, L. Su, Y. Wang, C. K. Tsung, L. Y. Chou and J. Xie, *Materials Today Nano*, 2022, **17**, 100158.
327. W.-J. Ji, G.-F. Liu, B.-Q. Wang, W.-B. Lu and Q.-G. Zhai, *CrystEngComm*, 2020, **22**, 4710–4715.
328. Y. Li, F. Wang, M. Liang, M. Sun, L. Xia and F. Qu, *Talanta*, 2024, **278**, 126456.
329. Z. Zhang, L. Liu, T. Zhang and H. Tang, *ACS Applied Materials & Interfaces*, 2023, **15**, 18982–18991.
330. S. Li, R. Wang, M. Xie, Y. Xu, J. Chen and Y. Jiao, *Journal of Colloid and Interface Science*, 2022, **622**, 378–389.
331. X. Zhao, Y. Wang, Z. Zhai, C. Zhuang, D. Tian, H. Guo, X. Zou and T. X. Liu, *ACS Applied Nano Materials*, 2023, **6**, 8315–8324.
332. S.-N. Zhao, G. Wang, D. Poelman and P. V. D. Voort, *Materials*, 2018, **11**, 572.



- Open Access Article. Published on 12 Februar 2026. Downloaded on 16.02.26 09:35:19.
This article is licensed under a Creative Commons Attribution-NonCommercial 3.0 Unported Licence.
- (cc) BY-NC
- 333. L.-L. Ma, G.-P. Yang, G.-P. Li, P.-F. Zhang, J. Jin, Y. Wang, J.-M. Wang and Y.-Y. Wang, *Inorganic Chemistry Frontiers*, 2021, **8**, 329–338.
 - 334. Y. Liu, X. Zhou, W. Zhu, C. Chen, C. Fan, L. Ding and K. Wang, *Inorganic Chemistry*, 2023, **62**, 15022–15030.
 - 335. C. Simms, A. Mullaliu, F. de de Azambuja, G. Aquilanti and T. N. Parac-Vogt, *Small*, 2024, **20**, 2307236.
 - 336. Q. Zhang, Z. Sang, Q. Li, J. Gong, X. Peng, L. Li, Z. Zhang, B. Zhang, S. Li and X. Yang, *Journal of Molecular Liquids*, 2022, **356**, 119024.
 - 337. L. Zhao, K. Sun, N. Youliwasi, H. Guo, G. Yang, F. Jiao, B. Dong, Y. Chai, S. Mintova and C. Liu, *Applied Surface Science*, 2019, **470**, 91–98.
 - 338. R. Zhao, Z. Wang, W. Li, Z. Zhang, H. Xu and H. Zhao, *Journal of Materials Science*, 2025, **60**, 861–880.
 - 339. Y. Lu, Z. Bai, Z. Sun, F. Wang, S. Pei, S. Wang, C. Wang, X. Li and B. Wang, *Chemical Engineering Journal*, 2025, **520**, 166079.
 - 340. H. Lv, H. Chen, T. Hu and X. Zhang, *Inorganic Chemistry Frontiers*, 2022, **9**, 5788–5798.
 - 341. Z. Li, G. Liu, C. Fan and S. Pu, *Analytical and Bioanalytical Chemistry*, 2021, **413**, 3281–3290.
 - 342. Z. Zhao, S. Yang, M. Zhu, Y. Zhang, Y. Sun and S. Wu, *Sensors and Actuators B: Chemical*, 2023, **383**, 133593.
 - 343. M. Wu, Z. W. Jiang, P. Zhang, X. Gong and Y. Wang, *Sensors and Actuators B: Chemical*, 2023, **383**, 133596.
 - 344. Z. Lu, Y. Jiang, P. Wang, W. Xiong, B. Qi, Y. Zhang, D. Xiang and K. Zhai, *Analytical and Bioanalytical Chemistry*, 2020, **412**, 5273–5281.
 - 345. X. Yue, L. Fu, Y. Li, S. Xu, X. Lin and Y. Bai, *Food Chemistry*, 2023, **410**, 135390.
 - 346. C. Zhang, Y. Wu, X. Hong, W. Lei, M. Xia and F. Wang, *Spectrochimica Acta Part A: Molecular and Biomolecular Spectroscopy*, 2024, **304**, 123326.
 - 347. J. Yao, M. Xie and Y. Li, *Microporous and Mesoporous Materials*, 2021, **317**, 110831.
 - 348. H. Yu, Q. Liu, J. Li, Z.-M. Su, X. Li, X. Wang, J. Sun, C. Zhou and X. Hu, *Journal of Materials Chemistry C*, 2021, **9**, 562–568.
 - 349. J. Yin, H. Chu, S. Qin, H. Qi and M. Hu, *Sensors*, 2021, **21**, 7355.
 - 350. J.-L. Li, Y. Xiao, L.-Y. Wang, Y.-H. Xing, F.-Y. Bai and Z. Shi, *Polyhedron*, 2022, **214**, 115648.
 - 351. Y. Wu, Y. Zhou, H. Long, X. Chen, Y. Jiang, L. Zhang and T. Le, *Food Chemistry*, 2023, **422**, 136250.
 - 352. X. Zeng, J. Hu, M. Zhang, F. Wang, L. Wu and X. Hou, *Analytical Chemistry*, 2020, **92**, 2097–2102.
 - 353. M. Wu, Y. Zhuang, J. Liu, W. Chen, X. Li and R.-J. Xie, *Optical Materials*, 2020, **106**, 110006.
 - 354. Y. Songlin, S. Dongxue, L. Kaisu, W. Lei, Z. Ying, S. Yaguang, Z. Mingchang and W. Shuangyan, *Dyes and Pigments*, 2023, **220**, 111673.
 - 355. X. Zhai, P. Feng, N. Song, G. Zhao, Q. Liu, L. Liu, M. Tang and Y. Tang, *Inorganic Chemistry Frontiers*, 2022, **9**, 1406–1415.
 - 356. F. Zhang, Z. Zhao, F. Wang, Y. Pu and H. Cheng, *Journal of Solid State Chemistry*, 2019, **280**, 120972.
 - 357. W. Shi, T. Li, N. Chu, X. Liu, M. He, B. Bui, M. Chen and W. Chen, *Materials Science and Engineering: C*, 2021, **129**, 112404.
 - 358. Y. Gao, Y. Zhu, Y. Wang and J. Bi, *Spectrochimica Acta Part A: Molecular and Biomolecular Spectroscopy*, 2024, **323**, 124915.
 - 359. X. Jiang, J. Hu, Y. Zhang, X. Zeng and Z. Long, *Microchemical Journal*, 2020, **159**, 105417.

DATA AVAILABILITY STATEMENT

[View Article Online](#)
DOI: 10.1039/D5TA06669G

Data is available upon request to the corresponding authors.

